A Study of Equilibrium and Non-Equilibrium Phase Transition In Two Dimensional Colloidal Suspension

SHUBHENDU SHEKHAR KHALI

A thesis submitted for the partial fulfillment of
the degree of Doctor of Philosophy

Department of Physical Sciences

Indian Institute of Science Education and Research Mohali
Knowledge city, Sector 81, SAS Nagar, Manauli PO, Mohali 140306, Punjab, India.

July 2020

Certificate of Examination

This is to certify that the dissertation titled *’A Study of Equilibrium and Non-Equilibrium Phase Transition In Two Dimensional Colloidal Suspension’* submitted by Mr. Shubhendu Shekhar Khali (Reg. No. PH13018) for the partial fulfillment of Doctor of Philosophy programme of the Institute, has been examined by the thesis committee duly appointed by the Institute. The committee finds the work done by the candidate satisfactory and recommends that the report be accepted.

Dr. Abhishek Chaudhuri Dr. Rajeev Kapri Dr. Dipanjan Chakraborty

(Supervisor)

Declaration

The work presented in this thesis has been carried out by me under the guidance of Dr. Dipanjan Chakraborty at the Indian Institute of Science Education and Research Mohali. This work has not been submitted in part or in full for a degree, a diploma, or a fellowship to any other university or institute. Whenever contributions of others are involved, every effort is made to indicate this clearly, with due acknowledgement of collaborative research and discussions. This thesis is a bona fide record of original work done by me and all sources listed within have been detailed in the bibliography.

Shubhendu Shekhar Khali

(PH13018)

In my capacity as the supervisor of the candidate's thesis work, I certify that the above statements by the candidate are true to the best of my knowledge.

Dr. Dipanjan Chakraborty

(Supervisor)

Acknowledgements

First of all, I wish to show my deepest gratitude to my thesis supervisor Dr Dipanjan Chakraborty, whose friendly behaviour always makes the learning process full of joy. Despite knowing the fact that I need to build my understanding of programming from scratch, he provided me with an opportunity to pursue my PhD in his group and patiently trained me in developing the required skills. His steadfast encouragement, especially the way he pulled me out through tough times is inexpressible. The work ethic I learned from him will remain to be the most valuable lesson throughout my life.

I specially thank Dr Debasish Chaudhuri from IOP (Bhubaneswar, India) who collaboratively supported us all the way through in completing the thesis work.

I am also thankful to my doctoral committee members Dr Abhishek Chaudhuri and Dr Rajeev Kapri, for providing their time for the valuable discussions. I thank all the other faculty members, computing staff members especially Garima ma'am, Sunny, Ramesh sir, administrative staff members and rest of the IISER Mohali community for providing helping hands in the direct or indirect way during the period of my PhD.

I feel privileged to be part of a very supportive research group which includes: Mayank Srivastava (from whom one can learn to live day to day life in an utmost balanced manner), Anirban Ghosh (well versed on current-affairs), Sudipto Mandal (with a very joyful nature), Yogyata Pathania ma'am (post-doc fellow, a very calm person), Moutushi di (post-doc fellow, full of liveliness) and two junior fellows Nitish Chetri and Dimpi (both of them have superb hands in sketching). Though most of us avoid expressing our emotions, deep inside, we share a strong bonding.

I like to mention some names from which I got precious assistance: Gopal verma, Satyam Srivastava, Sushanshu Shekhar Chaurasia, Ankit Singh, Avinash, Ashiwani Balodhi, Rakesh Sharma, Jaskaran Singh, Ramu Kumar Yadav, Aashish, Gokul, Aman, Ranbir, Ritesh, Anzar, Amit, Shailendra and Shyam. A special thanks goes to Rajneesh Perhate (for helping in my early days), Deepak Singh Kathayat(painter, poet, mythologist and our chess-guru), Arnob Mukharji (with a very caring nature, and a badminton champ), Swagatam Nayak (the style guru) and Sandeep Rana(conversation with whom motivated me during low times) for their company.

"Some people deserve more than just a Thank you". This sentence seems to be true when it comes to writing a 'Thank you note' in favour of the family members. Still, I thank my parents and 'Richa di' for everything.

Shubhendu Shekhar Khali
Mohali, July 30, 2020.

विद्यां चाविद्यां च यस्तद्वेदोभ्य सह ।
अविद्यया मृत्युं तीर्त्वाऽमृतमश्नुते ॥
(ईशा उपनिषद)

vidyāṃ cāvidyāṃ ca yastadvedobhya saha ।
avidyayā mṛtyuṃ tīrtvā’mṛtamaśnute ॥
(Isha upnishad)

One who knows both, the material as well as spritual, transgresses fear of death by the former (by proper bodilly and mental effort), and attains salvation by the latter (by the purity of mind and soul).

Contents

Abstract **3**

1 Introduction **5**

1.1 Role of dimension in melting-freezing transition 9
  1.1.1 One dimensional linear chain of magnetic moments 10
  1.1.2 XY model and Mermin-Wagner Theorem 11
1.2 Berezinskii-Kosterliz-Thouless-Halperin-Nelson-Young theory 14
1.3 System under constant confinement 21
1.4 Brownian Ratchets 24
  1.4.1 Feynman Ratchet: A mechanical rectifier 24
  1.4.2 Mathematical Model for the generation of directed motion 26
Bibliography 31

2 Phase transition in a system of two-dimensional colloids interacting via inverse twelfth power potential. **37**

2.1 Introduction 38
2.2 Model and Simulation Details 39
2.3 Solid and hexatic melting 40
  2.3.1 Thermodynamic Pressure 41
  2.3.2 Static Structure Function and Solid Order Parameter 41
  2.3.3 Pair-correlation Function and Identification of Solid-Melting Point 44
  2.3.4 Orientational Order and Hexatic Melting 48
2.4 Order of the transition 52
2.5 Conclusion 55
Bibliography 59

3 Phase transition in a system of two dimensional colloids interacting via Week-Chandler-Anderson potential **61**

3.1 Introduction 62
3.2 Model and Simulation Details 62
3.3 Melting point of solid and the hexatic phase 64
  3.3.1 Thermodynamic Pressure 64
  3.3.2 Melting of the solid: Solid order parameter 64
  3.3.3 Melting of the solid:Correlation function 68
  3.3.4 Melting of solid:Finite size scaling 70

3.3.5 Hexatic melting: Order parameter 71
3.3.6 Hexatic melting: Order parameter correlation 72
3.3.7 Hexatic melting: Finite size scaling 73
3.4 Defect formation in the system 73
3.5 Order of the transitions 79
3.6 Conclusion 82
Bibliography 85

4 Phase transition in a driven system 87
4.1 Introduction 88
4.2 Model and Simulation Details 89
4.3 Results and Discussion 91
4.3.1 Phase diagram 91
4.3.2 Directed particle current and order 93
4.3.3 Non-equilibrium melting 98
4.3.4 Continuous transition: Distribution of order parameters 102
4.3.5 Pair correlation: quasi- long ranged order to disorder 104
4.3.6 Defect formation 109
4.4 Discussion 111
Bibliography 113

5 Summary and Outlook 117

List of Figures 123

Abstract

A flashing ratchet refers to an overall directed motion of particles in a thermal environment under the influence of an asymmetric potential, switching on and off stochastically. This model has been studied in the context of active dynamics of molecular motors, as a mechanism of particle segregation, transport of cold atoms in optical lattice, in motion of flux quanta and in describing the collective dynamics of elastically coupled motor proteins. While a large body of work has been concentrated on the ratcheting effect of non-interacting systems in one spatial dimension, there has been fewer studies that focuses on the effects of interaction in one or higher dimensions. Despite moderate efforts, the collective dynamics of interacting system of particles under ratcheting drives remains largely unexplored. It is also worth noting that in most of such studies the focus had been on the transport properties of the system and its dependence on the external control parameter.

In the first part of the thesis, we present our results on the study of equilibrium phase transition in a two dimensional system of interacting colloidal suspension and compare it with that of the predictions from KTHNY theory and grain boundary melting. The melting transition is identified from the translational and the orientational order parameter and their correlation functions. The nature of the phase transition is determined from the distribution of the order parameters and the local density fluctuations.

In the second part of the thesis, we look at such a two dimensional colloidal dispersion of soft-core particles driven by a one dimensional stochastic flashing ratchet that induces a time averaged directed particle current through the system. It undergoes a non-equilibrium melting transition as the directed current approaches a maximum associated with a resonance of the ratcheting frequency with the relaxation frequency of the system. We use extensive molecular dynamics simulations to present a detailed phase dia- gram in the ratcheting rate- mean density plane. With the help of numerically calculated structure factor, solid and hexatic order parameters, and pair correlation functions, we show that the non- equilibrium melting is a continuous transition from a quasi-long ranged ordered solid to a hexatic phase. The transition is mediated by the unbinding of dislocations, and formation of compact and string-like defect clusters.

1

Introduction

A brief introduction to equilibrium melting in two dimensions is presented in this chapter. The discussion centers on the development of the Berezinskii-Kosterlitz-Thouless-Halperin-Nelson-Young (BKTHNY) theory of melting in two dimensional systems and a brief review of experimental and computational studies on melting in two-dimensional colloidal dispersions. Role of dimension in phase transition and the BKTHNY theroy is reviewed briefly. Freezing in two-dimensions in presence of external applied field and the concept of rectification of Brownian forces using flashing ratchets in also presented to connect our work on melting under non-equilibrium conditions.

Phase transitions are ubiquitous in nature and encountered quite frequently in our every-day life. As a consequence, it is perhaps the single most topic in condensed matter that has garnered unparalleled attention from the scientific community. The first phenomenological explanation that explained the physics of phase transitions was put forward by Landau in 1937.[1,2] The most significant aspect of the theory was the notion of an order parameter that remains zero above the transition temperature and is finite below it. This very simplistic approach has a rather deeper physical insight. Every phase of matter is characterized by different symmetries and the change in the value of the order parameter from zero to a non-zero value signifies the breaking of these symmetries. The most celebrated example is that of a paramagnetic to a ferro-magnetic transition, where the underlying up-down symmetry is broken in going from a paramagnetic to a ferromagnetic phase. The magnetization serves as the order parameter of the transition that remains zero in the paramagnetic phase and has a non-zero value in the ferromagnetic phase. The standard classification of a phase transition is dictated by the behavior of the order parameter near the transition point. If the order-parameter is discontinuous across the transition point, the phase-transition is first order, and if it is continuous, the transition is second-order or a continuous transition. In the earlier example of para to ferro-magnetic phase, the transition is continuous when the transition happens in the absence of an external magnetic field. When an external field is applied, the spins align in the direction of the field, and a finite magnetization appears. This is a first-order transition. Yet another example is that of transition between the three states of matter: solid-liquid and liquid-gas transition.

In Fig. 1.1, a typical phase diagram of such a transition has been shown in the pressure (P) - temperature (T) plane, along with that of water. Three different phases of the matter, i.e. solid, liquid and gas can be separated with the corresponding phase boundaries. These boundaries represent the regions of coexistence of two different phases. At the triple point (P_t, T_t), where the three curves meet, all three phases exist together. Any transition from one phase to other that happens via crossing the phase boundary is known to be discontinuous. As free energy associated with the system becomes non-analytic function and its first derivative with respect to temperature and pressure shows a finite discontinuity at the phase boundaries.

The transition between gas and liquid can also happen via following a path around the critical point. It is the point where the liquid-gas phase boundary terminates. The transition is continuous and is characterized by universal behavior among the systems in terms of some defined critical exponents. These critical exponents possess identical values irrespective of the microscopic interaction in the systems and depend only on dimensionality and symmetry of the order parameters. This equivalence across different

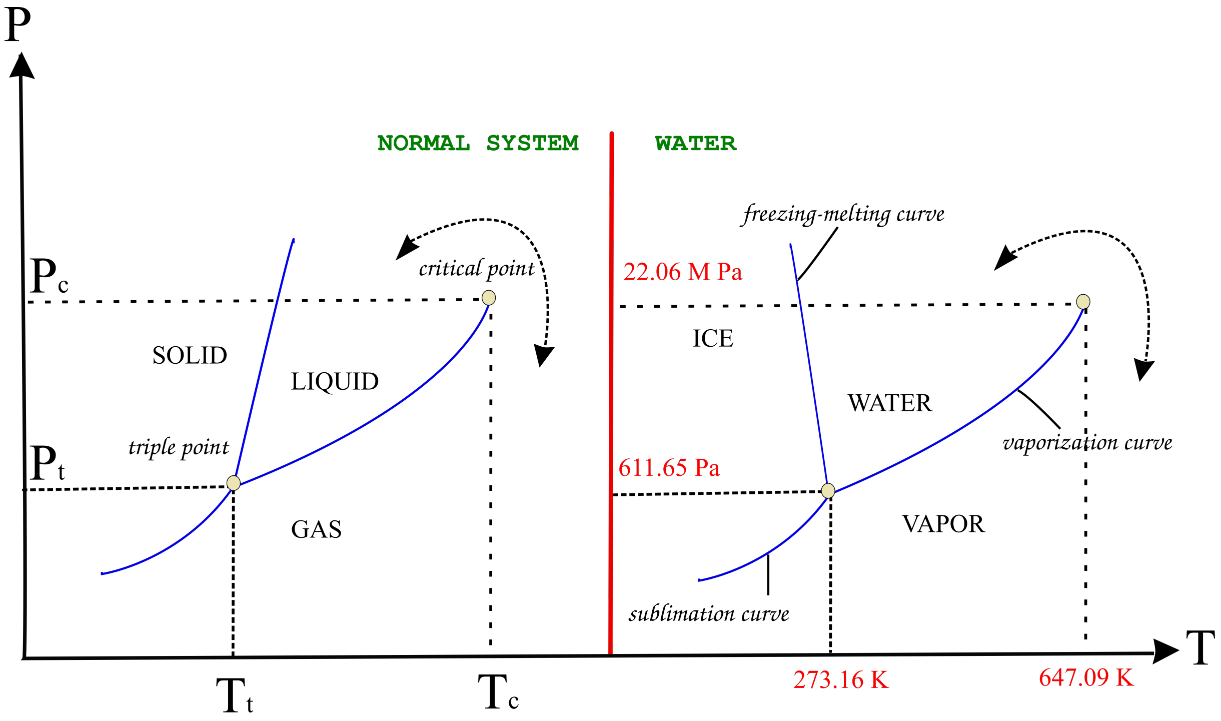
P
NORMAL SYSTEM
WATER
P_c
critical point
freezing-melting curve
22.06 M Pa
SOLID
LIQUID
ICE
WATER
triple point
P_t
vaporization curve
611.65 Pa
GAS
VAPOR
sublimation curve
T
T_t
T_c
273.16 K
647.09 K

Figure 1.1 Pressure-temperature plane in three dimensional space

systems is a direct consequence of the diverging length and time scales in a continuous transition.

The existence of a system in different phases is determined by the free energy of the system $F = U - TS$, where U is the internal energy system, T is the temperature, and S is the entropy of the system. A stable thermodynamic equilibrium requires the minimization of this free-energy, leading to a competition between the internal energy and the entropy. At the high temperatures where the number of available microstates is large, entropy being proportional to this number dominates over internal energy and the system appears in a disordered phase. On the other hand, at low temperatures, internal energy plays the dominant role and pushes the system to be in the ordered phase. A disordered phase, therefore, implies to highly symmetric phase. Transition to an ordered state happens via breaking of all or some of these symmetries. This spontaneous symmetry breaking is precisely the conceptual idea behind the Landau–Ginzburg theory of phase-transition. The phenomenological description expresses the free energy in terms of a polynomial function of the order parameter. The terms in the expression of F is governed by the underlying symmetries of the system. The theory, however, neglects thermal fluctuations in the system that becomes extremely important in the vicinity of a second-order transition. Later, more comprehensive theories of phase-transition that incorporate thermal fluctuations have been developed.

The spontaneous symmetry breaking leading to a more ordered state works quite well in three dimensions. The physics of phase-transition changes as the dimensionality of the system is altered.As we pass from three to two-dimensional systems, thermal fluctuations destroy long-range ordering in the system leading to a non-zero value of the order parameter. Hence, phase-transition in such systems can happen only at a zero temperature. Yet, there were abundant examples that contradict this simple argument.[3–19] Perhaps, the earliest example of an ordered state in two-dimension was the formation and melting of a Wigner crystal in a system of two-dimensional electrons on the surface of liquid Helium.[20–23] The explanation of this contradiction came from Berezinskii, Kosterlitz and Thouless (BKT).[17,19,24–26] In fact, the work by Berezinskii remains a seminal work on phase-transitions in two-dimensional systems. The BKT theory clearly showed that the order parameter correlation exhibits an algebraic decay in an ordered phase and faster exponential decay in the disordered phase. Since the decays do not match smoothly, the transition between these two phases was a phase transition. Unlike the spontaneous symmetry breaking in three dimensional systems, the phase-transition in two-dimensions is induced by the dissociation of topological defects. In two-dimensional solids, the majority of defects are quartets – pairs of dislocations. The unbinding of these quartets into dislocations which are pairs of five and seven fold topological defects induces the melting of the solid. A quasi long range translational order exists in the solid phase that transforms into a short-range order upon the melting of the solid. The solid phase is also characterized by a true long-range orientational order. Later works by Halperin and Nelson showed that with the melting of the solid, the system still remains anisotropic.[27,28] The dissociation of the dislocation pairs changes the long-range orientational order into a slowly algebraic decay. This is the hexatic phase. It retains some element of ordering even though the shear modulus vanishes. The unbinding of the dislocation into free disclinations – defects with five and seven fold degeneracy induces the transition to an isotropic liquid. In sharp contrast to a three dimensional system, two-dimensional melting is a two-step process and within the framework of Berezinskii-Kosterliz-Thouless-Halperin-Nelson-Young (BKTHNY) theory both the transitions are continuous.[24,26–29]

While the BKTHNY theory is very appealing, the proposed melting scenario in the theory is not universal and depends on the microscopic interactions of the system. Even with almost a 4-decade long history,[30–34] the problem of melting in two-dimensions is not completely understood. Perhaps the most suited model systems to study two dimensional melting are that of colloidal suspensions, specifically due to their size, which makes them amenable to experimental observations. The additional advantage of using a colloidal suspension is that the inter-particle interaction can be precisely tuned leading to different equilibrium phase diagrams. Indeed, an enormous amount of effort was put in to investigate two dimensional melting in colloidal dispersions using experiment[31,35–50] and computer simulations.[51–64,64–72] All of these indicate that the melting scenarios are dependent on pair-interaction,[51,61,68,69] particle shape,[70] pinning of particle or vacancies[66,71] and even out of plane fluctuations.[67] The current understanding is that BKTHNY theory is applicable to systems with long-range interaction. For short-ranged Lennard–Jones interactions, the BKTHNY scenario applies well in the high-temperature regime whereas for repulsive interactions $\sim r^{-n}$ the BKTHNY theory holds for $n < 12$ and for values $12 \leq n \leq 64$, the solid-hexatic melting is consistent with BKTHNY but the hexatic-liquid transition is first order.[51,61,69] In fact, it is worth noting that alternative theories of melting via grain-boundaries has also been proposed.[73–75] Finally, we invite the readers to look at the recent review by Ryzhov *et. al.*[34] and the references therein for a more comprehensive review of two-dimensional melting.

The central theme of this thesis is to study equilibrium and non-equilibrium phase-transition of a two-dimensional colloidal suspension. In the equilibrium scenario, we study the phase diagram of a mono-dispersed colloidal suspension interacting with a repulsive potential, the details of which are presented in Chapter 2. We also study the equilibrium melting scenario of a similar system but interacting with Weeks-Chandler-Anderson potential (see Chapter 3). In the non-equilibrium scenario presented in Chapter 4, we consider a two dimensional colloidal dispersion of soft-core particles driven by a one dimensional stochastic flashing ratchet that induces a time averaged directed particle current through the system. The system undergoes a non-equilibrium melting transition as the directed current approaches a maximum associated with a resonance of the ratcheting frequency with the relaxation frequency of the system.

The rest of this chapter is organized in the following way. In context of the equilibrium two-dimensional melting, we present very brief discussions on fluctuations in one and two dimensional systems in Section 1.1 and present the BKTHNY theory in Section 1.2. In the non-equilibrium scenario, since the common practice to drive a colloidal suspension out of equilibrium is to apply an external field - either a static field or a time dependent field we have presented a brief discussion on the phenomena of laser-induced freezing in Section 1.3. Finally, as the driving of the colloidal suspension is done via flashing ratchet, a discussion on Brownian ratchets in presented in Section 1.4.

1.1 Role of dimension in melting-freezing transition

In lower dimensions $d \leq 2$, thermal fluctuations become quite prominent and make great impact on the macroscopic behavior of the system. Due to presence of long wave length (low wave vector) fluctuations, systems in one and two dimensions can not acquire long range order. It was first discussed by Rudolf Peierls[76] and Landau[1,2] in mid-1930. They studied the effect of thermal fluctuations in different dimensions and concluded that spatial fluctuation in local order term diverges linearly in one dimension, logarithmically in two dimension and remains finite in three dimension.

1.1.1 One dimensional linear chain of magnetic moments

Peierls arguments are based on harmonic approximation and can be understood by analyzing a system of size L, comprising N magnetic moments (spins) in one dimension. Each spin interacts with its neighboring spin only. If $\delta\phi_i$ is the rotation of the i^{th} spin relative to its neighbors, then for the longest wavelength mode (see Fig. 1.2)

$$\sum_{i=1}^{N} \delta\phi_i = 2\pi \tag{1.1}$$

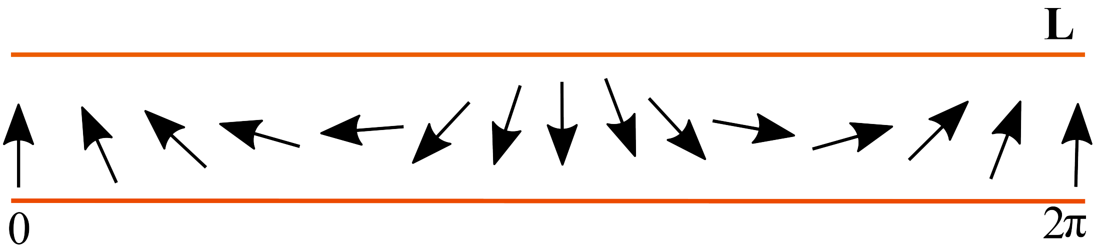

Figure 1.2 Sketch representing the longest wavelength of spins fluctuation in the system of size L in one dimensional space.

The relative rotation per unit length is $\frac{2\pi}{L}$. As the interaction is harmonic, energy density of the longest wavelength mode becomes $\propto (2\pi/L)^2$. Thus the total energy comes out to be $\propto L(2\pi/L)^2$, implying that at any finite temperature, the long wavelength fluctuations can always be excited in one dimension.

Extending this case to the higher dimensions, one can observe that the energy of the long wavelength fluctuations is $\propto L^2(2\pi/L)^2$ in two dimension and is independent of the system size and is responsible for the breaking of long range order. However in three dimension this energy depends on the system size :$\propto L^3(2\pi/L)^2$ and therefore, to excite long wave length fluctuations in a large system requires a substantial energy which can not be full filled by the thermal energy if the temperature is low.

1.1.2 XY model and Mermin-Wagner Theorem

The lack of long range order due to fluctuations, in two dimensional space, can also be realized from Mermin-Wagner theorem. According to the theorem, "In a system with short-range interactions, at any finite temperature, continuous symmetry can not be broken spontaneously in lower dimensions $d \leq 2$." The word "Spontaneously" here means examining the system in the absence of external field.

David Mermin and Herbert Wagner analyzed a system of classical spins on square lattice, knwon as XY-Model[77]. In this model, each spin can opt any orientation in the X-Y plane as a result of nearest neighbor interaction. Fig. 1.3 represents the sketch for such a case.

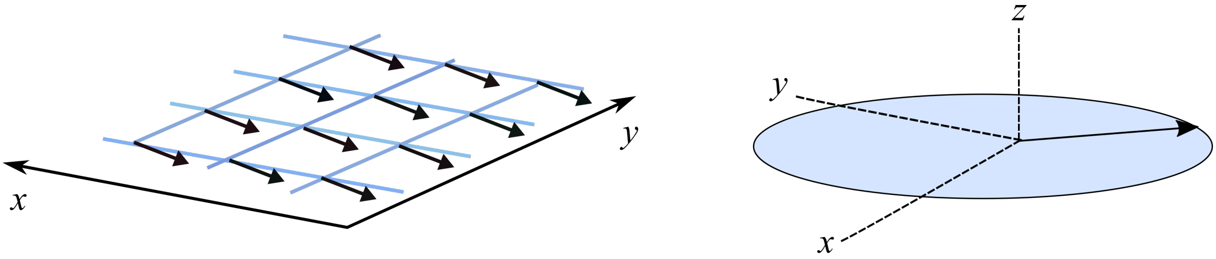

Figure 1.3 Schematic representation of XY Model. In (a) spins residing on the sites of a square lattice and (b) representing the allowed values that each spin can take.

The Hamiltonian of such a system can be represented as

$$H = -J \sum_{(i,j)} \mathbf{s}_i . \mathbf{s}_j = -J \sum_{(i,j)} cos(\phi_i - \phi_j) \tag{1.2}$$

Here, J is a constant (exchange energy) and controls the strength of the interaction and ϕ_i is the angle that the i^{th} spin makes with an arbitrary fixed axis. Clearly the Hamiltonian depends upon the relative angle of the neighboring spins. Transforming the angles through a constant value $\phi_i \rightarrow \phi_i + c$, does not affect the Hamiltonian and thus shows rotational invariance of it.

At absolute zero temperature, the ground state configuration belongs to the ordered state, all spins being aligned in the same direction. This broken symmetry phase known as ’Ferromagnetic’ is characterized by non-zero magnetization $M = (1/N)\sum_i \mathbf{s}_i$. On the other hand at high values of temperature, spins become randomly orientated and result in rotationally symmetric ’Paramagnetic’ phase with zero value of magnetization. The correlation length of spin’s orientation can be quantified by calculating the function $C(\mathbf{r}_i - \mathbf{r}_j) = \langle e^{\mathbb{i}(\phi(\mathbf{r}_i) - \phi(\mathbf{r}_j))} \rangle$. In the ’Ferromagnetic’ phase, one can expect the value of this function to be one through out the system as $\phi(\mathbf{r}_i) = \phi(\mathbf{r}_j)$ there. In the paramagnetic phase, the function $C(\mathbf{r}_i - \mathbf{r}_j)$ goes to zero beyond the correlation length.

In 2D case, if we consider an ordered state at temperature T (even slightly above the absolute zero) and evaluate $C(\mathbf{r}_i - \mathbf{r}_j)$, it shows power law decay with the separation $|\mathbf{r}_i - \mathbf{r}_j| = \delta r$.

For negligibly small fluctuations between neighboring spins, the Hamiltonian Eq. (1.2) can be approximated by

$$H \approx E_0 + \frac{J}{2} \sum_{(i,j)} (\phi_i - \phi_j)^2 \tag{1.3}$$

and in the continuum limit it becomes,

$$H \approx \frac{J}{2} \int d^2r (\nabla \phi(\mathbf{r}))^2 \tag{1.4}$$

Using the Fourier transformation: $\phi(\mathbf{r}) = \frac{1}{2\pi} \int d^2k e^{\mathbb{i}\mathbf{k}\cdot\mathbf{r}} \phi(\mathbf{k})$ and integrating over $\mathbf{r}$,

$$H = \frac{J}{2} \int d^2k \phi(\mathbf{k}) \phi(-\mathbf{k}) k^2 \tag{1.5}$$

Since $\phi(\mathbf{r})$ is real, $\phi(-\mathbf{k}) = (\phi(\mathbf{k}))^*$ and taking $\varepsilon(\mathbf{k}) = Jk^2$ we get

$$H = \frac{1}{2} \int d^2k \varepsilon(\mathbf{k}) |\phi(\mathbf{k})|^2 \tag{1.6}$$

Now, the equipartition dictates

$$\langle \phi(\mathbf{k}) \phi(\mathbf{k'}) \rangle = \delta(\mathbf{k} + \mathbf{k'}) (\beta \varepsilon(\mathbf{k}))^{-1} \tag{1.7}$$

For the Gaussian Hamiltonian, the correlation function takes the form

$$c(\mathbf{r} - \mathbf{r'}) = \langle e^{i(\phi(\mathbf{r}) - \phi(\mathbf{r'}))} \rangle = e^{-1/2 \langle (\phi(\mathbf{r}) - \phi(\mathbf{r'}))^2 \rangle} \tag{1.8}$$

Now,

$$\langle (\phi(\mathbf{r}) - \phi(\mathbf{r'}))^2 \rangle = \int \frac{d^2k' d^2k}{(2\pi)^2} (e^{i\mathbf{k}.\mathbf{r}} - e^{i\mathbf{k}.\mathbf{r'}})(e^{i\mathbf{k'}.\mathbf{r}} - e^{i\mathbf{k'}.\mathbf{r'}}) \langle \phi(\mathbf{k}) \phi(\mathbf{k'}) \tag{1.9}$$

putting the value of $\langle\phi(\mathbf{k})\phi(\mathbf{k'})\rangle$ from Eq. (1.7) we get:

$$\langle(\phi(\mathbf{r})-\phi(\mathbf{r'}))^2\rangle = \frac{1}{2\pi}\int d^2k(e^{i\mathbf{k}.\mathbf{r}}-e^{i\mathbf{k}.\mathbf{r'}})(e^{i\mathbf{k}.\mathbf{r}}-e^{i\mathbf{k}.\mathbf{r'}})\frac{1}{\beta\varepsilon(\mathbf{k})} = \frac{1}{2\beta\pi^2}\int d^2k\frac{(1-cos(\delta\mathbf{r}.\mathbf{k}))}{\varepsilon(\mathbf{k})} \tag{1.10}$$

Breaking this integral Eq. (1.10) into two parts:

$$\frac{1}{2\beta\pi^2}[\int^{1/\delta r} d^2k\frac{(1-cos(\delta\mathbf{r}.\mathbf{k}))}{\varepsilon(\mathbf{k})} + \int_{1/\delta r} d^2k\frac{(1-cos(\delta\mathbf{r}.\mathbf{k}))}{\varepsilon(\mathbf{k})}] \tag{1.11}$$

In the large δr limit,

First part gives $\int^{1/\delta r} d^2k\frac{(1-cos(\delta\mathbf{r}.\mathbf{k}))}{\varepsilon(\mathbf{k})} \to 0$

and dropping the cosine term from the second part as its oscillating '+' and '-' values will be averaged out, we left with

$$\frac{1}{\beta J\pi}\int_{1/\delta r} dk\frac{1}{k} \tag{1.12}$$

Clearly, this integral has logarithmic divergence for large k-values.

For the discrete lattice model, the lattice spacing 'a' imposes upper limit on k-values. Therefore by restricting the k-values up to 1^{st} Brilloiun zone, the function $\langle(\phi(\mathbf{r})-\phi(\mathbf{r'}))^2\rangle$ becomes $\frac{1}{\beta J\pi}log(\alpha\delta r)$. '$\alpha$', the upper limit of integral is $\propto a^{-1}$.

Finally, the correlation function $c(\mathbf{r}-\mathbf{r'})$ comes out to be

$$c(\mathbf{r}-\mathbf{r'}) \propto (\alpha\delta r)^{-\eta(T)} \tag{1.13}$$

with $\eta = \frac{T}{2\pi J}$.

This result Eq. (1.13) shows, spins at large distances are uncorrelated and hence claims that system can not appear in the 'broken symmetry phase' (Ferromagnetic) at any finite temperature.

The results obtained by Mermin and Wagner are universal in nature and are applicable to any 2d system with continuous symmetry. In the case of solids, the spin orientation vector $\mathbf{s}_i$ can be replaced by a vector $\mathbf{u}_i$ defining particles deviations from the equilibrium positions. Similar to the previous case, for small relative displacements, Hamiltonian of the system can be approximated by

$$\frac{K}{2}\sum_{i,j}(\mathbf{u}_i-\mathbf{u}_j)^2$$

The quadratic form of the Hamiltonian will again lead to the logarithmically diverging positional fluctuations at large distances according to

$$\langle(\mathbf{u}_i-\mathbf{u}_j)^2\rangle \propto \ln|\mathbf{r}_i-\mathbf{r}_j|$$

1.2 Berezinskii-Kosterliz-Thouless-Halperin-Nelson-Young theory

The fact that two dimensional systems lack true long range order does not rule out the possibility of phase transition in these systems. The positional order approaches to zero in both solid and liquid phases, but its decaying behavior in the two phases obey different laws. In solids, the logarithmic divergence in positional fluctuations $\langle|\mathbf{u}(\mathbf{r}_i)-\mathbf{u}(\mathbf{r}_j)|^2\rangle \propto \ln(|\mathbf{r}_i-\mathbf{r}_j|)$, ensures that the positional order $\rho_{\mathbf{G}}(\mathbf{r}) = e^{-\iota\mathbf{G}\cdot\mathbf{r}}$ decays very slowly following the power low behavior $\langle\rho_{\mathbf{G}}(r)\rho_{\text{-}\mathbf{G}}(0)\rangle \propto r^{-\eta_{\mathbf{G}}(T)}$. The structure factor in 2D solids, holds power law singularity $S(q) \propto |\mathbf{q}-\mathbf{G}|^{-2+\eta_{\mathbf{G}}(T)}$, as a consequence Bragg peaks in the Fourier plane appear with spread in them. On the other hand in liquid the order lasts only for few atomic distances and shows exponentially decaying behavior.

Along with quasi-long range positional order, 2D solids exhibit long range correlation in orientational order $\psi_6(\mathbf{r}) = e^{(6\iota\theta(\mathbf{r}))}$. Here θ is the angle between two neighboring particles, measured with respect to some fixed reference axis at location $\mathbf{r}$. As solid melts, system losses positional order immediately but the orientational correlation first shift to a power law decaying function $\langle\psi_6^*(\mathbf{r})\psi_6(0)\rangle \propto r^{-\eta_6(T)}$ and then obtains the exponential form. The algebraically decaying orientational order together with short range positional order, corresponds to an intermediate hexatic phase. The shear modulus in the hexatic phase comes out to be zero, which resembles with the liquid phase. The slowly decaying nature of orientational correlation however, reflects the presence of some residual anisotropy in this phase. The isotropic liquid phase is characterized by both positional and orientational correlations that decay exponentially.

The most renowned theory developed so far regarding 2D melting is "Berezinskii-

Kosterlitz-Thouless-Halperin-Nelson-Young" in short BKTHNY. It takes very microscopic details into account in explaining the melting transition. According to the theory, melting happens as a result of unbinding of topological defects. There are two classes of the defects namely ’dislocation’ and ’disclination’, the presence of which helps in restoring the lost translational and rotational symmetries of the isotropic liquid respectively. These defects are topological in the sense that any continuous transformation can not make them to disappear from the crystal structure.

In an ideal triangular lattice, each site posses six neighbors Fig. 1.4(a). Therefore in 2D solid if a particle have neighbors other than six, it can be assigned the label of ’defect’. A pair of closely held five-fold and seven-fold particles forms a dislocation. The presence of these defects is responsible for breaking the positional order of the system. A dislocation can be characterized by a ’Burger vector’. It can be calculated by drawing a closed circuit around the dislocation. In Fig. 1.4(b) a Burger circuit starting from point A is shown. It is constructed by taking three steps in one direction and four steps in the other direction. The extra lattice vector **b** which comes out after closing the loop is the Burger vector for the enclosed dislocation. It is almost in perpendicular direction of the line that joins five-fold defect with the seven-fold defect. The length of Burger vector increases with the number of dislocations and is direct multiple of them. Thus it measures the strength and orientation of displacement field **u(r)** associated with a dislocation at a position **r**. Mathematically it can be represented as

$$\oint d\mathbf{u(r)} = a_0\mathbf{b(r)} = -n(\mathbf{r})a_0\mathbf{e}_1 - m(\mathbf{r})a_0\mathbf{e}_2 \tag{1.14}$$

Here, a_0 is the lattice spacing, $\mathbf{e}_1$ and $\mathbf{e}_1$ are the basis vectors of the triangular lattice and m and n are integers.

In an otherwise perfect triangular lattice the presence of a dislocation can be imagined as a consequence of inserting two half planes as can be seen in Fig. 1.4(b). However, emergence of such a situation in a spontaneous manner is unreal. There must be a continuous process which can lead to a state that contains dislocations. This provides an insight to assume strong attractive interaction among the defects particles. In the solid, dislocations appear in a bounded pairs having Burger vectors in opposite directions. These are called ’quartets’. The presence of these defects allows the system to possess quasi-long-range positional order along with long range orientational order. The BKTHNY theory, considers an elastic Hamiltonian for the system

$$H_E = \frac{1}{2}\int d^2r(2\mu u_{ij}^2 + \lambda u_{kk}^2) \tag{1.15}$$

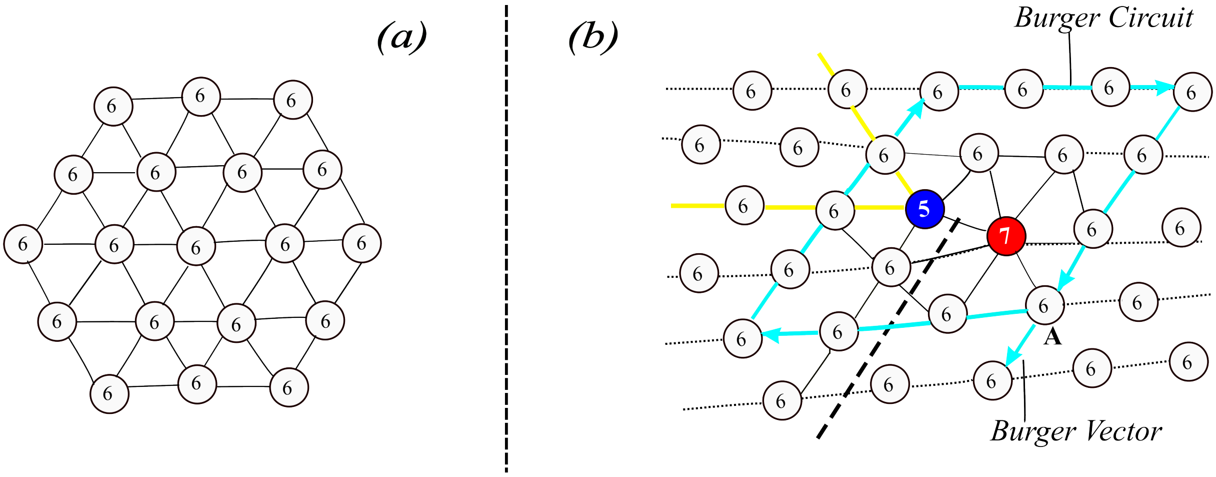

Figure 1.4 Figure (a) represents a perfect triangular lattice, in which each site is surrounded by six neighbors. Figure (b) shows generation of a dislocation in an otherwise perfect triangular lattice as a result of inserting two half planes (highlighted with yellow color) inside it. At the point where these planes terminate, a five-fold defect together with a seven-fold defect is generated. The closed Burger circuit around the dislocation is shown in blue color. The black dashed line represents the Volterra-cut. If the crystal is cut along this line up to its tip and both sides of it get shifted relative to each other by a lattice spacing a , the structure of the perfect triangular crystal gets recovered.

Here, $u_{ij} = \frac{1}{2}\left[\frac{\partial \mathbf{u}_i(\mathbf{r})}{\partial r_j} + \frac{\partial \mathbf{u}_j(\mathbf{r})}{\partial r_i}\right]$, is the strain tensor, which involves displacement field components u_i. 'λ' and 'μ' are the Lamé coefficients.

Using equations Eq. (1.14) and Eq. (1.15), leads to the Hamiltonian for a system of arbitrary distributed dislocations of the form

$$H_{dis} = -\frac{a_0^2 K}{8\pi}\sum_{i\neq j}^{M}\left[\mathbf{b}(\mathbf{r}_i)\cdot\mathbf{b}(\mathbf{r}_j)\frac{\ln(r_{ij})}{a} - \frac{(\mathbf{b}(\mathbf{r}_i)\cdot\mathbf{r}_{ij})(\mathbf{b}(\mathbf{r}_j)\cdot\mathbf{r}_{ij})}{r_{ij}^2}\right] + E_c\sum_{i=1}^{M}|\mathbf{b}(\mathbf{r}_i)|^2 \qquad (1.16)$$

Here E_c is the dislocation core energy, a is the dislocation core radius and K is the Young modulus,

$$K = \frac{4\mu(\mu+\lambda)}{2\mu+\lambda} \qquad (1.17)$$

The last term in Eq. (1.16) represents the number of dislocations in the system. Eq. (1.16) indicates that the energy of a single dislocation diverges with system size according to $E_d \propto \ln(\frac{R}{a})$. Whereas for the bounded dislocations with anti-symmetric Burger vectors such that $\mathbf{b}(\mathbf{r}_1) + (-\mathbf{b}(\mathbf{r}_2)) = 0$, the logarithmic divergence of the energy disappears,

$$E_d = \frac{a_0^2 b^2 K}{4\pi} \ln \frac{r_{12}}{a} - \frac{a_0^2 K}{4\pi} \frac{(\mathbf{b} \cdot \mathbf{r}_{12})^2}{r_{12}^2} + 2E_c \tag{1.18}$$

This non-diverging condition remains true for a number of dislocations as long as they satisfy the neutrality condition

$$\Sigma_{i=1}^{n} \mathbf{b}(\mathbf{r}_i) = 0 \tag{1.19}$$

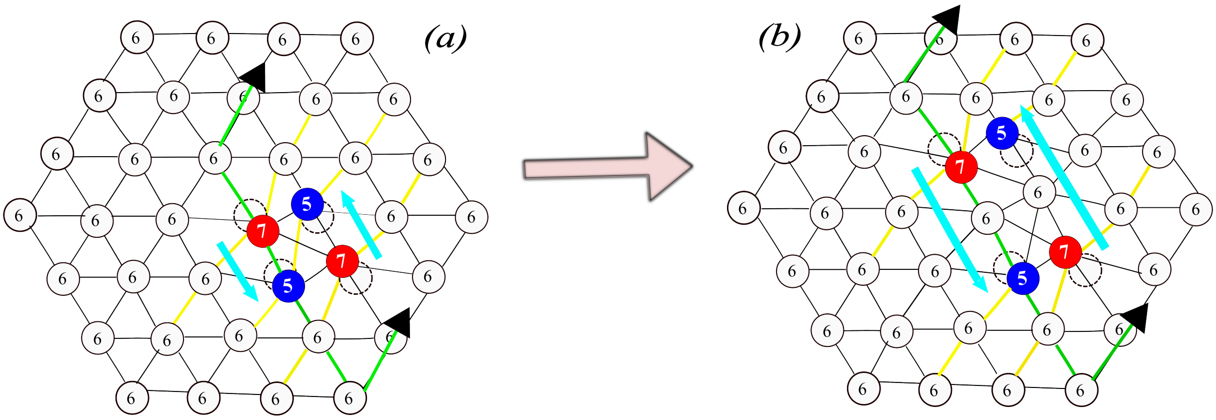

Figure 1.5 Figure (a) presents dislocation-pair inside a solid. Because of thermal fluctuations, particles are displaced from their equilibrium positions. In the process two particles loose one of their neighbor in each and as a result the other two particles accompanied with an additional neighbor. This distortion generates local stress in the system and is represented by blue vectors. At sufficient high temperature the thermal energy overcomes this stress and in order to increase local stress field, the dislocation-pair get dissociated into two free dislocations. Figure (b) represent the state of free dislocations. The alignment of green color vectors with the black head around the distorted area, shows orientation in the crystal remains unaffected in the presence of both paired and free dislocations.

Taking disclinations, another class of topological defects, into consideration brings more general equation on the table. Isolated five-fold and seven-fold defects comes under this class of defects. Fig. 1.6 shows the generation of these defects in an otherwise perfect triangular lattice. It is done by twisting the two sides of the Volterra cut relative to each other through angles $+\pi/3$ and $-\pi/3$. A rotation by $+\pi/3$, leads to the five-fold defect (positive disclination) and, rotation by -$\pi/3$ generates a seven-fold defect(negative disclination). In solids, disclinations interact very strongly, the interaction energy is proportional to the square of their separation $|\mathbf{r}_{ij}|^2$. As a results disclinations appear in the form of bounded dislocations in solids. In hexatic phase, due to screening by dislocations, the effectiveness of the interaction gets lowered and it takes logarithmic form. To explain residual anisotropy in hexatic phase, Halperin and Nelson proposed a phenomenological Hamiltonian

$$H_A = \frac{1}{2} K_A \int d^2 r (\nabla \theta(\mathbf{r}))^2 \tag{1.20}$$

with $K_A = \frac{2E_c a^2}{a_0^2}$, is a rotational stiffness constant known as 'Frank constant'. $\theta(\mathbf{r})$ gives the local orientation field

$$\theta(\mathbf{r}) = \frac{1}{2}\left(\frac{\partial u_y}{\partial x} + \frac{\partial u_x}{\partial y}\right) \tag{1.21}$$

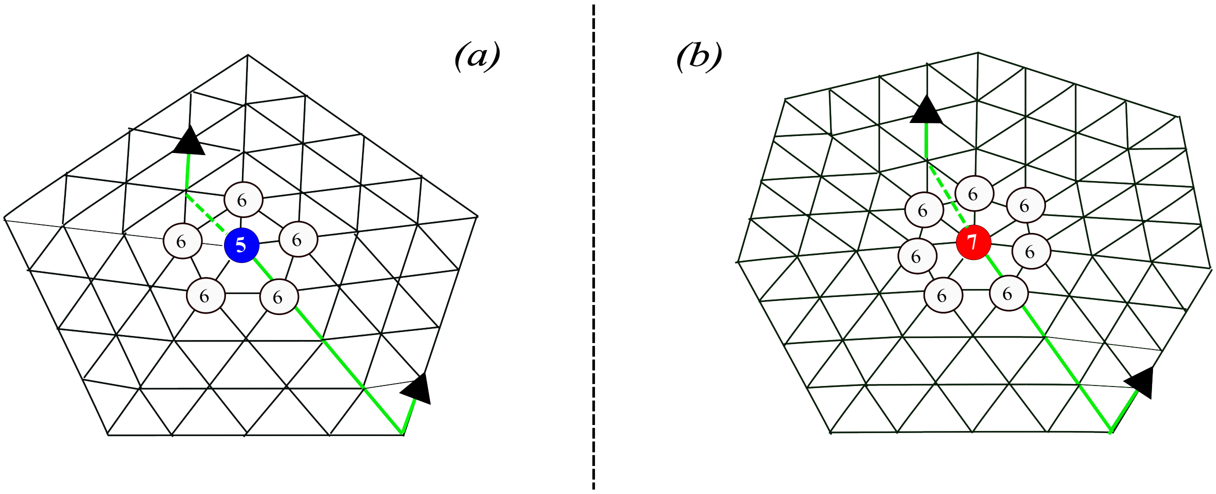

Figure 1.6 Figure (a) and (b) represent generation of a free five-fold and seven-fold defect in an otherwise perfect triangular lattice respectively. These isolated defects can be generated by twisting the two sides of the Volterra-cut through angles $\pm\pi/3$ relative to each other. The five-fold defect known to be positive disclination, is produced as a result of rotation through $+\pi/3$ and the rotation through $-\pi/3$ creates seven-fold defect also known as negative disclination. Note that the presence of disclinations breaks the orientational order of the system as green vectors around these defects are not in the same direction.

The contour integral of rotation angle Eq. (1.21), around a closed path enclosing a disclination at position **r** satisfies the condition

$$\oint d\theta(\mathbf{r}) = -\left(\frac{2\pi}{6}\right) s \tag{1.22}$$

with s being ±1, ±2... The minus sign is for calculating integration in counter clockwise direction.

In a system with both dislocations and disclination, defects from different class can also interact with one another. The Hamiltonian of such a mixed system in Fourier space takes the form

$$H_{dd} = \frac{K}{2}\int \frac{d^2q}{(2\pi)^2}\,\frac{1}{q^4}\,\tilde{s}(\mathbf{q})\tilde{s}(\text{-}\mathbf{q}) + E_c\sum_i b_i^2 + E_s\sum_i s_i^2 \tag{1.23}$$

Here, E_s is the disclination core energy. The expression of the Hamiltonian above, is subjected to the both translational and rotational displacement field equations: Eq. (1.15) and Eq. (1.22). The term $\tilde{s}(\mathbf{q})$ in Eq. (1.23) is the total defect density in Fourier space, which includes contributions from both dislocations $\mathbf{b}(\mathbf{q})$, and disclinations $s(\mathbf{q})$ density terms, which are

$$s(\mathbf{q}) = \sum_i s_i e^{-\imath\mathbf{q}\cdot\mathbf{r}_i} \tag{1.24}$$

$$\mathbf{b}(\mathbf{q}) = \sum_i \mathbf{b}_i e^{-\imath\mathbf{q}\cdot\mathbf{r}_i} \tag{1.25}$$

The inverse Fourier transforms of Eq. (1.24) and Eq. (1.25) are $s(\mathbf{r}) = \sum_i s_i\delta(\mathbf{r}-\mathbf{r}_i)$, with $s_i = \pm 1$ and $\mathbf{b}(\mathbf{r}) = \sum_i \mathbf{b}_i\delta(\mathbf{r}-\mathbf{r}_i)$, which give distribution of disclinations and dislocations respectively in real space.

From the expression Eq. (1.23), one can deduce the dislocation Hamiltonian term Eq. (1.16) by setting $s(\mathbf{r}) = 0$. To obtain disclination Hamiltonian, all that needs to be done is to equate $\mathbf{b}(\mathbf{r})$ to the zero. Similar to the dislocation case, energy of single disclination also diverges with system size but as R^2. However, for a pair of disclination with opposite and equal weight factor this divergence vanishes. The disclination Hamiltonian in the hexatic phase takes the form

$$H_{disc} = K_A\left(\frac{\pi}{3}\right)^2\int \frac{d^2q}{(2\pi)^2}\,\frac{1}{q^2}\,s(\mathbf{q})\cdot s(\text{-}\mathbf{q}) + E_s\sum_i s^2(\mathbf{r}_i) \tag{1.26}$$

which in the real space is,

$$H_{disc} = -\frac{\pi K_A(T)}{36}\sum_{i\neq j} s(\mathbf{r}_i)s(\mathbf{r}_j)\ln\frac{|\mathbf{r}_i-\mathbf{r}_j|}{a} + E_s\sum_i s^2(\mathbf{r}_i) \tag{1.27}$$

From Eqs. (1.16) and (1.27), we can observe that the defects in both dislocation-pair and disclination pair attract each other. Ignoring the angular part of Eq. (1.16), allows us to assign a common potential form for both types of defect-pairs which is

$$\beta U(r) = C_d \ln(r/r_c) \tag{1.28}$$

Here, the constant C_d takes the value $\frac{\beta K a_0^2}{4\pi}$ for a dislocation pair and $\frac{\beta K_A \pi}{18}$ for a disclination pair.

The unbinding conditions of topological defects which lead to the two step melting transition, can be obtained by calculating mean square distance between pair-particles using the interaction potential Eq. (1.28)

$$\langle r^2 \rangle = \frac{\int d^2 r r^2 e^{-\beta U(r)}}{\int d^2 r e^{-\beta U(r)}} = \frac{2-c}{4-c} a_0^2 \tag{1.29}$$

which diverges $\langle r^2 \rangle \to \infty$ as $c \to 4$.

Thus the temperature T_m at which dislocation-pair unbinds, can be obtained by equating the corresponding C_d value to the 4 which gives,

$$k_{\mathrm{B}} T_m = \frac{K a_0^2}{16\pi} \tag{1.30}$$

Similarly, the disclination unbinding temperature T_i results from the condition

$$k_{\mathrm{B}} T_i = \frac{K_A \pi}{72} \tag{1.31}$$

The Eq. (1.30) and Eq. (1.31) relate the transition temperatures T_m and T_i to the Young Modulus $K(T)$ and Frank Constant $K_A(T)$.

To summarize 'BKTHNY' theory considers two stiffness parameters. First is 'Young' modulus $K(T)$ which is associated with the translational rigidity of the solids and the other one is 'Frank constant' $K_A(T)$ which determines the rotational stiffness of the hexatic phase. The main concept behind melting process is that as the temperature approaches to the transition point T_m, the term K(T)/T lowers and at $T = T_m$ it becomes small enough to allow dislocation-pairs to get unbind. At this point solid melts into hexatic phase. At the next step $T = T_i$, the term $K_A(T)/T$ becomes small enough and permits unbinding of disclination-pairs. At this step, hexatic melts into a completely isotropic liquid phase with continuous translational and rotational symmetries in it.

One point to be noted here is, while constructing the disclination Hamiltonian, screening effect from the dislocation was taken care of. But no such consideration was taken into account for dislocation Hamiltonian. Halperin and Nelson addressed this point and modified the Hamiltonian term Eq. (1.15), with

$$H = H_0 + H_D = \frac{1}{2}\int d^2r(\lambda\phi_{ii}^2 + 2\mu\phi_{ij}^2) \tag{1.32}$$

here H_0 is the Hamiltonian for a defect-free solids and H_D brings contribution from the dislocations. Using renormalized values of Lamé-coefficients λ_R and μ_R, they put (H_0 + H_D) in a single form $H_0(\lambda_R, \mu_R)$ and, this effective Hamiltonian accounts softening of the solids by both the factors : temperature and the presence of dislocations in it.

In the unbinding condition for dislocation-pair the Young-modulus K(T) gets replaced by renormalized modulus $K_R(T)$ and the Eq. (1.30) takes the form

$$k_\mathrm{B}T_m = \frac{K_R a_0^2}{16\pi} \tag{1.33}$$

This is the universal condition for the 2D solids melting. The transition points are identified as the boundary points which separates stable phases from the unstable ones. The exponent in the positional correlation function depends on the renormalized Lamé coefficients as

$$\eta_G = \left(\frac{k_\mathrm{B}T}{\pi\mu_R a_0^2}\right)\frac{3\mu_R + \lambda_R}{2\mu_R + \lambda_R} \tag{1.34}$$

For stable solids, the upper-bound of decaying exponent is predicted at $\eta_G = 1/3$. The exponent in the orientational correlation function η_6 is related to the Frank constant as

$$\eta_6 = \frac{18k_\mathrm{B}T}{\pi K_A} \tag{1.35}$$

and its upper bound value at the liquid-hexatic transition point is predicted to be $\eta_6 = 1/4$.

1.3 System under constant confinement

In common practice, 2D layers do not appear as independent entities. To do so, the constituent particles need to get confined on crystalline surfaces. To understand the substrate potential role, it becomes essential to study the 2D systems under the influence of external potential. The photo-lithography and the optical tweezers are the two main techniques which have been using to create the substrate potential. But it is the later one that provides more convenience in terms of tuning the applied potential strength and the periodicity. The optical tweezer is a technique for trapping the micron and nano-sized particles with a laser beam and was first introduced by Arthur Ashkin in 1970[78]. For this discovery, he got the 2018 Nobel Prize in physics with Gerard Mourou and Donna Strickland.

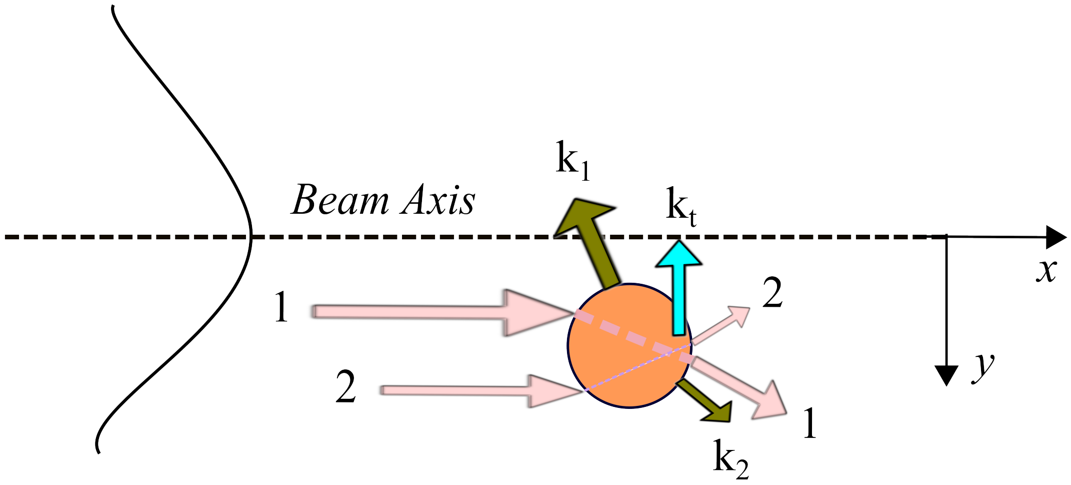

Figure 1.7 Sketch representing the trapping of a suspended particle on the center axis of a focused light beam. k_1 and k_2 are the momenta that the particle experiences because of the outgoing refracted rays '1' and '2' respectively. K_t is their resultant momentum and is in upward (-y) direction.

A. Ashkin found that when a light beam strikes on a suspended particle having a refractive index greater than that of the medium, particle gets attracted towards the center of the light beam. The reason behind this lies in the fact that light carries momentum with it and therefore exerts a force on the particle (see Fig. 1.7). There are two kinds of forces a particle feels when a beam of light strikes on it. One coming from the reflection of the light called *scattering force* pushes the particle in the direction of its propagation. The other is due to the refraction of the light and is termed as *gradient force*. Since the intensity profile of the beam is Gaussian in nature, the resultant *gradient force* works upwardly (in -y direction) and traps the particle on the center axis. In his experiment, Ashkin also got able to hold the particle at a single spot using another light beam originating from the opposite direction.

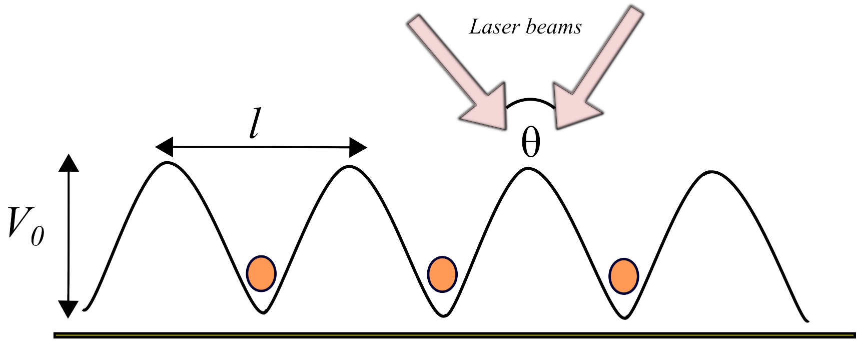

Figure 1.8 Schematic representation of particles confined between the troughs of a periodic optical potential.

Based on this aspect of light, the first experimental realization of the interacting 2D colloids under the influence of 1D optical potential, came in 1985 by A. Chowdhury et al[79]. The standing wave pattern of the potential, obtained by the interference of two laser beams at an angle θ was used to trap the particles at the troughs of the potential Fig. 1.8. The periodicity of the potential was tuned with the mean interparticle spacing a of the colloids. In the liquid phase at $V_0 = 0$, they observed a transition into a solid phase, upon increasing the intensity of the laser beams. This phenomenon has been known as '*Laser Induced Freezing*' (LIF).[80–86] Later in 1998, Wei *et. al.* observed that on further increasing the intensity, the solid phase melts into liquid phase again and this phenomenon was termed as '*Laser Induced Melting*' (LIM)[87].

The presence of the external potential explicitly breaks the continuous 2D rotational symmetry of the system. The translational symmetry in the direction of the potential also gets discretized following the periodicity of the potential. In liquid phase under the influence of periodic potential, the particles are allowed to diffuse freely only in the perpendicular direction of the potential. This phase is referred to be '*Modulated liquid*' and its characterization factors are: vanishing shear modulus, presence of unbound dislocations and absence of massless Goldstone modes. The density modulation in both directions can also be done using three or four laser beams and was achieved by Brunner and Bechinger in 2002.

Having an additional control parameter in the form of the external potential provides more insight into the topic of phase transition for 2D systems. It is found that unlike the spontaneous case, in the presence of the potential, there can be two kinds of solid phases: '*Floating Solid*' and '*Locked Floating Solid*'[88,89]. The *Floating Solid Phase* differs from the *Locked Solid Phase* as it can slide across the troughs of the potential and in many ways resembles with the pure 2D phase (in the absence of the potential). It has also been observed that depending upon the commensuration ratio between the periodicity of the potential and interparticle spacing, an intermediate *'Locked Schematic Phase'* appears in the melting process from the *Locked Floating Solid* into *Modulated Liquid* phase. The *Locked Smectic Phase* is characterized by the short-range translational order in the neighboring troughs with a lowered symmetry in comparison of *Modulated Liquid Phase*.

1.4 Brownian Ratchets

A Brownian ratchet is a device that is designed to rectify the thermal fluctuations from its environment to produce directed motion (or say useful work). It requires the presence of three elements: 1^{st} a fluctuating environment, 2^{nd} appropriate asymmetry 3^{rd} and the essential one, keeping the system out of thermal equilibrium. At present, the concept of Brownian ratchet is also being used to understand the molecular process of motor proteins in biological systems. New artificial proteins have started to made using this concept.

Its idea was originated in 1950 by L. Brillouin[90]. In an electric circuit consisting of a diode (rectifier) and a resister, he inquired, whether the diode can be used to rectify thermal fluctuations available in the resistor and thus in producing a direct voltage. The phenomenon is known as the 'Brillouin paradox'. Based on this concept, Smoluchowsky and Feynman analyzed a mechanical device which involves a ratchet (notched wheel) and a pawl. In both of these cases, the generation of useful work is inhibited by the second law of thermodynamics. In the following sections, it is explained how the second law of thermodynamics averts the generation of directed motion in a system if it is kept at thermal equilibrium.

1.4.1 Feynman Ratchet: A mechanical rectifier

It was Richard Feynman's intuitive attempt of extracting useful work from the random motion of gas molecules using ratchet and pawl system.[91] The thermal energy keeps the molecules in constant motion. The set-up of such a device is shown in the Fig. 1.9. Two cases are presented here, one in which the two gas containers are at thermal equilibrium and in the other non-equilibrium scenario is discussed.

1^{st} *Case*: **Both Gas Containers at the same temperature** i.e. $T_1 = T_2$

The continuous collision of gas molecules from random directions makes the vanes

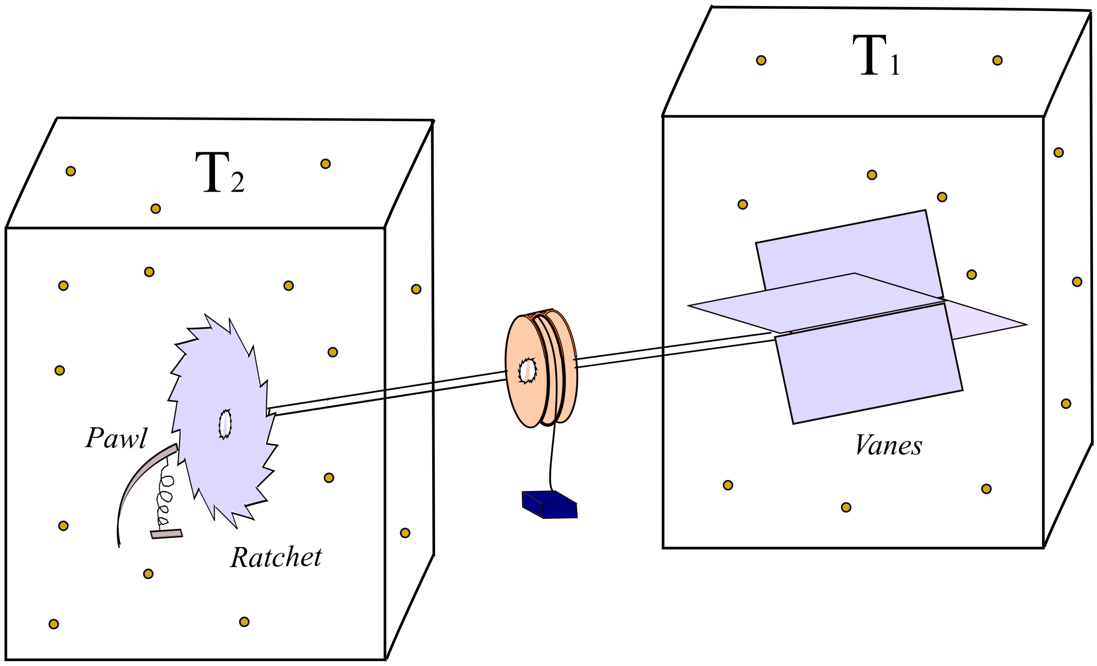

Figure 1.9 A schematic representation of Feynman Ratchet device. It consists of a rod with vanes attached to it at one end, and a ratchet wheel at the other end. The wheel is in contact with a pawl, which is held by a piece of spring. The presence of pawl makes the ratchet wheel to move only in one direction. Both ends of the rod are placed inside the containers of gas. The temperatures of the two containers are T_1 and T_2.

to rotate in both clockwise as well as in anti-clockwise directions. The connection of vanes with the ratchet wheel tries to rotate it also accordingly. The device is built in such a manner that, the pawl allows the ratchet wheel to move only in the clockwise direction. Each time when the wheel attempts to rotate anti-clockwise, it pushes the pawl dawn, and the motion gets jammed.

On the other hand, when the wheel gets a push to move in the clockwise direction, the notch on the wheel pushes the pawl upwards and proceeds one step further. After the pawl gets crossed by the notch, it looks for the next notch to fall back on. This is where the role of spring comes into the picture. A pure elastic spring will lead to indefinite bouncing of the pawl and hence will create chances to slip the notch accidentally underneath the pawl. Therefore, to make the pawl stick on the wheel, an inelastic damped bouncing is required. Now the set up looks done for producing a perpetual motion in a single direction we can use it in lifting a box against gravity.

Will it manage to pull the box up? Well, both source and system are working at the same temperature, and the system is performing work without losing any part of the gained heat, violating the second law of thermodynamics. The thing we have overlooked here is the pawl is also subjected to the random bombardment by the gas molecules. There is an equal probability that the pawl lifts not because of the push from notch but by the bombardment of gas molecules itself. In such a situation, the wheel can move in the anti-clockwise direction as well, and thus the motion in a single direction gets canceled out

One other point is that, as a damped spring is used, the pawl will produce heat out of friction, each time when it falls on the notch. Thus the temperature of its surroundings will increase gradually and the gas molecules will hit the pawl more randomly with greater thermal energy. Because of this increased energy pawl will start to move up and down to a greater extent. If it falls on the inclined plane, it will drag the wheel to slip anti-clockwise and if it falls on the other plane, it will push it in the opposite direction. Thus the wheel which is designed to move in the clockwise direction will end up moving in the opposite direction. Again no unidirectional motion will be achieved in long duration of time.

A more general explanation of the question: "why thermal equilibrium prevents rectification from occurring", can be understood by the arguments, based on the concepts of symmetry and detailed balance. L. Boltzmann introduced the concept of detailed balance to prove H-theorem. According to it, at thermal equilibrium, each process is equilibrated by its reverse process. The equations which govern the microscopic world follow time-reversal symmetry. Therefore, in a mechanical rectifier device at thermal equilibrium, the forward and the backward motion will be equally probable for the course of a long-time period.

2^{nd}*Case*: The Gas Containers at different temperatures T_1 and T_2

The only way of producing unidirectional motion in such an aforementioned device requires to keep the two containers at different temperatures. As the system no longer remains at thermal equilibrium, the generation of rectified motion is allowed in this case.

1.4.2 Mathematical Model for the generation of directed motion

In the previous section, we have discussed that the rectification of fluctuation requires the system to be taken out of equilibrium. In the Feynman ratchet device, it was done by keeping the two parts -: the vanes and the ratchet wheel at two different temperatures. One thing to be noticed here is that at room temperature, the order of thermal energy is around 4×10^{-21} Joule. This energy is quite small to influence the device, made up at the macro scale. So to observe the results of rectification, the device must be built at the micro-scale. However, to build a mechanical device, operating between two heat reservoirs at the micro-scale is quite complicated.

In this section, we will discuss one of the mathematical model 'flashing ratchet', introduced by Ajdari and Prost in 1992[92], which explains the working principle for the Brownian ratchets. The flashing ratchet is a device that rectifies thermal fluctuations originating from a single temperature source. It involves an external potential, and as the name 'flashing' is referring, this potential keeps on appearing and disappearing in a cycle as time goes on.

To understand the flashing ratchet model, let us look at the dynamics of a Brownian particle under the influence of time-dependent ratchet potential, in one-dimensional space. The ratchet potential is spatially asymmetric and periodic $V(x+L) = V(x)$. The picture of such a system can be viewed in Fig. 1.10.

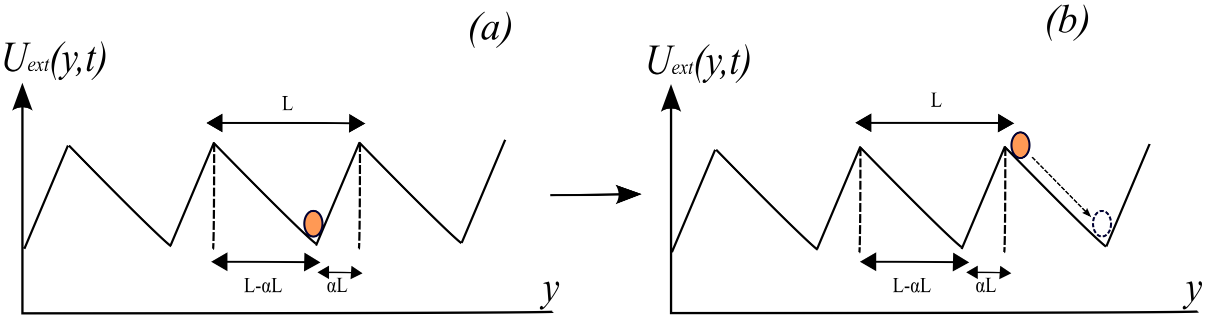

Figure 1.10 Sketch representing the dynamics of a Brownian particle in the presence of one dimensional, time dependent ratchet potential. The potential has the periodicity 'L' and changes its state between $'On'$ and $'Off'$ phases with time. The parameter α controls the spatial asymmetry. For $\alpha < 1.0$ the distance between a minima and its consecutive maxima in the forward (+y) direction (αL) becomes smaller than the distance which it shares with the maxima in backward (-y) direction ($L - \alpha L$).

Mathematically, directed motion can be expressed as the statistical average of the velocity,

$$\langle v \rangle = \lim_{t\to\infty} \frac{1}{t} \int_0^t dt' \langle \frac{dx(t')}{dt} \rangle = \lim_{t\to\infty} \frac{\langle x(t) - x(0) \rangle}{t} \tag{1.36}$$

In the presence of heat bath, the equation of motion of the Brownian particle of mass 'm' can be formulated as

$$m\frac{d^2x}{dt^2} = -\gamma\frac{dx}{dt} - \frac{\partial V(x)}{\partial x} + \xi(t) \tag{1.37}$$

This is the famous 'Langevin equation'. Here, γ is the friction coefficient, V(x) is the external ratchet potential, and $\xi(t)$ is the random force. The random force $\xi(t)$ has $\langle \xi(t) \rangle = 0$ and is delta correlated $\langle \xi(t)\xi(t') \rangle = 2k_{\mathrm{B}}T\gamma\delta(t-t')$.

Most of the experimental realizations follow the over-damped dynamics of the Brownian particle. In this case, the time scale obtained by m/γ, appears to be very small in comparison of any other time-scale. So dropping the 1^{st} term (the inertial part) from the Eq. (1.37) gives

$$\gamma\frac{dx}{dt} = -\frac{\partial V(x)}{\partial x} + \xi(t) \tag{1.38}$$

Under the $'On'$ state of the potential with $k_{\mathrm{B}}T \ll V(x)$, the particle does not get enough energy to overcome the potential barrier height and remains trapped at the bottom of the potential well. On the other hand, During $'Off'$ state, it diffuses freely and the Eq. (1.38) becomes

$$\gamma\frac{dx}{dt} = \xi(t) \tag{1.39}$$

which leads to the mean square displacement

$$\langle [x(t) - x(0)]^2 \rangle = 2D\tau_{off} \tag{1.40}$$

Here D is the Diffusion coefficient and has the value $k_{\mathrm{B}}T/\gamma$.

With $'\tau'_{off}$ satisfying the condition

$$\frac{(\alpha L)^2}{2D} \simeq \tau_{off} \ll \frac{(1-\alpha)^2 L^2}{2D} \tag{1.41}$$

particle covers a distance which is $\geq \alpha L$ but $< L(1-\alpha)$. This condition allows the particle to cross the potential maxima of right side but not to the one at left.

Hence in the $'On'$ state, there becomes a larger probability of finding the particle near the top of the potential well at right side Fig. 1.10 (b). Now in this well, the particle feels a force $V_0/(1-\alpha L)$, that retraps it at the bottom of the well in the time period given by

$$\tau_{on} \geq \frac{\gamma(1-\alpha)^2 L^2}{V_0} \tag{1.42}$$

There is also a possibility that the particle does not shifts its position while remaining in the same well during the $'Off'$ state of the potential. However, the possibility of its shifting to the left well will always remain negligible. Thus on repeating the cycle of switching the potential states sets an averaged directed motion in the forward (+y) direction. It should be noted that the switching of the ratchet potential states, requires sustained energy input and the thermal energy is not the only source of the total energy input here.

The first experimental realization of Brownian ratchet for colloidal particles was done by Rousselet *et. al.* in 1994[93]. They implemented the flashing ratchet model on Polystyrene latex spheres of diameter in the range 0.25 μm to 1 μm. A flashing ratchet can also produce averaged directed current by the random switching of potential between $'On'$ and $'Off'$ states. Based on this aspect, we have studied the dynamics and associated structural changes in a two-dimensional colloidal system in the presence of a one-dimensional ratchet potential. The directed current induces a melting of the triangular solid into a hexatic phase. The details of this melting scenario is discussed in Chapter 4.

Bibliography

[1] L. D. Landau, *Zh. Eksp. Teor. Fiz.*, 1937, **7**, 19–32.

[2] L. D. Landau, *Phys. Z. Sowjet.*, 1937, **11**, 545.

[3] W. W. Wood and J. D. Jacobson, *The Journal of Chemical Physics*, 1957, **27**, 1207–1208.

[4] B. J. Alder and T. E. Wainwright, *The Journal of Chemical Physics*, 1957, **27**, 1208–1209.

[5] B. J. Alder and T. E. Wainwright, *The Journal of Chemical Physics*, 1959, **31**, 459–466.

[6] B. J. Alder and T. E. Wainwright, *The Journal of Chemical Physics*, 1960, **33**, 1439–1451.

[7] B. J. Alder and T. E. Wainwright, *Phys. Rev.*, 1962, **127**, 359–361.

[8] H. E. Stanley and T. A. Kaplan, *Phys. Rev. Lett.*, 1966, **17**, 913–915.

[9] J. R. Clow and J. D. Reppy, *Phys. Rev. Lett.*, 1967, **19**, 291–293.

[10] G. Kukich, R. P. Henkel and J. D. Reppy, *Phys. Rev. Lett.*, 1968, **21**, 197–200.

[11] D. Amit, *Physics Letters A*, 1968, **26**, 448 – 449.

[12] D. Amit, *Physics Letters A*, 1968, **26**, 466 – 467.

[13] H. E. Stanley, *Phys. Rev. Lett.*, 1968, **20**, 589–592.

[14] R. S. Kagiwada, J. C. Fraser, I. Rudnick and D. Bergman, *Phys. Rev. Lett.*, 1969, **22**, 338–342.

[15] R. P. Henkel, E. N. Smith and J. D. Reppy, *Phys. Rev. Lett.*, 1969, **23**, 1276–1279.

[16] M. A. Moore, *Phys. Rev. Lett.*, 1969, **23**, 861–863.

[17] J. M. Kosterlitz and D. J. Thouless, *Journal of Physics C: Solid State Physics*, 1972, **5**, L124–L126.

[18] M. Chester, L. C. Yang and J. B. Stephens, *Phys. Rev. Lett.*, 1972, **29**, 211–214.

[19] J. M. Kosterlitz, *Journal of Physics C: Solid State Physics*, 1974, **7**, 1046–1060.

[20] Y. P. Monarkha and V. B. Shikin, *Soviet Journal of Experimental and Theoretical Physics*, 1975, **41**, 710.

[21] D. S. Fisher, B. I. Halperin and P. M. Platzman, *Physical Review Letters*, 1979, **42**, 798–801.

[22] E. Andrei, *Two-Dimensional Electron Systems: On Helium and Other Cryogenic Substrates*, Springer Netherlands, 1997.

[23] A. Alexandrov and J. Devreese, *Advances in Polaron Physics*, Springer Berlin Heidelberg, 2009.

[24] V. L. Berezinsky, *Sov.Phys.JETP*, 1970, **59**, 907–920.

[25] V. L. Berezinsky, *Sov.Phys.JETP*, 1972, **34**, 1144–1156.

[26] J. M. Kosterlitz and D. J. Thouless, *J. Phys.*, 1973, **C6**, 1181–1203.

[27] B. I. Halperin and D. R. Nelson, *Phys. Rev. Lett.*, 1978, **41**, 121–124.

[28] D. R. Nelson and B. I. Halperin, *Phys. Rev. B*, 1979, **19**, 2457–2484.

[29] A. P. Young, *Phys. Rev. B*, 1979, **19**, 1855–1866.

[30] K. J. Strandburg, in *Bond-Orientational Order in Condensed Matter Systems. Partially Ordered Systems.*, ed. K. J. Strandburg, Springer-Verlag, New York, NY, 1992, ch. 2, pp. 32–77.

[31] C. A. Murray, in *Bond-Orientational Order in Condensed Matter Systems. Partially Ordered Systems.*, ed. K. J. Strandburg, Springer-Verlag, New York, NY, 1992, ch. 4, pp. 137–215.

[32] J. V. José, *40 Years of Berezinskii-Kosterlitz-Thouless Theory*, WORLD SCIENTIFIC, 2013.

[33] J. M. Kosterlitz, *Reports on Progress in Physics*, 2016, **79**, 026001.

[34] V. N. Ryzhov, E. E. Tareyeva, Y. D. Fomin and E. N. Tsiok, *Physics-Uspekhi*, 2017, **60**, 857–885.

[35] A. T. Skjeltorp, *Phys. Rev. Lett.*, 1983, **51**, 2306–2309.

[36] C. A. Murray and D. H. Van Winkle, *Phys. Rev. Lett.*, 1987, **58**, 1200–1203.

[37] Y. Tang, A. J. Armstrong, R. C. Mockler and W. J. O'Sullivan, *Phys. Rev. Lett.*, 1989, **62**, 2401–2404.

[38] A. J. Armstrong, R. C. Mockler and W. J. O'Sullivan, *Journal of Physics: Condensed Matter*, 1989, **1**, 1707–1730.

[39] C. A. Murray and R. A. Wenk, *Phys. Rev. Lett.*, 1989, **62**, 1643–1646.

[40] C. A. Murray, D. H. V. winkle and R. A. Wenk, *Phase Transitions*, 1990, **21**, 93–126.

[41] C. A. Murray, W. O. Sprenger and R. A. Wenk, *Phys. Rev. B*, 1990, **42**, 688–703.

[42] Y. Tang, A. J. Armstrong, R. C. Mockler and W. J. O'Sullivan, *Phase Transitions*, 1990, **21**, 75–92.

[43] W. V. Megen, P. N. Pusey and P. Bartlett, *Phase Transitions*, 1990, **21**, 207–227.

[44] R. E. Kusner, J. A. Mann, J. Kerins and A. J. Dahm, *Phys. Rev. Lett.*, 1994, **73**, 3113–3116.

[45] R. E. Kusner, J. A. Mann and A. J. Dahm, *Phys. Rev. B*, 1995, **51**, 5746–5759.

[46] K. Zahn and G. Maret, *Phys. Rev. Lett.*, 2000, **85**, 3656–3659.

[47] H. H. von Grünberg, P. Keim, K. Zahn and G. Maret, *Phys. Rev. Lett.*, 2004, **93**, 255703.

[48] P. Keim, G. Maret and H. H. von Grünberg, *Phys. Rev. E*, 2007, **75**, 031402.

[49] P. Dillmann, G. Maret and P. Keim, *Journal of Physics: Condensed Matter*, 2008, **20**, 404216.

[50] L. Assoud, F. Ebert, P. Keim, R. Messina, G. Maret and H. Löwen, *Phys. Rev. Lett.*, 2009, **102**, 238301.

[51] E. P. Bernard and W. Krauth, *Phys. Rev. Lett.*, 2011, **107**, 155704.

[52] M. Engel, J. A. Anderson, S. C. Glotzer, M. Isobe, E. P. Bernard and W. Krauth, *Phys. Rev. E*, 2013, **87**, 042134.

[53] J. J. Alonso and J. F. Fernández, *Phys. Rev. E*, 1999, **59**, 2659–2663.

[54] K. Wierschem and E. Manousakis, *Phys. Rev. B*, 2011, **83**, 214108.

[55] M. Zu, J. Liu, H. Tong and N. Xu, *Phys. Rev. Lett.*, 2016, **117**, 085702.

[56] H. Zhang, S. Peng, L. Mao, X. Zhou, J. Liang, C. Wan, J. Zheng and X. Ju, *Phys. Rev. E*, 2014, **89**, 062410.

[57] O. S. Vaulina and X. G. Koss, *Physics Letters A*, 2009, **373**, 3330–3335.

[58] O. Vaulina and E. Vasilieva, *Physics Letters A*, 2014, **378**, 719–722.

[59] D. E. Dudalov, Y. D. Fomin, E. N. Tsiok and V. N. Ryzhov, *Phys. Rev. Lett.*, 2014, **112**, 157803.

[60] W.-K. Qi, S.-M. Qin, X.-Y. Zhao and Y. Chen, *Journal of Physics: Condensed Matter*, 2008, **20**, 245102.

[61] S. C. Kapfer and W. Krauth, *Phys. Rev. Lett.*, 2015, **114**, 035702.

[62] S. Z. Lin, B. Zheng and S. Trimper, *Phys. Rev. E*, 2006, **73**, 066106.

[63] H. Weber, D. Marx and K. Binder, *Phys. Rev. B*, 1995, **51**, 14636–14651.

[64] K. Chen, T. Kaplan and M. Mostoller, *Phys. Rev. Lett.*, 1995, **74**, 4019–4022.

[65] Y. Saito, *Phys. Rev. B*, 1982, **26**, 6239–6253.

[66] W. Qi and M. Dijkstra, *Soft Matter*, 2015, **11**, 2852–2856.

[67] W. Qi, A. P. Gantapara and M. Dijkstra, *Soft Matter*, 2014, **10**, 5449–5457.

[68] P. Bladon and D. Frenkel, *Phys. Rev. Lett.*, 1995, **74**, 2519–2522.

[69] A. Hajibabaei and K. S. Kim, *Phys. Rev. E*, 2019, **99**, 022145.

[70] J. A. Anderson, J. Antonaglia, J. A. Millan, M. Engel and S. C. Glotzer, *Phys. Rev. X*, 2017, **7**, 021001.

[71] J. F. Fernández, J. J. Alonso and J. Stankiewicz, *Phys. Rev. Lett.*, 1995, **75**, 3477–3480.

[72] K. Binder, S. Sengupta and P. Nielaba, *Journal of Physics: Condensed Matter*, 2002, **14**, 2323–2333.

[73] S. T. Chui, *Phys. Rev. Lett.*, 1982, **48**, 933–935.

[74] S. T. Chui, *Phys. Rev. B*, 1983, **28**, 178–194.

[75] M. A. Glaser and N. A. Clark, in *Melting and Liquid Structure in two Dimensions*, John Wiley & Sons, Ltd, 2007, pp. 543–709.

[76] R. Peierls, *Annales de l'institut Henri Poincaré*, 1935, **5**, 177–222.

[77] N. D. Mermin and H. Wagner, *Phys. Rev. Lett.*, 1966, **17**, 1133–1136.

[78] A. Ashkin, *Phys. Rev. Lett.*, 1970, **24**, 156–159.

[79] A. Chowdhury, B. J. Ackerson and N. A. Clark, *Phys. Rev. Lett.*, 1985, **55**, 833–836.

[80] A. Ricci, P. Nielaba, S. Sengupta and K. Binder, in *Computer Simulation of Models for Confined Two-Dimensional Colloidal Crystals: Evidence for the Lack of Positional Long Range Order*, 2009, pp. 149–154.

[81] F. Bürzle and P. Nielaba, *Physical review. E, Statistical, nonlinear, and soft matter physics*, 2007, **76**, 051112.

[82] P. Nielaba, S. Sengupta and W. Strepp, in *Phase Transitions of Model Colloids in External Fields*, 2007, vol. 704, pp. 163–189.

[83] A. Ricci, P. Nielaba, S. Sengupta and K. Binder, *Physical review. E, Statistical, nonlinear, and soft matter physics*, 2007, **75**, 011405.

[84] A. Ricci, P. Nielaba, S. Sengupta and K. Binder, *Physical review. E, Statistical, nonlinear, and soft matter physics*, 2006, **74**, 010404.

[85] W. Strepp, S. Sengupta and P. Nielaba, *Physical review. E, Statistical, nonlinear, and soft matter physics*, 2002, **66**, 056109.

[86] W. Strepp, S. Sengupta and P. Nielaba, *Physical review. E, Statistical, nonlinear, and soft matter physics*, 2001, **63**, 046106.

[87] Q.-H. Wei, C. Bechinger, D. Rudhardt and P. Leiderer, *Phys. Rev. Lett.*, 1998, **81**, 2606–2609.

[88] E. Frey, D. R. Nelson and L. Radzihovsky, *Phys. Rev. Lett.*, 1999, **83**, 2977–2980.

[89] L. Radzihovsky, E. Frey and D. R. Nelson, *Phys. Rev. E*, 2001, **63**, 031503.

[90] L. Brillouin, *Phys. Rev.*, 1950, **78**, 627–628.

[91] R. Feynman, R. Leighton and M. Sands, *The Feynman Lectures on Physics, Vol I: Mainly mechanics, radiation, and heat*, Addison-Wesley, 1963.

[92] A. Ajdari, J. Prost and L. Peliti, *Phys. Rev. Lett.*, 1992, **69**, 861–861.

[93] J. Rousselet, L. Salome, A. Ajdari and J. Prost, *Nature*, 1994, **370**, 446.

2

Phase transition in a system of two-dimensional colloids interacting via inverse twelfth power potential.

A molecular dynamic study of melting transition for a system of monodispered repulsively interacting colloidal dispersion in two dimensions is presented. The relevant physical quantities necessary to study melting in two dimensions is introduced here. The identification of the transition points and the different phases of the system is done using the pair-correlation function, static structure factor, translational order parameter, their correlation functions and their finite size scaling. The nature of transitions are obtained by calculating the spatially resolving the translational and orientational order paramter and their corresponding distributions. The melting in the system is observed to be a two step process. The solid phase at high densities melts to a hexatic phase via a continous transition, in conformation with BKTHNY theory. In contrast, a stable hexatic phase exists in the system upto a certain density, below which it melts to an isotropic liquid via a weak first order transition. We find the location of the transition points of the solid and the liquid, as well as the stable hexatic boundary in the system.

2.1 Introduction

Colloidal suspensions serve as ideal systems to study the melting scenarios in two-dimensions. They are particularly suited due to their sizes which make them amenable to experimental observations.[1–18] Additionally, the pair-interaction in such systems can be precisely tuned, and as a consequence allow us to test the different melting scenarios that has been proposed. While the Berezinskii-Kosterlitz-Thouless-Halperin-Nelson-Young (BKTHNY) theory[19–23] is very appealing, the proposed melting scenarios are not universal. Rather, the melting is dependent on pair-interaction,[24–27] particle shape,[28] pinning of particle or vacancies[29,30] and even out of plane fluctuations.[31]

Even for the simple system of hard-disks, the detailed analysis of the melting was done only a decade ago.[25] Event Chain Monte Carlo (ECMC) simulations of a system of hard-disks revealed that while the solid-hexatic transition is continuous, in agreement with the KTHNY scenario, the hexatic-liquid transition is first order.[25] The first evidence of a first-order transition came from the behaviour of the thermodynamic pressure as a function of density of the system. The authors observed a Mayer-Wood loop in the pressure-density curve, which appears as a direct consequence of the interface between the two phases - hexatic and liquid. In the density interval belonging to the co-existence regime, the distribution of local orientations mapped on the global orientation shows two separate regions of high and low orientational order.

This work was later extended to study the melting scenario in short-ranged pair potentials. For short-ranged potentials, the liquid-hexatic transition is observed to be either first order or continuous depending upon the extent of hardness they offer. For example, a system of soft-disks with repulsive power-law interaction of form $U(r) \sim r^{-n}$, exhibits a continuous liquid-hexatic transition for $n < 6$, but it becomes first-order for $n \geqslant 6$.[26]. Similarly in the system of Yukawa pair interaction, the nature of liquid-hexatic transition is found to depend upon the Debye-Huckel screening length and temperature.[26]. Although, this result has been contested in the recent work by Hajibabaei *e*t. al.[27] that showed that a hexatic-liquid transition is first order for $12 < n < 64$.

This gives us an excellent starting point to study melting in two-dimensional colloidal suspensions. We started our study by investigating the colloidal system with r^{-12} repulsive interaction. While it helped us in benchmarking our code for further research, it also gave us the opportunity to resolve the two different melting scenarios proposed in the earlier works.

The rest of the presentation is organized as follows. In Section 2.2 we present the model system and the details of the simulations. The discussion on the results of the simulation, including the identification of the different phases and the melting points are presented in Section 2.3. The nature of the solid-hexatic and the hexatic-liquid transitions are presented in Section 2.4. Finally, a brief conclusion is presented in Section 3.6.

2.2 Model and Simulation Details

We started with a mono-dispersed suspension of 512^2 colloidal particles in two-dimension, initially arranged in a perfect triangular lattice. The inter-particle distance is set by density of the system according to $a^2 = \sqrt{3}\rho/2$. Each particle interact with other particles within a cut-off radius r_c through a shifted repulsive potential of the form $\beta U(r) = (\sigma/r)^{12} - 2^{-12}$ for $r \leq r_c$ and 0 otherwise. Here, r is the particle's separation distance. The cut-off radius value r_c is taken to be 2.0σ. The parameter σ sets the length scale of the system. Molecular dynamics simulations of the system are performed in the presence of Langevin heat bath with an isotropic friction $\gamma\tau = 1$ and a bath temperature of $k_{\mathrm{B}}T/\varepsilon = 1$, where $\tau = \sigma\sqrt{m/\varepsilon}$ sets the time-scale of the system. The presence of heat bath maintains the temperature of the system at this fixed value and the corresponding Langevin equation is

$$\dot{\mathbf{p}}_i(t) = -\gamma\frac{\mathbf{p}_i(t)}{m_i} + \eta_i(t) + \mathbf{f}_{int} = \mathbf{F}_i(t) \tag{2.1}$$

Here $-\gamma_i(t)/m_i$ is the frictional force exerted by the solvent particles, $\eta_i(t)$ is random force whose mean value $\langle\eta_i(t)\rangle = 0$ and is delta correlated $\langle\eta_i(t)\eta_j(t')\rangle = 2\gamma k_{\mathrm{B}}T\delta_{i,j}\delta(t-t')$. The values of fluctuating forces are taken from a Normal distribution of width $2k_{\mathrm{B}}T\gamma/\delta t$. Here, δt is the integration time step and its value is taken to be 0.001τ. To integrate Eq. (2.1), we have used Leap-Frog algorithm. It updates particles momentum and position values according to the following equations

$$\mathbf{p}_i(t+\delta t/2) - \mathbf{p}_i(t-\delta t/2) = \delta t\mathbf{F}_i(t) \tag{2.2}$$

$$\mathbf{r}_i(t+\delta t) = \mathbf{r}_i(t) + \delta t\frac{\mathbf{p}_i(t+\delta t/2)}{m_i} \tag{2.3}$$

The system was first equilibrated for 10^8 time steps, after which statistics were collected for a further 10^7 steps.

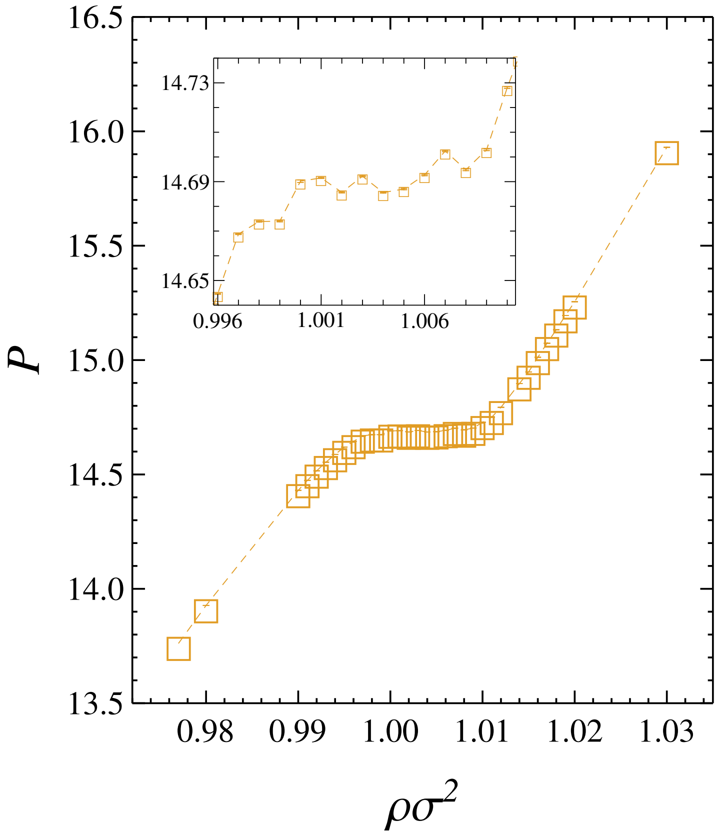

Figure 2.1 Time-averaged pressure as a function of system density is shown for the density range from $\rho\sigma^2$ = 0.978 to 1.03. There is almost a flat line of value ∼14.70 from $\rho\sigma^2$ =0.998 to 1.009. The zoomed picture of this region is highlighted in the inset plot. It shows that the pressure value actually has positive increment with density though the variation is very little ranging from the value of ∼14.65 to ∼14.73.

2.3 Solid and hexatic melting

In this section, we present a coherent discussion on the results from our simulations. The system is known to undergo a two step melting process. Accordingly, we have split the discussion based on the identification and melting of the solid and the hexatic phased. At first, we present a qualitative discussion on the melting scenario from the behavior of the thermodynamic pressure as a function of system density in Section 2.3.1. The solid melting is then qualitatively discussed using the static structure and the order parameter in Section 2.3.2. Quantitative identification of the solid phase and the melting point of the solid using the pair-correlation function and a finite size scaling of the order parameter is presented in Section 2.3.3. The identification of the hexatic phase using the orientational order parameter and its spatial correlation is presented in Section 3.3.5.

2.3.1 Thermodynamic Pressure

The thermodynamic pressure is calculated using virial expression

$$P = \frac{\rho}{\beta} + \frac{\rho}{(2N)} \sum_{i}^{N} \sum_{j>i}^{N} \mathbf{f}(\mathbf{r}_{ij}) \cdot \mathbf{r}_{ij}, \tag{2.4}$$

where ρ is the system density, β is the inverse of temperature, N is the total number of particles, $f(\mathbf{r}_{ij})$ is the interaction force and $\mathbf{r}_{ij}$ is the inter-particle separation.

The variation of pressure with the system density is shown in Fig. 2.1. The pressure-density curve exhibits the signature of three different phases-solid, hexatic and liquid. The initial monotonically increasing pressure for densities $0.978 \leq \rho\sigma^2 \leq 0.997$ belongs to the isotropic liquid phase. Since the hexatic phase immediately precedes the isotropic liquid phase, the intermediate regime of densities, $0.998 \leq \rho\sigma^2 \leq 1.01$, belongs to the hexatic phase. The thermodynamic pressure however, in the hexatic phase is neither monotonically increasing nor exhibits a plateau. Instead, its density dependence is weakly non-monotonic. While there is a lack of a distinct Mayer-Wood loop in the pressure-density curve, the weak non-monotonicity does not rule out a first-order transition from a hexatic to a liquid phase. Once the density of the system becomes larger than $\rho\sigma^2 = 1.01$, the pressure again increases monotonically with the density, corresponding to a solid phase of the system. This roughly gives us an idea of the transition points of the system – solid melting occurs close to $\rho\sigma^2 \approx 1.01$ and hexatic melting happens close to $\rho\sigma^2 \approx 0.998$. The more refined analysis of the transition points, as well as the different phases of the system, relies on the positional and the orientational order parameters and their spatial correlation functions, and are discussed in the subsequent sections.

2.3.2 Static Structure Function and Solid Order Parameter

The order parameter of the solid-hexatic melting is average of the structure factor at the four Bragg peaks in the reciprocal lattice plane. The structure factor (SSF) is the Fourier transform of the density correlation and can clearly distinguish between a solid, a hexatic and a liquid phase. For a liquid phase, the ensemble averaged density $\langle \rho(\mathbf{r}) \rangle$ neither depends on the magnitude nor on the direction of $\mathbf{r}$. This projects the complete translational and rotational symmetry of the liquid phase. In the crystalline solid phase, $\langle \rho(\mathbf{r}) \rangle$ becomes a periodic function of $\mathbf{r}$, and refers to the broken symmetries associated with this phase.

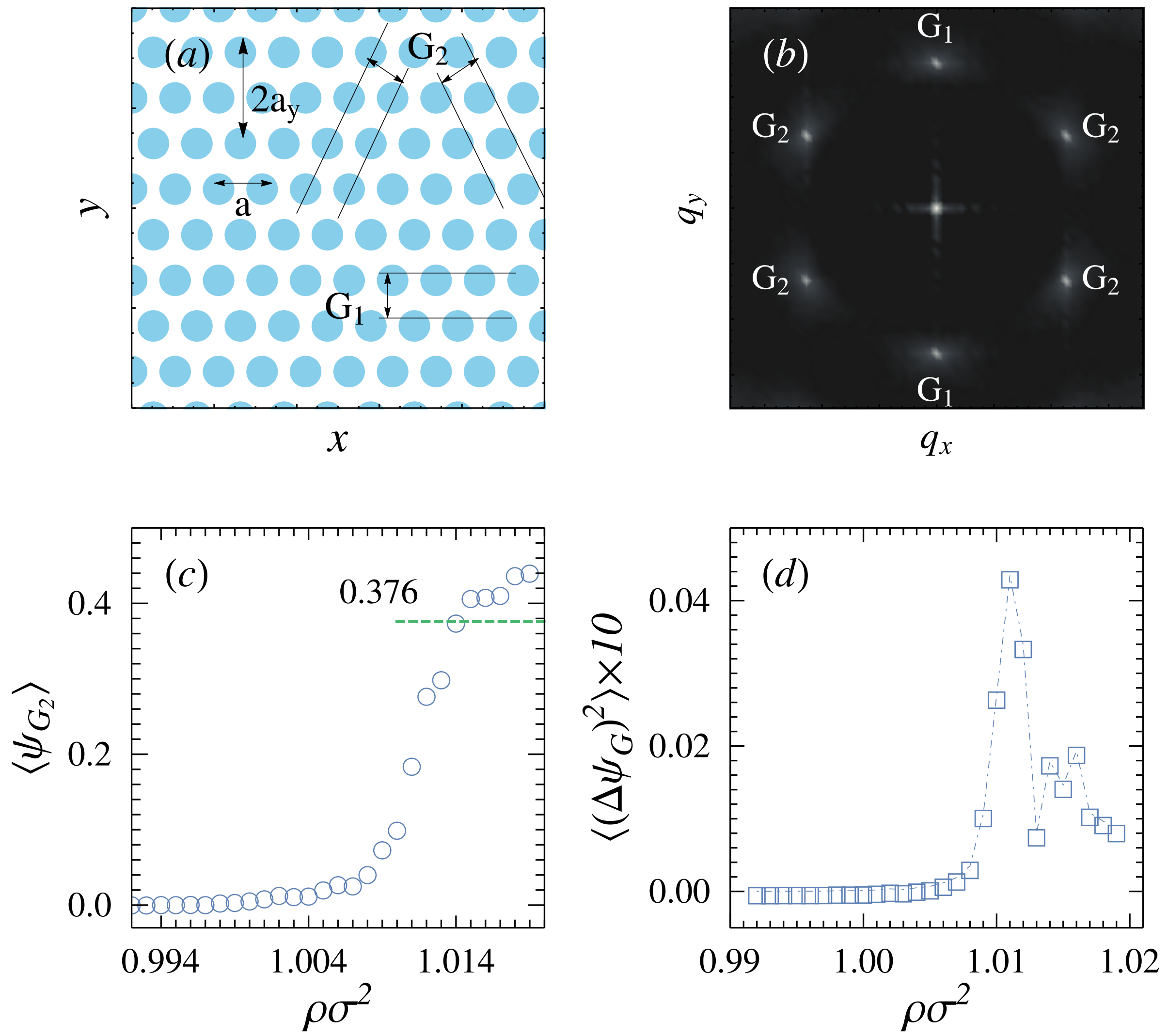

Figure 2.2 In Figure (a): schematic representation of two dimensional triangular lattice. The lattice spacing and corresponding reciprocal lattice vectors are indicated on top of it. Figure (b): **SSF plane**: six intensity peaks at corresponding reciprocal lattice vectors for triangular crystalline structure. Figure (c): The calculated time-averaged solid order parameter $\langle \psi_{G_2} \rangle$ as a function of system density $\rho\sigma^2$. The cut at 0.376 indicates the hexatic-solid transition point. Figure (d): Fluctuation of solid order parameter as a function of system density.

The Fourier transform of the local density translates to $\rho_{\mathbf{q}} = \sum_{j=1}^{N} e^{-\mathrm{i}\mathbf{q}\cdot\mathbf{r}_j}$ with $\rho_{\mathbf{q}}^* = \rho_{-\mathbf{q}}$ which ensures $\langle \psi_{\mathbf{q}} \rangle$ is real. The SSF is then constructed from $\rho_{\mathbf{q}}$ via the relation

$$\langle \psi_{\mathbf{q}} \rangle = (1/N)\ \langle \rho_{\mathbf{q}}\ \rho_{-\mathbf{q}} \rangle \tag{2.5}$$

In the top figure of Fig. 2.2 (a), a perfect triangular lattice is shown with lattice spacing a and a_y in x and y direction, respectively. For such a periodic geometry we obtain six intensity peaks in the reciprocal lattice plane (see Fig. 2.2(b)) corresponding to the following six reciprocal lattice vectors $\mathbf{G}_1 = (0, \pm 2\pi/a_y)$ and $\mathbf{G}_2 = (\pm 2\pi/a, \pm \pi/a_y)$

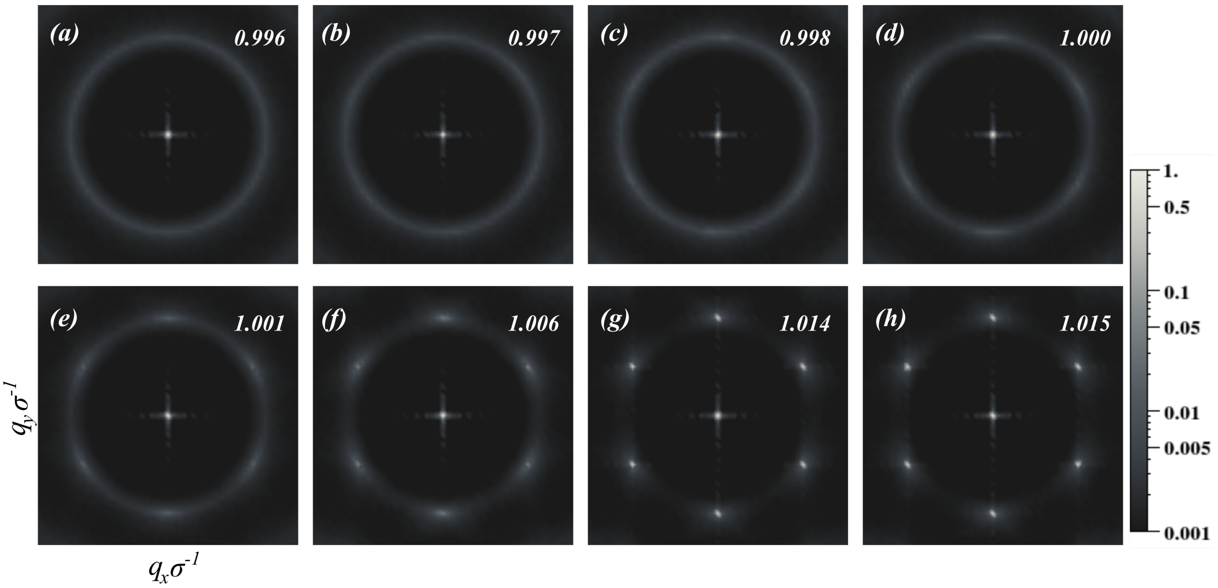

Figure 2.3 The static structure factor for different densities of the system as indicated in the legend. $\psi_{\mathbf{q}}$ is calculated in the Fourier plane with resolution interval of $0.01\sigma^{-1}$.The sequence depicts the melting of the solid to a hexatic and the melting of the hexatic to an isotropic liquid phase.Plot of SSF

The average value of SSF with respect to vectors $\mathbf{G}_1$ can only be used to identify density modulation in the system. In the solid phase, in addition to the peaks at $\mathbf{G}_1$, four additional peaks at the reciprocal vectors $\mathbf{G}_2$ are observed in the structure factor (see Fig. 2.2 (b)). Consequently, the average value of these four intensity peaks, $\langle\psi_{G_2}\rangle$, serve as the solid order parameter. In Fig. 2.2 (c) and (d) time-averaged value of solid order parameter $\langle\psi_{G_2}\rangle$ and its fluctuations are shown as function of the density of the system. The solid order parameter shows a monotonic increase in its value as the density of the system is increased. Of more interest are the fluctuations of the solid order parameter $\langle\Delta\psi^2_{\mathbf{G}_2}\rangle$ as a function of density. The location of the maximum of $\langle\Delta\psi^2_{\mathbf{G}_2}\rangle$ gives us an estimate of the solid melting point. From Fig. 2.2 (d) we see that this happens at the density $\rho\sigma^2 \approx 1.011$, in close agreement with the estimated value from the pressure-density curve.

A sequence of plots of the SSF that follows the phase transition in the system are shown in Fig. 2.3. The SSF can very clearly distinguish amongst a solid, a hexatic and a liquid phase.[32] In the solid phase the six intensity peaks are reflective of the six-fold symmetry of the solid (see Fig. 2.3 (g)-(h). In the hexatic phase, the six intensity peaks broadens on a circle of radius $2\pi/a$ shown in Fig. 2.3 (c)-(f). In the liquid phase, the isotropy of the system results in a characteristic circular ring in the SSF (see 2.3 (a) and (b)).

2.3.3 Pair-correlation Function and Identification of Solid-Melting Point

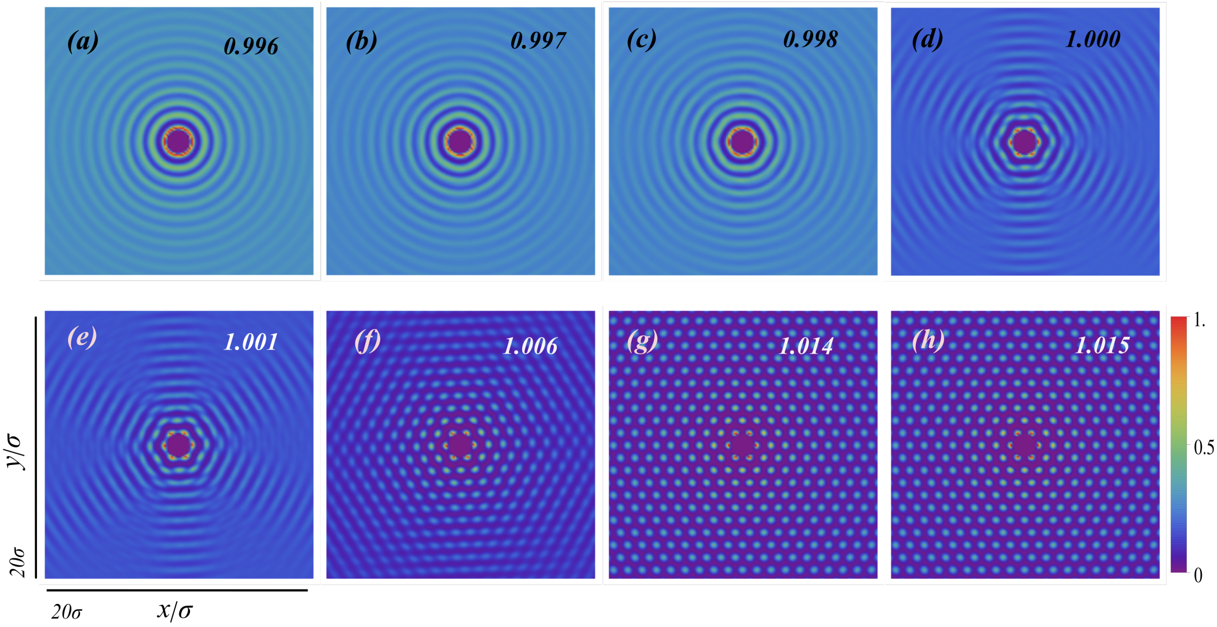

Figure 2.4 Time-averaged pair-correlation function g(x,y) is shown for the densities indicated on top of each plot. For clear visibility it is shown in the length scale of $20\sigma\times$ 20σ. The calculations are done by aligning Δx in the direction of system orientation. Plot corresponding to the density $\rho\sigma^2$=1.014 belongs to the solid and for $\rho\sigma^2$=0.996 to the isotropic liquid phase.

While both the pressure-density curve and the static structure factor bears the signature of the two-step melting process in the system, the descriptions are qualitative and a precise identification of the melting points can not be made from these information. Further, it also does not provide any information on the nature of the transitions. To resolve the positional order even at the largest length scale in the system, we turn our attention to the pair-correlation function that gives us a qualitative as well as a quantitative estimate of the melting points. The pair-correlation function $g(x,y) = \langle\rho(x,y)\rho(0,0)\rangle/\langle\rho^2\rangle$ gives the information about the positional order in the system. To determine $g(x,y)$, we divided the system in a 4096×4096 grid and measured the pair-correlation function by counting the number of particles at the separation $\mathbf{r}$ from a chosen particle, normalized by the number that would be in an ideal gas system for the same density. The subsequent histograms for a given density was averaged over 200 independent configurations. Care was taken to orient each configuration of the system along the direction of the corresponding global orientation.

In Fig. 2.4, a sequence of plots of the pair correlation function are shown that follows the phase transition in the system. For a clear visibiility of the different structures, we restrict the plots over an area of $20\sigma\times20\sigma$. At very high densities we observe a triangular structure characteristic of the solid phase (see Fig. 2.4 (f)-(h)). The lowest density at which such triangular structure is distinctly visible happens at the density $\rho\sigma^2 = 1.012$ (not shown in the figure), which gives us a qualitative estimate of the solid-hexatic melting point. As the density of the system is decreased below this, the sharp triangular structure is replaced by diffused intensity peaks that overlap with concentric hexagonal rings. This is the signature of the hexatic phase. On further decreasing the density, the diffused intensity peaks in $g(x,y)$ starts fading and instead we observe distinct hexagonal rings. In the liquid phase, the hexagonal rings are replaced by concentric circular rings, characteristic of the isotropic liquid phase.

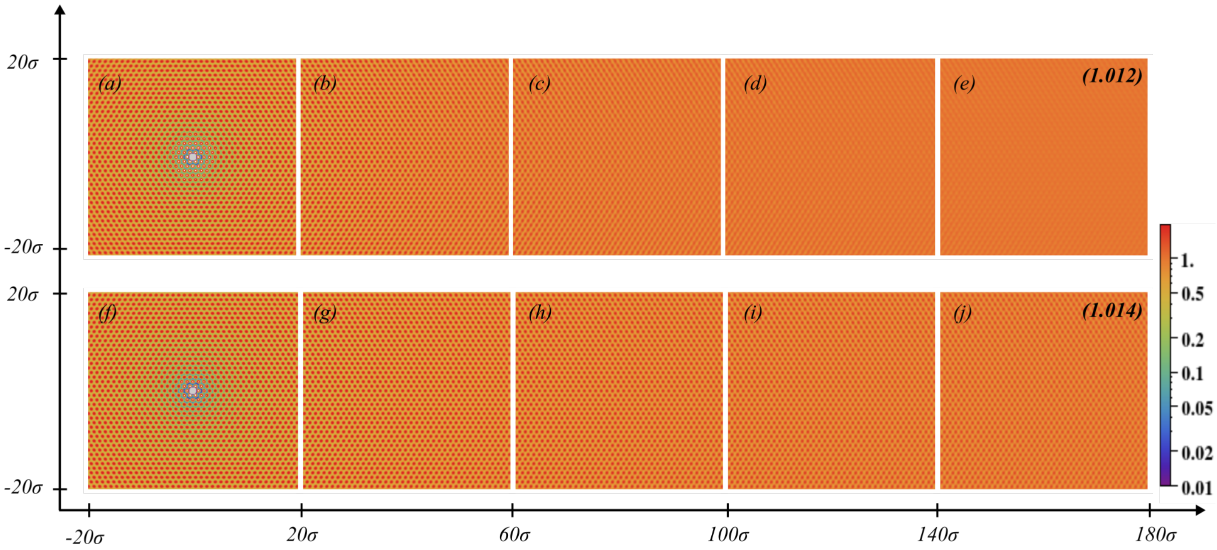

Figure 2.5 Scan of pair-correlation g(x,y) along x-axis with the window of $40\sigma \times 40\sigma$ for densities $\rho\sigma^2 = 1.012$ (upper panel) and 1.014 (lower panel). At $\rho\sigma^2 = 1.014$ periodic arrangement can be seen throughout the range. whereas it disappears at large distances for $\rho\sigma^2 = 1.012$.

A system wide scan of the pair-correlation function shown in Fig. 2.5 (a)-(j) for two densities $\rho\sigma^2 = 1.012$ (Fig. 2.5 (a)-(e)) and 1.014 (Fig. 2.5 (f)-(j)) that lies close to the phase transition point. The scan clearly shows that at the density $\rho\sigma^2 = 1.012$ the triangular structure persists only up to 60σ and at larger separations, the structures are more diffused. In contrast, at the density $\rho\sigma^2 = 1.014$, the positional order is maintained almost throughout the system size. To quantify this, we look at the cut of the pair-correlation function $g(x,0) - 1$, and a quantitative estimate of the solid-hexatic melting point is obtained from this cut of the pair-correlation function.[25,26] In the solid phase, a quasi-long range positional order is predicted by the KTHNY theory. Exactly at the transition point, the positional correlation decays algebraically with an exponent $\eta^* = 1/3$. From the measured pair-correlation function shown in Fig. 2.6, we also observe a similar behavior that conforms to the KTHNY scenario of melting. The cut of the pair-correlation function $g(x,0) - 1$ shows a quasi-long range order, decaying algebraically with an exponent $\eta \leq 1/3$, that transforms into an exponential decay as the system goes

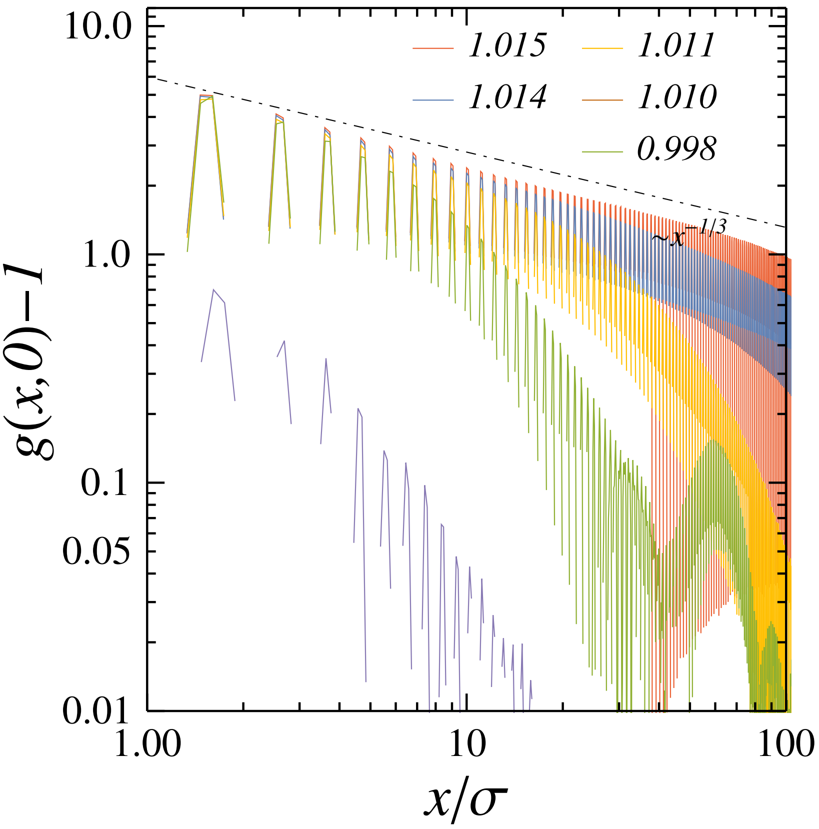

Figure 2.6 A cut taken along **r** $= (x, 0)$ from the two dimensional pair-correlation function g(x,y) is shown for various densities. The densities belonging to the different colors are indicated inside the plot. At $\rho\sigma^2$ =1.014 the function g(x,0)-1 shows power law decay. The black dashed line with the decaying slope of 1/3 inside the plot is to compare the stability criteria for solids as predicted in KTHNY theory. For lower densities the decaying function shifts its behaviour from algebraic to the exponential form.

into a hexatic phase. While in principle, following the cut of the pair-correlation as the density of the system is varied, would yield the solid melting point, there are few pitfalls associated with this. To illustrate this, we choose the densities $\rho\sigma^2 = 1.014$ and 1.015 in Fig. 2.6. In the both the cases, $g(x,0)-1$ exhibits a faster asymptotic decay compared to $x^{-1/3}$. One reason for this is that the lattice plane corresponding to $\Delta y = 0$ does not align with the one of the six lattice planes for a solid. Consequently, one observes a faster decay of the correlation.

The correlation of the order parameter $g_{\mathbf{G}}(r) = \langle \psi_{\mathbf{G}_2}(\mathbf{r}' + \mathbf{r})\psi_{\mathbf{G}_2}(\mathbf{r}')\rangle$ does a better job in identifying the melting point. The plots of $g_{\mathbf{G}(r)}$ for different densities is shown in Fig. 2.7 for different densities close to the melting of the solid. An algebraic decay with an exponent $\eta = 1/3$ is obtained for the density $\rho\sigma^2 = 1.014$, and below this the correlation transforms to a short-ranged exponential form.

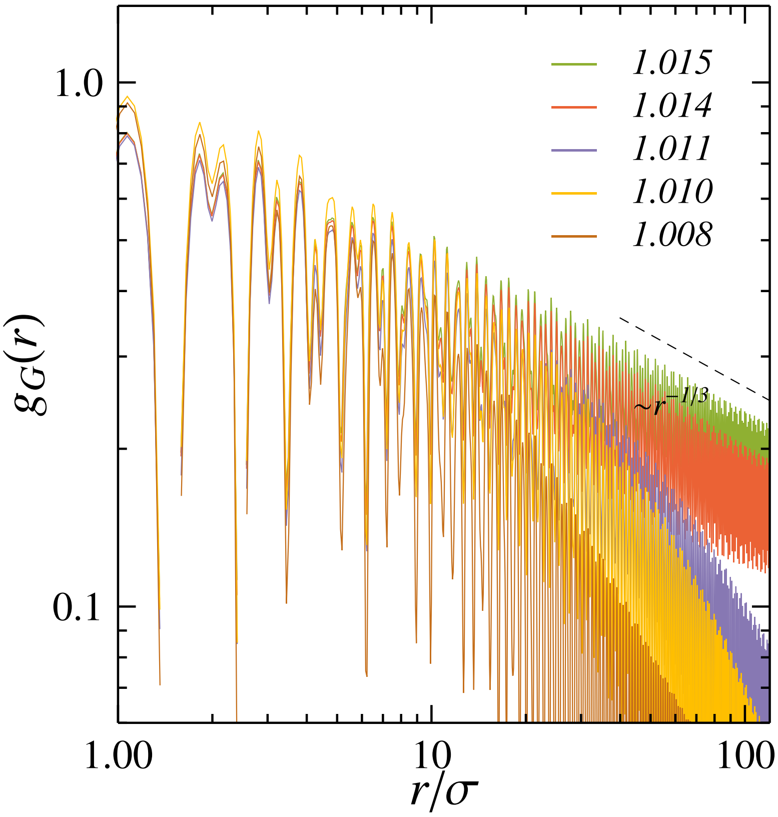

Figure 2.7 Plot of the spatial correlation of the solid order parameter for different densities as indicated in the legend. A stable solid is determined from the decay of the correlation function. KTHNY theory predicts an algebraic decay with an exponent $\eta \leq 1/3$, where the equality denotes the boundary of the stable solid phase and is indicated by the dashed line in the figure. The lowest density at which we observe a decay of the form $r^{-1/3}$ corresponds to the density $\rho\sigma^2 = 1.014$. Below this density, the decay transforms from an algebraic to an exponential form.

The final confirmation comes from the finite size scaling of the solid order parameter. The solid order parameter, defined as the correlation of the density modes, is evaluated in sub-boxes of size $\ell_x = L_x/N$ and $\ell_y = L_y/N$, such that $\ell_x \times \ell_y = \ell^2$. To study the finite-size scaling, we looked at the ratio of the solid order parameter in these sub-boxes to the global solid order parameter: $\langle \psi_{\mathbf{G}_2}(\ell)\rangle / \langle \psi_{\mathbf{G}_2}(L)\rangle$. KTHNY theory predicts that the ratio should exhibit a power-law decay :$\langle \psi_{\mathbf{G}_2}(\ell)\rangle / \langle \psi_{\mathbf{G}_2}(L)\rangle \sim (\ell/L)^{-\nu}$ with $\nu \leq 1/3$. The equality once again determines the boundary of the solid phase. In Fig. 2.8 we show the finite size scaling of the solid order parameter. The lowest density at which a stable solid exists throughout the system happens at $\rho\sigma^2 = 1.014$. Below this density the ratio of the local to the global solid order parameter does not show an algebraic decay, and instead has the signature of short-range positional order. Thus, we find the solid-hexatic melting to occur at the density of $\rho\sigma^2 = 1.014$ in close agreement with finding of Kapfer *et. al.*[26]

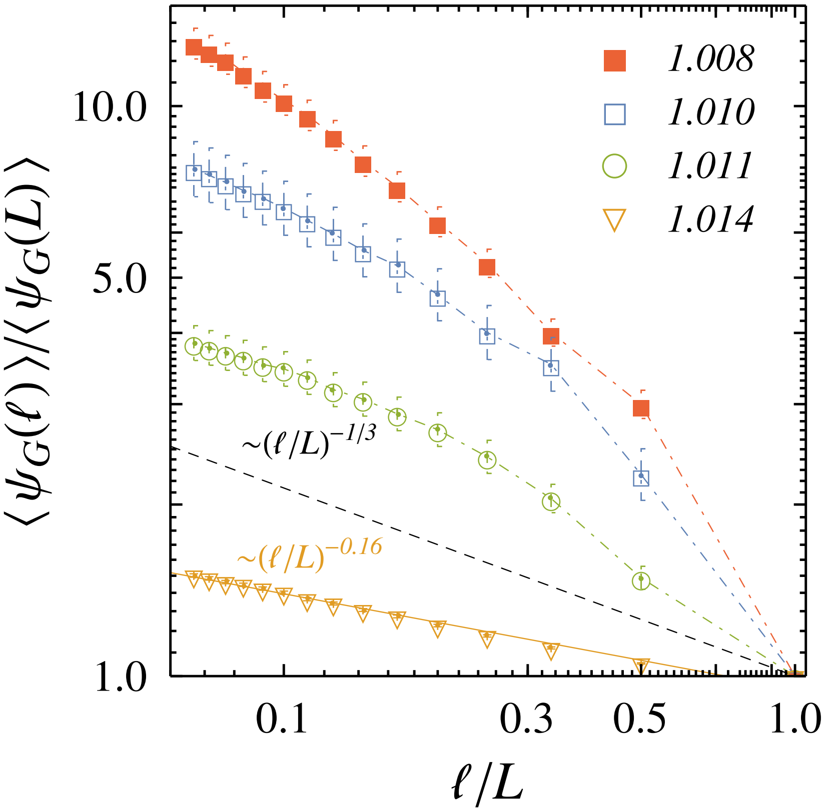

Figure 2.8 Finite size scaling of the solid order parameter for different densities as indicated in the legend. To study the finite size scaling, the system was divided in sub-boxes of size $\ell_x \times \ell_y = \ell^2$, and the solid order parameter was determined using the definition $\langle\psi_{\mathbf{G}_2}\rangle = \langle\rho_{\mathbf{q}}\rho_{-\mathbf{q}}\rangle$ but restricted to these sub-boxes. In the KTHNY theory, the ratio of the local to the global solid order parameter decays as a power law: $\langle\psi_{\mathbf{G}_2}(\ell)\rangle/\langle\psi_{\mathbf{G}_2}(L)\rangle \sim (\ell/L)^{-\nu}$, with $\nu \leq 1/3$. The equality marks the boundary of the stable solid phase, indicated by the dashed line in the figure. The solid melting occurs at the density of $\rho\sigma^2 = 1.014$. As the density is decreased beyond this value, the decay is no longer algebraic and bears the signature of short range positional order in the system.

2.3.4 Orientational Order and Hexatic Melting

In the solid phase due to the periodic arrangement particles, the bond angle between neighboring particles shows long range correlation. A two-dimensional solid is therefore characterized by a quasi-long range positional order and long-range orientational order. Once the solid melts, the new phase is not isotropic and retains some orientational ordering. This is the hexatic phase, characterized by a quasi-long range orientational order. As the hexatic melts to an isotropic liquid, the orientational order becomes short-ranged.

The qualitative picture of the melting of the hexatic phase comes from the pair-correlation function shown in Fig. 2.4 (a)-(e). In the density regime $1.001 \leq \rho\sigma^2 \leq$

1.011, $g(x,y)$ shows the hexagonal rings that is characteristic of the hexatic phase. Isotropic circular rings indicating a liquid phase is obtained at densities below $\rho\sigma^2 \approx 0.996$. In the intermediate density regime of $1.001 < \rho\sigma^2 < 0.96$ the concentric rings are not perfectly circular, suggesting that the transition happens via a weak first order.

To be more precise, we use the orientational order parameter and its correlation to identify the hexatic and liquid phase. The global bond orientational order parameter is defined using a measure for the local orientational order ψ_6^i:

$$\psi_6^i = \frac{1}{n}\sum_{k=1}^{n} e^{\mathbb{i}6\theta_{ik}} \tag{2.6}$$

Here n is the number of topological neighbors of i^{th} particle, identified using Voronoi tessellation (see figure Fig. 2.9). The angle θ_{ik} is the angle made by the separation vector $\mathbf{r}_{ik}$ with x-axis. With this definition, the corresponding global orientational order parameter for the system is defined as

$$\langle\psi_6\rangle = \left\langle \left| \frac{1}{N}\sum_{i=1}^{N} \psi_6^i \right|^2 \right\rangle \tag{2.7}$$

The variation of orientational order parameter $\langle\psi_6\rangle$ and its fluctuations are plotted against the system density in Fig. 2.10. In the liquid phase its value is around zero and it increases as the density goes higher. In the hexatic phase the non-zero value of $\langle\psi_6\rangle$ indicates that the orientational order is not completely broken in this phase. Irrespective of the order of the transition, the fluctuations of the order parameter peaks around the transition point. This gives us with an estimate of the hexatic-liquid transition at $\rho\sigma^2 \approx 0.998$. We note that this estimate is only an approximate, since it is derived from the fluctuations of the order parameter that in itself is averaged over the whole system. A better quantification is achieved through the spatial correlation and the finite size scaling of the orientational order parameter, since both of these resolves the orientational order at different length scales of the system.

The spatial correlation of the bond orientational order parameter $g_6(r)$ is defined using the local orientational order ψ_6^i as

$$g_6(r) = \langle(\psi_6^i)^*(\psi_6^j)\delta(\mathbf{r}-\mathbf{r}_{ij})\rangle, \tag{2.8}$$

where $\mathbf{r}_{ij} = \mathbf{r}_i - \mathbf{r}_j$ is the separation vector between two particles. In Fig. 2.11 this correlation function $g_6(r)$ is shown for various densities. In the solid phase the correlation

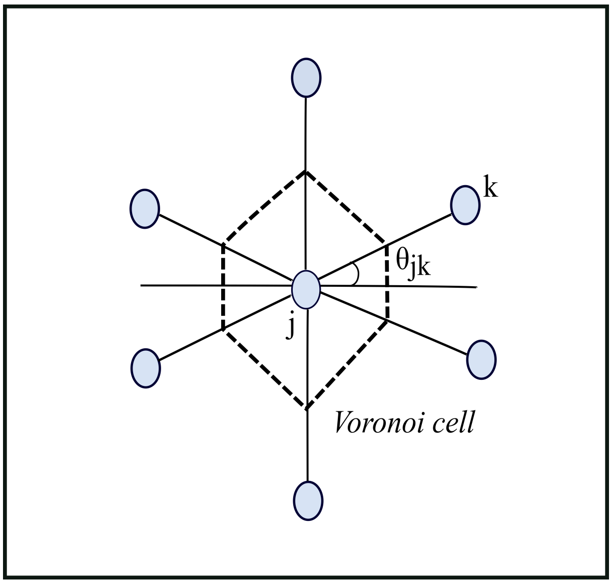

Figure 2.9 A partcle having six topological neighbors is presented in figure (a). The neighbors are calculated by identifying Voronoi cell for each of the particles. First for a given particle 'j', we select candidates within a cut-off radius. Next we find the bond length r_{jk} between j^{th} particle and these candidates. Then perpendicular bisectors for each of the bond length is calculated. The points where these bisectors meet, form the vertices of the Voronoi cell for the j^{th} particle. Partcles which share at at least one of edges of Voronoi cell are considered as topological neighbors.

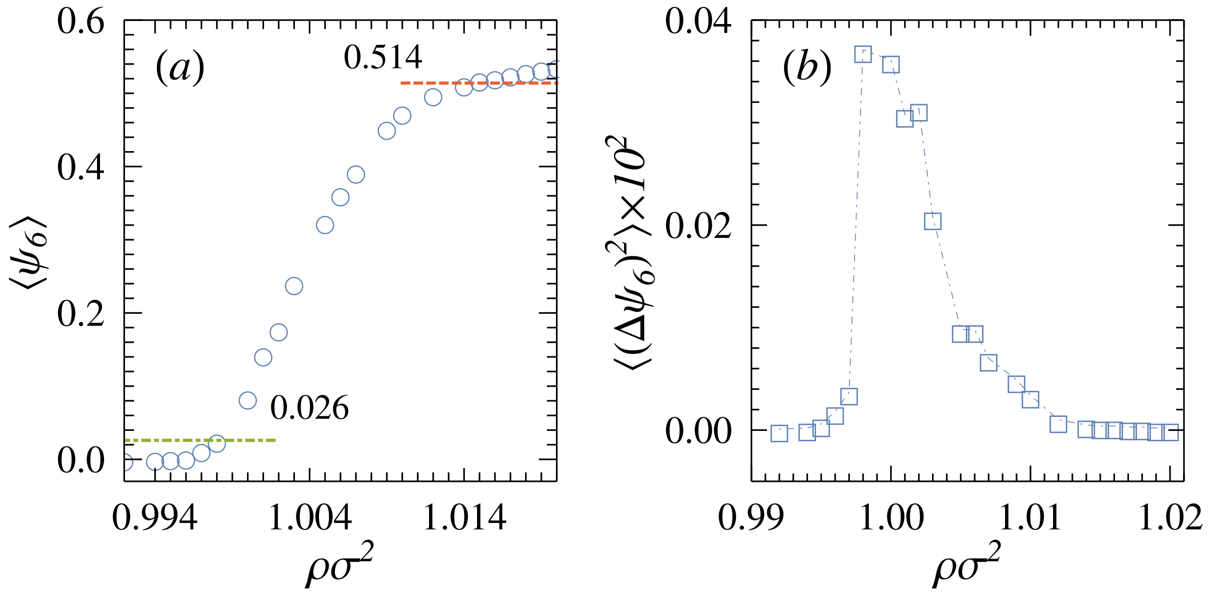

Figure 2.10 Plots of the time-averaged orientational order parameter $\langle\psi_6\rangle$ (figure (a)) and its fluctuations $\langle\Delta\psi_6^2\rangle$ (figure (b)) as a function of system density $\sigma^2\rho$. The cuts at the values 0.06 and 0.514 in figure (a) represent the liquid to hexatic and hexatic to solid transition points respectively. The maximum of the fluctuations occur at the density $\rho\sigma^2 \approx 0.998$, indicating the hexatic-liquid transition point.

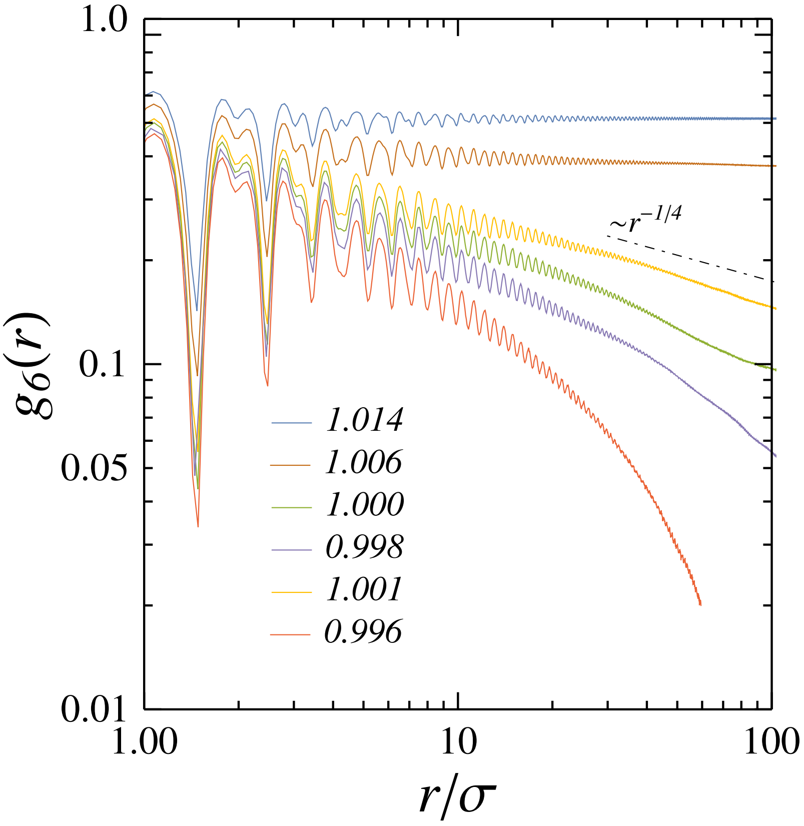

Figure 2.11 Spatial correlation of bond angle orientations $g_6(r)$ is shown for the densities indicated in the legends. The black dot-dashed line is the plot of $r^{-1/4}$ that marks the upper bound for the stable hexatic according to the prediction of KTHNY theory. The lowest density at which a stable hexatic phase is obtained is that of $\rho\sigma^2 = 1.001$. A pure exponential decay of the correlation function throughout the system, characteristic of the isotropic liquid phase, is obtained at densities below $\rho\sigma^2 = 0.996$. In the intermediate density regime, the correlation shows an exponential decay up to 50σ and crosses over to an algebraic decay with an exponent greater than $1/4$.

remains long ranged even at the largest distance of the system size as can be seen for the density $\rho\sigma^2 = 1.014$. As the density is decreased, the long range orientational order transforms to a quasi-long range order, in agreement with KTHNY theory. The exponent of the algebraic decay $\eta_6 \leq \eta_6^*$, where $\eta_6^* = 1/4$ is the upper bound for a stable hexatic phase in the KTHNY theory. Thus, at the hexatic-liquid transition point, the orientational correlation function decays with an exponent η_6^* and this happens at the density $\rho\sigma^2 \approx 1.001$. However, as is evident from the pair correlation function $g(x,y)$ shown in Fig. 2.4, the system does not immediately go into an isotropic liquid phase. This signature is also observed in $g_6(r)$. In the density regime of $0.996 < \rho\sigma^2 < 1.001$, the orientational correlation shows an exponential decay up to 50σ, beyond which it exhibits a power law decay with an exponent which is larger than η_6^*. A perfect exponential decay is only obtained for $\rho\sigma^2 \leq 0.996$. Hence, we identify $\rho\sigma^2 \approx 1.001$ as the boundary of the stable hexatic phase.

The final evidence comes from the finite size scaling of the bond-orientational order parameter. To this end, we divide the system in M blocks along each direction so that the size of each block is $\ell_x \times \ell_y = \ell^2 = L_x L_y / M^2$. The orientational order parameter $\psi_6(\ell)$ is calculated from Eq. (2.7), restricting the sum over the blocks. The ratio of the $\psi_6(\ell)$ to $\psi_6(L)$ is then computed for different values of M. The KTHNY theory predicts an algebraic decay of $\psi_6(\ell)/\psi_6(L)$, that is $\psi_6(\ell)/\psi_6(L) \sim (\ell/L)^{-\nu}$ with $\nu \leq 1/4$. The equality once again marks the boundary of the stable hexatic phase. In Fig. 4.12 we show our finite size scaling analysis for the orientational order parameter. From the decay of the scaling ratio $\psi_6(\ell)/\psi_6(L)$, a stable hexatic phase is obtained in the density regime $1.014 < \rho\sigma^2 \leq 1.001$. Below this density, decay of $\psi_6(\ell)/\psi_6(L)$ is faster than $(\ell/L)^{-1/4}$ indicating that the hexatic phase becomes unstable. Thus, we identify $\rho\sigma^2 \approx 1.001$ as the boundary of the stable solid. The fact that beyond this density, the transition to the liquid phase proceeds via a first order transition is also consistent with the earlier findings of Kapfer *et. al*[26], albeit they find the stable hexatic boundary at the density $\rho\sigma^2 = 1.005$.

2.4 Order of the transition

We now focus on the order of the transitions. The identification of the two transitions are done using the distribution of the local translational and positional order parameter. In the first step, we characterize the nature of the solid-hexatic transition. For this, we divide the system in sub-boxes of size $L_x/10 \times L_y/10$ and the solid order parameter was determined the from the density mode $\rho_{\mathbf{G}_2}$, with the sum over particle index in $\rho_{\mathbf{G}_2}$ restricted over the sub-boxes. The distribution of the solid order parameter is presented in Fig. 2.13. The distribution $\mathscr{P}(\psi^{\ell}_{\mathbf{G}_2})$ of the local solid order parameter $\psi^{\ell}_{\mathbf{G}_2}$ is uni-modal in the solid and the liquid phase, as illustrated in Fig. 2.13 at the densities which are the melting boundaries of the solid ($\rho\sigma^2 = 1.014$) and the liquid phase ($\rho\sigma^2 = 0.996$). In the solid phase, the maximum of the distribution occurs at a high value of the local solid order parameter. With the melting of the solid, the distribution starts to broaden, until it becomes uni-modal again in the liquid phase with a maximum at low value of the local solid order parameter. The absence of metastable states during the transition leads us to the conclusion that the melting of a solid to a hexatic phase is a continuous transition, in agreement with the KTHNY theory.

In the case of the hexatic– liquid melting, a little care needs to be taken in following a similar procedure to determine the local bond-orientational order parameter ψ^{ℓ}_6. If

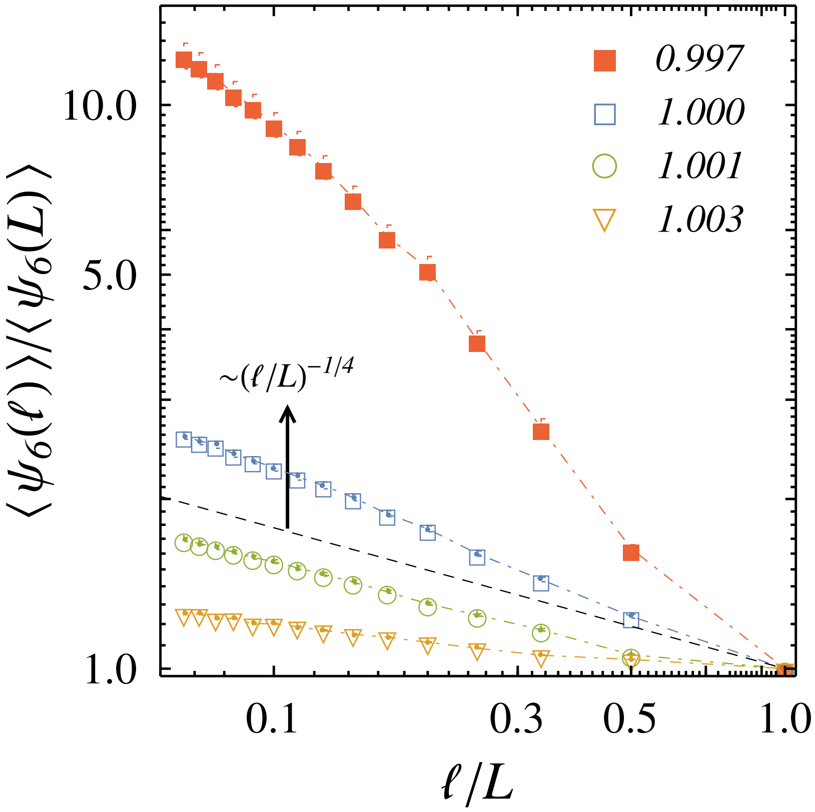

Figure 2.12 Finite size scaling of the orientational order parameter for different densities as indicated in the legend. The system was divided into blocks of size $\ell_x \times \ell_y = \ell^2$ and the orientational order parameter was calculated using Eq. (2.7), restricting the sum in the block. KTHNY theory predicts the ratio $\psi_6(\ell)/\psi_6(L)$ to scale as $(\ell/L)^{-\eta_6(\rho)}$, with $\eta_6(\rho) \leq 1/4$. The equality marks the boundary of the stable hexatic phase and is indicated by the black dashed line. The dot-dashed lines passing through the symbols are guide to the eye. A stable hexatic phase is obtained up to the density $\rho\sigma^2 \approx 1.001$. Below this density, the finite size scaling shows the signature of short-range orientational order.

there exists a coexistence, the size of coexisting region needs to be identified first. To achieve this, we divide the whole system in 16×16 blocks and determine the local orientational order parameter is these blocks.In Fig. 2.14, we plot a heatmap of this spatially resolved $|\psi_6(\mathbf{r})|^2$ and overlap it with the vector that represents the local orientation $(\mathrm{Re}\,\psi_6(\mathbf{r}), \mathrm{Im}\,\psi_6(\mathbf{r}))$.In the solid phase, represented by the melting boundary of the solid in Fig. 2.14 (d), we observe a uniform hexatic order in the system. In contrast, in the hexatic phase for densities below the stable hexatic boundary ($\rho\sigma^2 < 1.001$), we find patches of coexisting regions of high and low hexatic order (see Fig. 2.14 (b) and (c)). The size of the coexisting regions are dependent on the density and decreases as the liquid melting point is approached. This gives us a fairly good idea of the size of coexisting regions and make a decision on the block size in which local orientational order is determined. Additionally, to ascertain a macrophase separation over time, we followed similar configurations over time, as shown in Fig. 3.15 for the density $\rho\sigma^2 = 0.998$. The

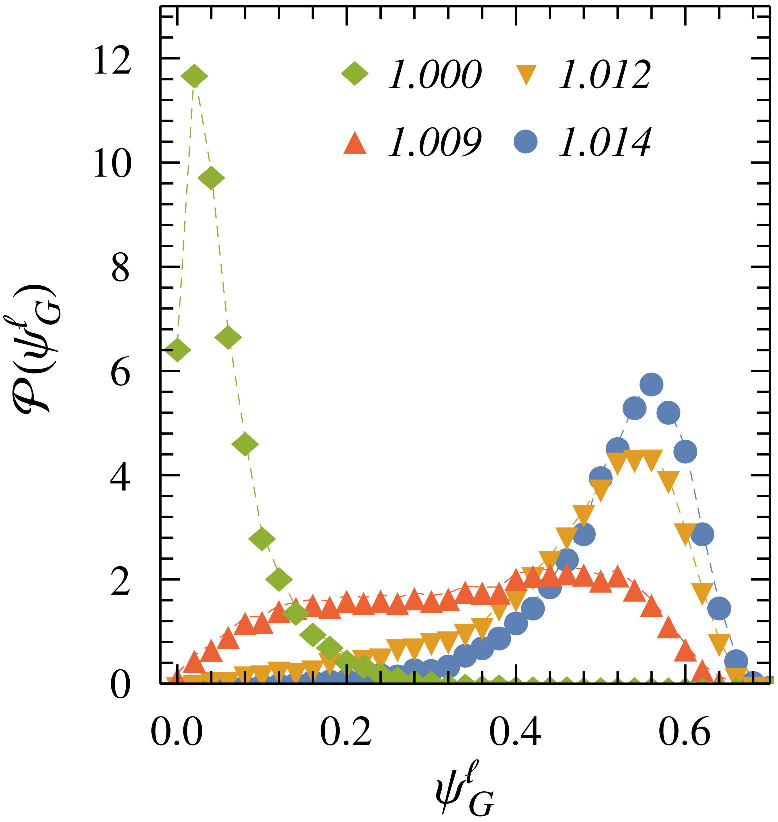

Figure 2.13 Distribution of local solid order parameter for the densities as indicated in the legend. The whole system was divided into 100×100 boxes and the local solid order parameter was calculated by computing the density mode $\rho_{\mathbf{G}_2}$, restricted to these sub-boxes. The distribution is uni-modal both in solid ($\rho\sigma^2 = 1.014$) and in liquid phase ($\rho\sigma^2 = 0.996$). With the melting of the solid to a hexatic phase, the distribution broadens, but there is clear absence of bi-modality in the distribution. This indicates that the transition is continuous.

plots clearly reveal that a macrophase separation indeed exists over time.

Accordingly, we divide the system into 100×100 blocks and estimate the local orientational order in these blocks. The measured distribution of $\mathscr{P}(\psi_6^{\ell})$ is shown Fig. 2.16. In the solid phase, the distribution has a single maximum at a high value of ψ_6^{ℓ} (not shown in the figure). As the solid melts to a hexatic, the distribution retains the uni-modal feature, but develops a fat tail with finite probabilities for lower values of hexatic order. At the boundary of the stable hexatic, we see the start of a weak bi-modality in the distribution with almost equal peak weights at the density $\rho\sigma^2 = 1.000$. Very close to the liquid melting point ($\rho\sigma^2 = 0.997$), the signature of a intermediate metastable state is evident. From this we conclude that the hexatic-liquid melting proceeds via weak first order transition, in agreement with the findings of Kapfer *et. al.*.[26] We summarise the melting points and compare it with the earlier work of Kapfer *et. al.* in the table below.

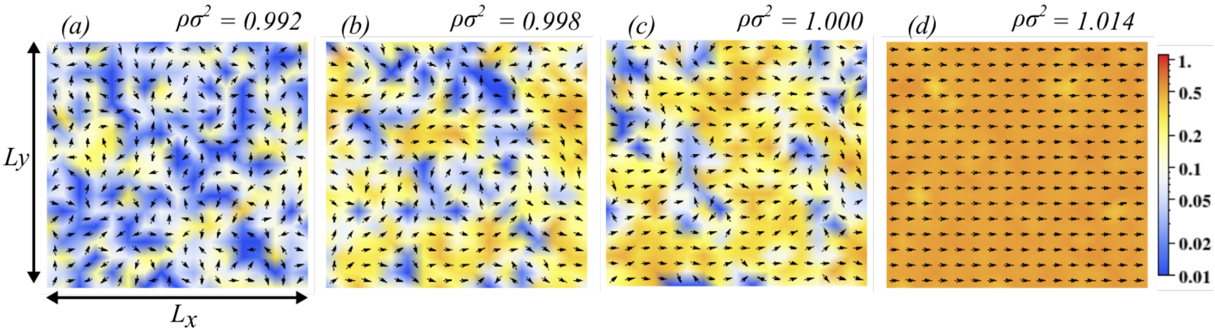

Figure 2.14 Coarse-grained plots of the orientational order parameter in the system for different densities as indicated on the top. The heatmap was obtained by dividing the whole system into 16×16 blocks.The local orientational order $\psi_6(\mathbf{r})$ is calculated inside each block using the particle based definition ψ_6^i and restricting the sum in Eq. (2.7) over the sub-boxes. Overlapped on the heatmap are the local orientation vectors $(\text{Re } \psi_6(\mathbf{r}), \text{Im } \psi_6(\mathbf{r}))$ indicated by the arrows. Below the stable hexatic boundary ($\rho\sigma^2 < 1.001$), the system shows patches of coexisting regions of high and low hexatic order.

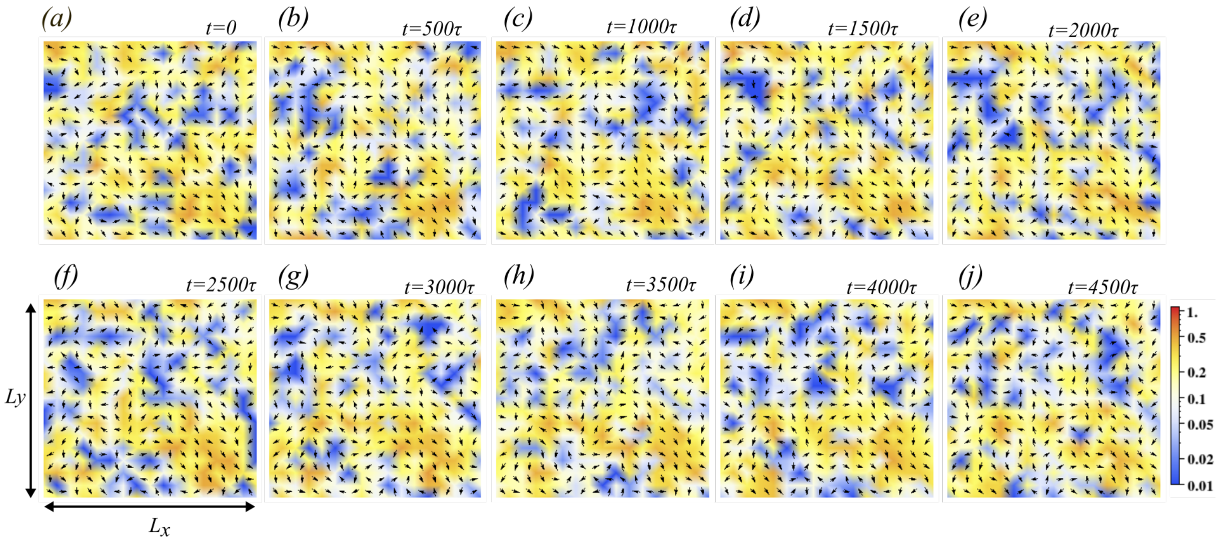

Figure 2.15 Time evolution of coarse-gained orientational order at the density $\rho\sigma^2 = 0.998$. The heatmap at each time snapshot was obtained by dividing the whole system into 16×16 blocks.The local orientational order $\psi_6(\mathbf{r})$ is calculated inside each block using the particle based definition ψ_6^i and restricting the sum in Eq. (2.7) over the sub-boxes. Overlapped on the heatmap are the local orientation vectors $(\text{Re } \psi_6(\mathbf{r}), \text{Im } \psi_6(\mathbf{r}))$ indicated by the arrows. The time evolutions indicate a stable macrophase separation of high and low hexatic order.

2.5 Conclusion

In summary, we have studied the melting scenarios of a repulsively interacting monodispersed colloidal suspension in two-dimensions. The melting points and the different phases are identified using the translational and orientational order parameter, their spatial correlations and finite size scaling. The solid phase is characterized by a quasi-

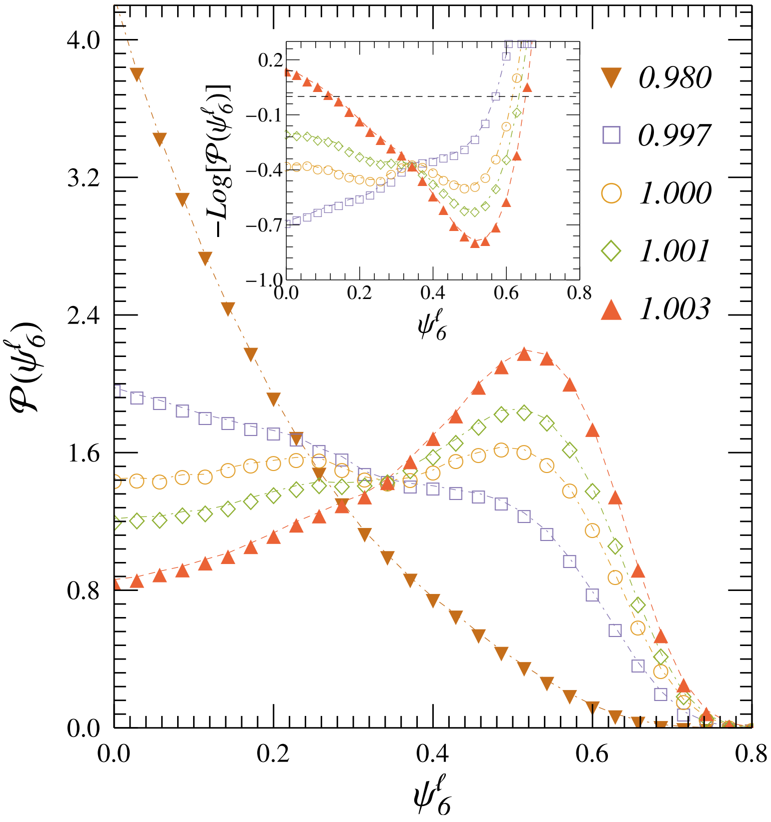

Figure 2.16 Distribution of local orientational order for the densities as indicated in the legend. The whole system was divided into 100×100 boxes and local order is calculated for a given configuration. A total of 200 independent configurations were used to construct the probability distribution $\mathscr{P}(\psi_6^\ell)$. As the solid melts to a hexatic, the distribution retains the uni-modal feature, but develops a fat tail with finite probabilities for lower values of hexatic order. At the boundary of the stable hexatic, we see the start of a weak bi-modality in the distribution with almost equal peaks at the density $\rho\sigma^2 = 1.000$. Very close to the liquid melting point ($\rho\sigma^2 = 0.997$), the signature of a intermediate metastable state is evident.

long range positional order and long range orientational order. On the other hand, the hexatic phase has a short range positional order and quasi-long range orientational order. The liquid phase, due to its isotropy, has both short range positional and orientational order. We find that the melting from a solid to a liquid is a two-step process. The solid melts to a hexatic phase via a continuous transition, in agreement with the KTHNY scenario. The melting of the solid occurs at the density $\rho\sigma^2 \approx 1.014$, and is identified from the nature of the decay of the positional order and the finite size scaling of the solid order parameter. The continuous nature of the transition is determined from the behavior of the distribution of the local solid order parameter as the density of the system is varied. In contrast, the hexatic to liquid transition proceeds via weak first order transition. From the decay of the spatial correlation of the orientational order parameter, we find that a stable hexatic phase exists up to a density of $\rho\sigma^2 = 1.001$. Below

Transition Densities	Kapfer *et. al.*[26]	Current Work
ρ_{hs}	$\rho\sigma^2 = 1.015$	$\rho\sigma^2 \approx 1.014$
ρ_{hex}	$\rho\sigma^2 = 1.005$	$\rho\sigma^2 \approx 1.001$
ρ_{liq}	$\rho\sigma^2 = 0.998$	$\rho\sigma^2 \approx 0.997$
Nature of Solid-Hexatic Transition	Continuous	Continuous
Nature of Hexatic-Liquid Transition	First-Order	First-Order

Table 2.1 Table comparing the solid-hexatic and the hexatic-liquid melting points and the nature of transition with the earlier works of Kapfer *et. al.*.[26]

this density, there are coexisting regions of high and low orientational order in the system. A distribution of the local orientational order also reveals the existence metastable states below the stable hexatic boundary. The melting scenarios are in confirmation of the earlier work by Kapfer *et. al.*. A comparison of the transition points obtained in the current study with that of the earlier results has been presented in Table 3.1. There is very little difference in the two transition points between the earlier work and the current study and we note that such a difference can be a result of the choice of the cutoff of the potential. While the work of Kapfer *et. al.* considered a cutoff $r_c = 1.8\sigma$ for the potential, we chose a cutoff $r_c = 2\sigma$. The choice of a slightly larger cutoff does not change the nature of the transition.

Bibliography

[1] A. T. Skjeltorp, *Phys. Rev. Lett.*, 1983, **51**, 2306–2309.

[2] C. A. Murray and D. H. Van Winkle, *Phys. Rev. Lett.*, 1987, **58**, 1200–1203.

[3] Y. Tang, A. J. Armstrong, R. C. Mockler and W. J. O'Sullivan, *Phys. Rev. Lett.*, 1989, **62**, 2401–2404.

[4] A. J. Armstrong, R. C. Mockler and W. J. O'Sullivan, *Journal of Physics: Condensed Matter*, 1989, **1**, 1707–1730.

[5] C. A. Murray and R. A. Wenk, *Phys. Rev. Lett.*, 1989, **62**, 1643–1646.

[6] C. A. Murray, D. H. V. winkle and R. A. Wenk, *Phase Transitions*, 1990, **21**, 93–126.

[7] C. A. Murray, W. O. Sprenger and R. A. Wenk, *Phys. Rev. B*, 1990, **42**, 688–703.

[8] Y. Tang, A. J. Armstrong, R. C. Mockler and W. J. O'Sullivan, *Phase Transitions*, 1990, **21**, 75–92.

[9] W. V. Megen, P. N. Pusey and P. Bartlett, *Phase Transitions*, 1990, **21**, 207–227.

[10] C. A. Murray, in *Bond-Orientational Order in Condensed Matter Systems. Partially Ordered Systems.*, ed. K. J. Strandburg, Springer-Verlag, New York, NY, 1992, ch. 4, pp. 137–215.

[11] R. E. Kusner, J. A. Mann, J. Kerins and A. J. Dahm, *Phys. Rev. Lett.*, 1994, **73**, 3113–3116.

[12] R. E. Kusner, J. A. Mann and A. J. Dahm, *Phys. Rev. B*, 1995, **51**, 5746–5759.

[13] K. Zahn and G. Maret, *Phys. Rev. Lett.*, 2000, **85**, 3656–3659.

[14] H. H. von Grünberg, P. Keim, K. Zahn and G. Maret, *Phys. Rev. Lett.*, 2004, **93**, 255703.

[15] P. Keim, G. Maret and H. H. von Grünberg, *Phys. Rev. E*, 2007, **75**, 031402.

[16] P. Dillmann, G. Maret and P. Keim, *Journal of Physics: Condensed Matter*, 2008, **20**, 404216.

[17] L. Assoud, F. Ebert, P. Keim, R. Messina, G. Maret and H. Löwen, *Phys. Rev. Lett.*, 2009, **102**, 238301.

[18] W. K. Kegel, *Science*, 2000, **287**, 290–293.

[19] V. L. Berezinsky, *Sov.Phys.JETP*, 1970, **59**, 907–920.

[20] J. M. Kosterlitz and D. J. Thouless, *J. Phys. C*, 1973, **6**, 1181.

[21] B. I. Halperin and D. R. Nelson, *Phys. Rev. Lett.*, 1978, **41**, 121–124.

[22] D. R. Nelson and B. I. Halperin, *Phys. Rev. B*, 1979, **19**, 2457.

[23] A. P. Young, *Phys. Rev. B*, 1979, **19**, 1855.

[24] P. Bladon and D. Frenkel, *Phys. Rev. Lett.*, 1995, **74**, 2519–2522.

[25] E. P. Bernard and W. Krauth, *Phys. Rev. Lett.*, 2011, **107**, 155704.

[26] S. C. Kapfer and W. Krauth, *Physical Review Letters*, 2015, **114**, 035702–5.

[27] A. Hajibabaei and K. S. Kim, *Phys. Rev. E*, 2019, **99**, 022145.

[28] J. A. Anderson, J. Antonaglia, J. A. Millan, M. Engel and S. C. Glotzer, *Phys. Rev. X*, 2017, **7**, 021001.

[29] W. Qi and M. Dijkstra, *Soft Matter*, 2015, **11**, 2852–2856.

[30] J. F. Fernández, J. J. Alonso and J. Stankiewicz, *Phys. Rev. Lett.*, 1995, **75**, 3477–3480.

[31] W. Qi, A. P. Gantapara and M. Dijkstra, *Soft Matter*, 2014, **10**, 5449–5457.

[32] P. M. Chaikin and T. C. Lubensky, *Principles of Condensed Matter Physics*, Cambridge University Press, Cambridge, 2012.

3

Phase transition in a system of two dimensional colloids interacting via Week-Chandler-Anderson potential

---

In this chapter, we present a detailed numerical simulation study of a two dimensional system of particles interacting via the Weeks- Chandler- Anderson potential, the repulsive part of the Lennard- Jones potential. With reduction of density, the system shows a two- step melting: a continuous melting from solid to hexatic phase, followed by a a first order melting of hexatic to liquid. The solid- hexatic melting is consistent with the Kosterlitz-Thouless-Halperin-Nelson-Young (KTHNY) scenario and shows dislocation unbinding. The first order melting of hexatic to fluid phase, on the other hand, is dominated by formation of string of defects at the hexatic-fluid interfaces.

3.1 Introduction

In Chapter 2 we studied the equilibrium melting of a monodispersed repulsively interacting colloidal suspension in two dimensions. In this chapter, we investigate the melting transition in a two-dimensional colloidal suspension with a Weeks-Chandler-Anderson[1] (WCA) pair interaction. In the last 50 years, the WCA potential has served as an alternative to the Lennard–Jones potential. It has been extensively used in liquid state theories, and more significantly in molecular simulations of complex systems owing to the inherent computational efficiency.[2–4] Despite its significance in modeling complex systems, there are relatively few studies on the phase diagram of a WCA fluid in three dimensions[5–8]. In two dimensions, to the best of our knowledge, other than the study by Toxværd,[9] there does not exist any study on the phase diagram of a WCA system. Such a dearth is indeed quite surprising and motivated by this we investigated the melting of a two dimensional system with a WCA pair interaction.

In two-dimensional melting, the BKTHNY theory predicts a two step melting process – a solid to a hexatic melting, followed by a hexatic to an isotropic liquid. Both of these transitions are continuous although melting of the hexatic via a first order transition has been observed. In this present work, we consider a system at a fixed temperature and follow the different phases by varying the density. The different phases of the system are identified using the positional and the orientational order parameter, their spatial correlations and their finite size scaling with system sizes. The identification of the two melting points are done using all of these. We find the solid-hexatic melting to be a continuous transition, consistent with the predictions of the KTHNY theory. In contrast, the hexatic-liquid transition turns out to be a first order transition.

The rest of the chapter is organized in the following way. In Section 4.2 we present the details of our model system and the numerical simulations. The identification of the different phases of the system and the two melting points is described Section 3.3. The associated defect formation in the system is presented in Section 3.4 and a discussion on the order of the transition is presented in Section 3.5

3.2 Model and Simulation Details

We consider a two-dimensional interacting colloidal suspension made of 256×256 particles. The particles interact via the WCA potential $U(r) = 4\varepsilon[(r/\sigma)^{-12} - (r/\sigma)^{-6}] + \varepsilon$ for separation $r < r_c$, with $r_c = 2^{1/6}\sigma$. Beyond this separation the pair interaction is

$U(r) = 0$. The cutoff separation r_c is the point at which potential attains its minimum value. The initial configuration of the system is chosen to be that of a triangular lattice with inter particle separation a along the x-direction determined from the density of the suspension: $a^2 = \sqrt{3}\rho/2$. The separation of the lattice planes along the y-direction is given by $a_y = \sqrt{3}a/2$. The quantities ε and σ set the energy and the length scale, respectively.

Molecular dynamics simulations of the system are performed in the presence of Langevin heat bath[10] with an isotropic friction of $\gamma\tau = 1$ and a bath temperature of $k_B T/\varepsilon = 1$, where τ is the characteristic time scale defined as $\tau = \sigma\sqrt{m/\varepsilon}$. The equations of motion are integrated using the standard Leap-Frog algorithm[3] with an integration time step of $\Delta t = 0.001\tau$. Starting from the initial triangular lattice configuration, the system is equilibrated for 10^8 steps, following which statistics is collected over a further 10^7 steps. All simulations were performed using massively parallel home-grown codes implemented on Graphics Processing Units (GPU).

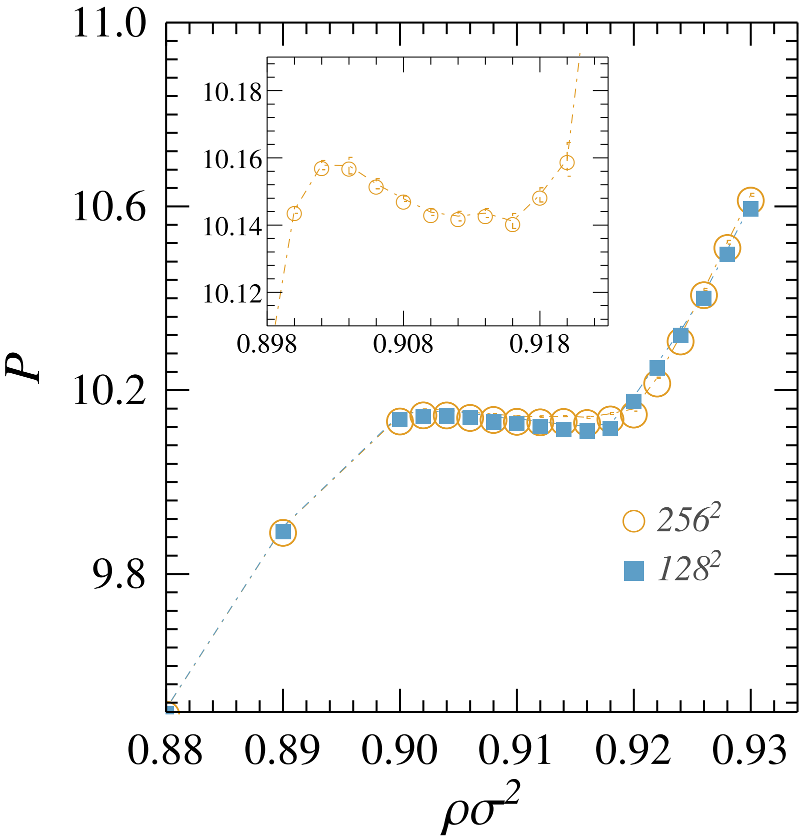

Figure 3.1 Variation of the thermodynamic pressure with density for two different system sizes as indicated inside the plot.The inset depicts a zoomed section of the main plot, for the comparatively larger system size 256^2, to highlight the Meyer-Wood loop within the density range $\rho\sigma^2 = 0.898$ to 0.922.

3.3 Melting point of solid and the hexatic phase

In this section, we present detailed analysis of the solid and the hexatic phases. The different phases are qualitatively identified from the pair correlation function and the static structure factor. Quantitative estimation of the two melting points are done using the solid and the orientational order parameter, their correlation function and finally employing a finite size scaling of the order parameters. We find that at very high densities the system exhibits a stable triangular solid phase with a long range orientational and a quasi long ranged positional order. The solid melts to a hexatic phase at density of $\rho_m\sigma^2 \approx 0.920$, as determined from the pair-correlation function. Decreasing the density further, the hexatic phase becomes unstable at the density $\rho_l\sigma^2 = 0.906$ and goes to an is tropic liquid phase at the density $\rho\sigma^2 = 0.900$ through a weak first order transition.

3.3.1 Thermodynamic Pressure

The first evidence of a first order transition comes from the pressure-density diagram of the system. The thermodynamic pressure is determined from the molecular dynamics trajectories using the virial expression

$$P = k_{\mathrm{B}}T\rho + \frac{\rho}{(2N)}\sum_{i}^{N}\sum_{j>i}^{N}\mathbf{f}(r_{ij})\cdot\mathbf{r}_{ij} \tag{3.1}$$

where $\mathbf{f}(r_{ij})$ is the interaction force and $\mathbf{r}_{ij}$ is the inter-particle separation. At the fixed temperature of $k_{\mathrm{B}}T = 1$, the variation of the pressure with density is shown in Fig. 3.1 for two system sizes - 128^2 and 256^2. The Meyer-Wood loop, characteristic of a first order transition, is very clearly visible within a density range of $0.9 \leq \rho\sigma^2 \leq 0.918$ (see inset of Fig. 3.1), even for the comparatively larger system size with 256^2 particles. Above $\rho\sigma^2 = 0.918$ and below $\rho\sigma^2 = 0.900$, the pressure has a monotonic variation with the density. The onset and the termination of the Meyer-Wood loop gives us an estimate for transition points. We expect the solid-hexatic melting to be around $\rho\sigma^2 \approx 0.920$ and the hexatic-liquid melting to be around $\rho\sigma^2 \approx 0.900$.

3.3.2 Melting of the solid: Solid order parameter

The static structure factor (SSF), defined as $\langle \psi_{\mathbf{q}} \rangle = N^{-1}\langle \rho_{\mathbf{q}}\rho_{-\mathbf{q}} \rangle$ where $\rho_{\mathbf{q}} = \sum_{j=1}^{N} e^{\mathrm{i}\mathbf{q}\cdot\mathbf{r}_j}$ with $\rho_{\mathbf{q}}^{*} = \rho_{-\mathbf{q}}$ is shown in Fig. 3.2 (a)–(f). SSF can clearly distinguish between a solid, hexatic and a liquid phase. In a solid phase, the six-fold symmetry results in Bragg

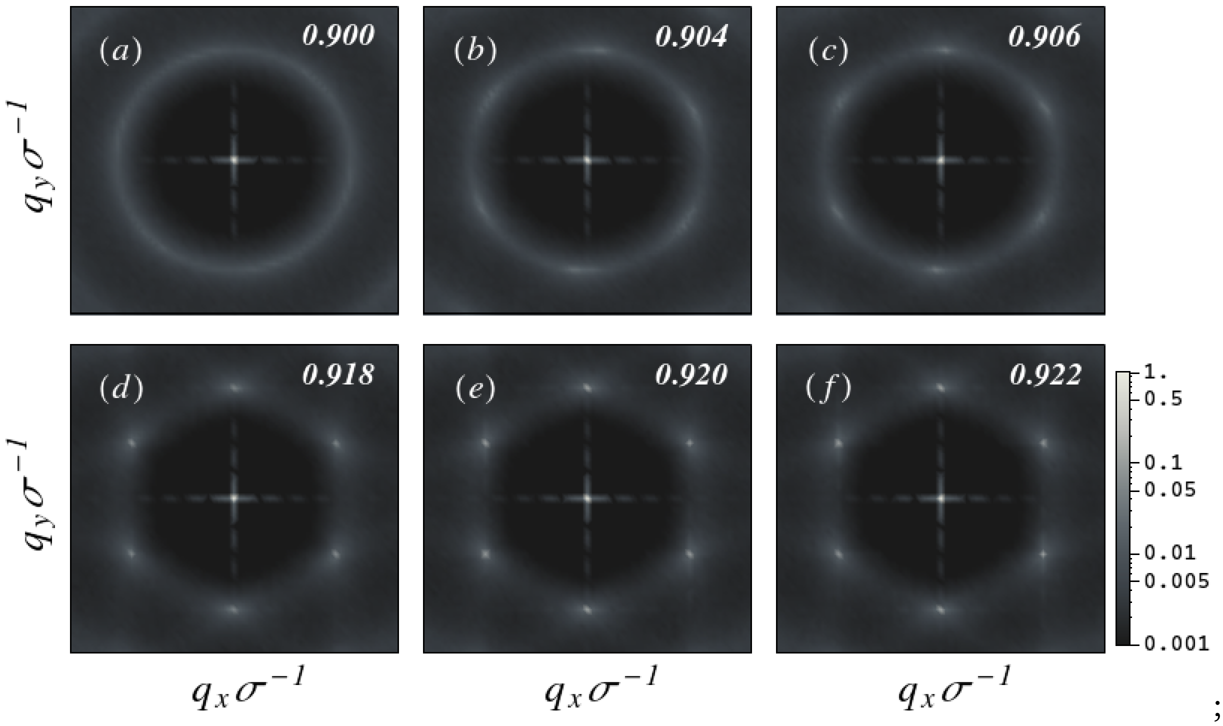

;

Figure 3.2 The static structure factor for different densities of the system as indicated in the legend. $\langle\psi_{\mathbf{q}}\rangle$ is calculated in the Fourier plane with resolution interval of $0.01\sigma^{-1}$.The sequence depicts the melting of the solid to a hexatic and the melting of the hexatic to an isotropic liquid phase.

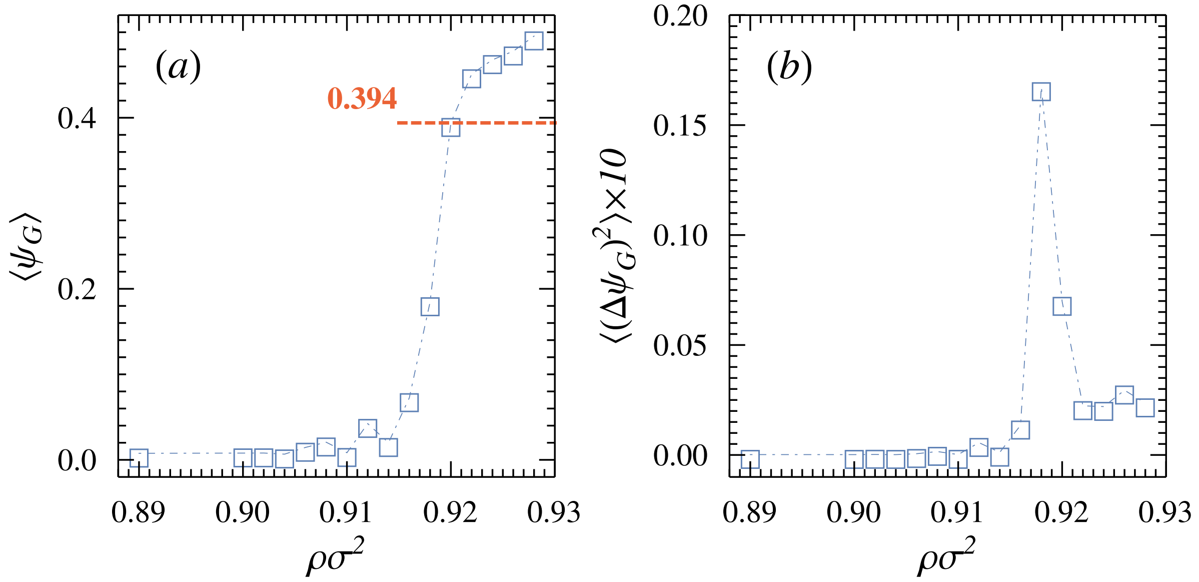

;

Figure 3.3 Plot of the solid order parameter (a) and its fluctuation (b) as a function density. The peak of the order parameter fluctuation occurs at a density $\rho\sigma^2 = 0.918$. Irrespective of the nature of the transition, the peak of the solid order parameter fluctuation indicates the melting of the solid.

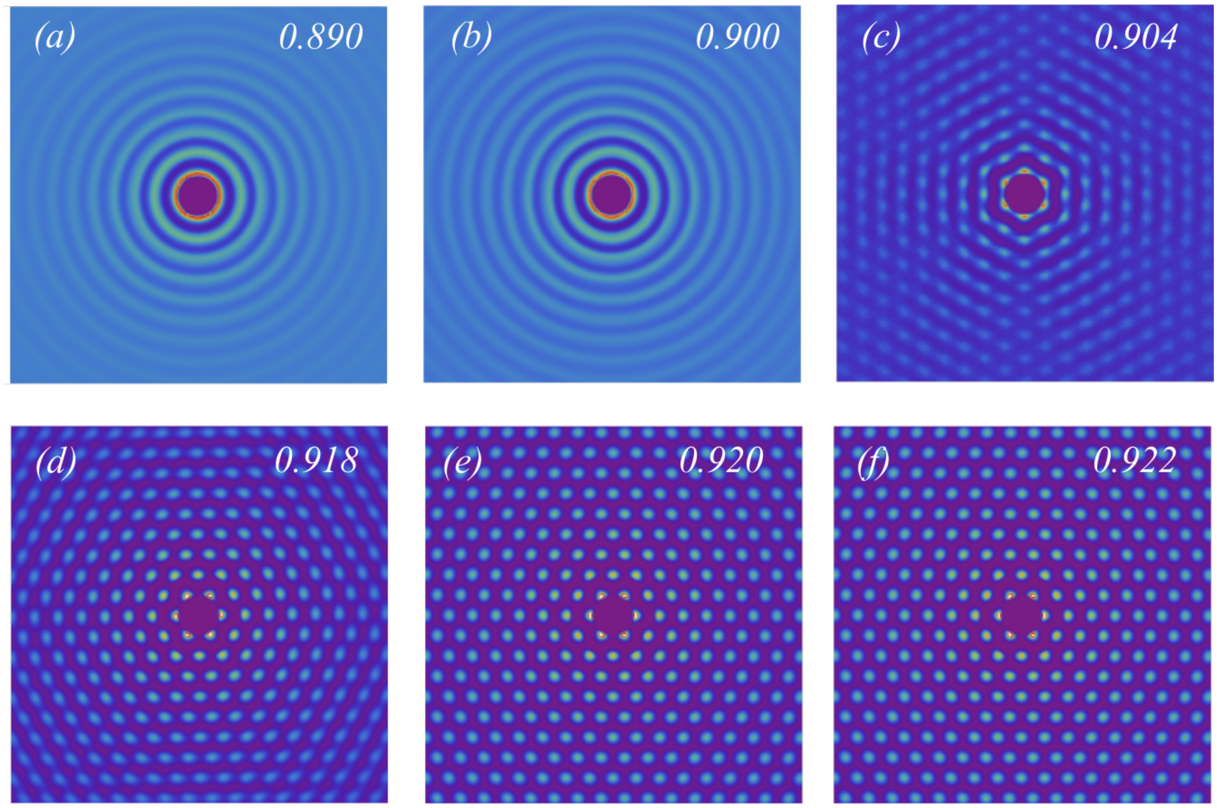

Figure 3.4 Pair correlation correlation $g(x,y)$ is shown for various densities as indicated inside each plot. In the solid phase, $g(x,y)$ shows the characteristic triangular lattice structure. As the solid melts, the triangular lattice structure overlaps with concentric hexagonal rings characteristic of the hexatic phase. In the liquid phase, these hexagonal rings transforms into completely symmetric circular rings that reflects the isotropy of the system.

peaks at the reciprocal lattice vectors $\mathbf{G}_1 = (0, \pm 2\pi/a_y)$ and $\mathbf{G}_2 = (\pm 2\pi/a, \pm\pi/a_y)$ that reflects the underlying triangular lattice structure. Fig. 3.2 (e)–(f) clearly illustrates this fact where the six intensity peaks are distinctly visible. In contrast, in a hexatic phase, the six intensity peaks broaden along a circle of radius $2\pi/a$ (see Fig. 3.2 b–d). Finally, in the liquid phase (Fig. 3.4 a), SSF shows the characteristic uniform ring structure with radius $2\pi/a$ that reflects the isotropy of the system. While the SSF look similar for the densities $\rho\sigma^2 = 0.918$ (figure (d)) and $\rho\sigma^2 = 0.920$ (figure (e)), a closer inspection of the figures reveals that at the density $\rho\sigma^2 = 0.918$ the intensity peaks at $\mathbf{G}_2$ are more diffused and broadened in contrast to the SSF at the density $\rho\sigma^2 = 0.920$. This gives us a qualitative estimate of the solid-hexatic melting point. The melting clearly happens at a density close to $\rho_m\sigma^2 \approx 0.920$.

Additional support to this conclusion comes from the behavior of the solid order parameter and its fluctuations as a function of the density of the system. Since the static structure factor can distinguish between a solid and a hexatic phase from the appearance of the intensity peaks at $\mathbf{G}_2$, the average of these intensity peaks $\langle\psi_{\mathbf{G}_2}\rangle$ serves as

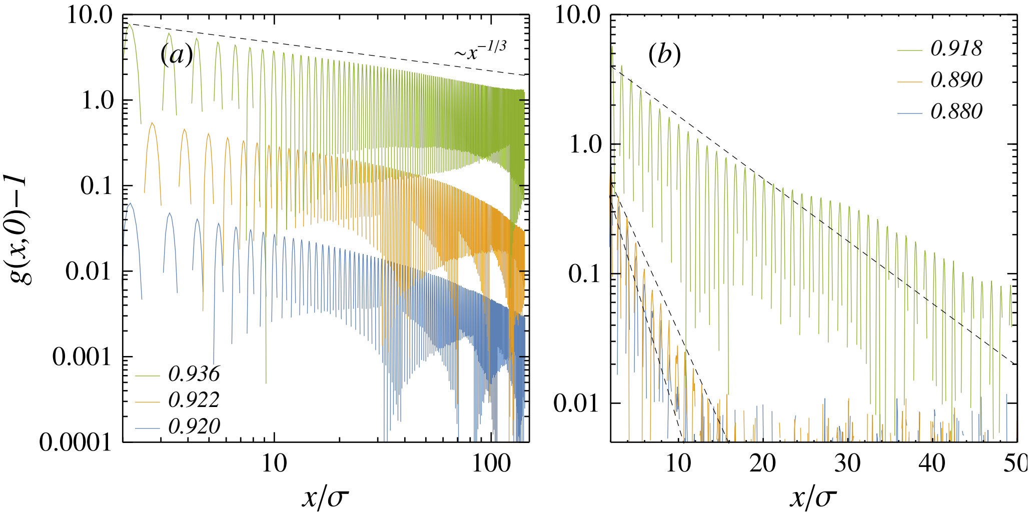

Figure 3.5 The cut of the pair correlation $g(x,0)-1$ is shown in the double-logarithmic scale in (a) and in log scale in (b) for the densities indicated in the legend. The black dashed line shows the plot of $x^{-1/3}$ that identifies the stable solid phase. From the decay of the correlation, the hexatic-solid transition happens at the point $\rho\sigma^2 = 0.920$. For the densities below this point, there is an exponential decay observed in the pair correlation function.

---

the order parameter of the solid-hexatic transition. In determining the solid order parameter from the simulations, we observed that the four diagonal peaks with maximum intensity were shifted from the expected value of $\mathbf{G}_2$.Accordingly, we monitored the intensity values around $\mathbf{G}_2$ in region of $0.8 \times 0.8\sigma^{-2}$ and the maximum intensity value was taken as the order parameter (see 3.6 (c) – (f)). In Fig. 3.3 (a) we show the solid order parameter $\langle \psi_{\mathbf{G}_2} \rangle$ as function of the density of the system. At very high densities, when the system remains in a triangular solid phase, the solid order parameter shows a high value and monotonically decreases as the density of the system is decreased. For densities below $\rho\sigma^2 \leq 0.92$, $\langle \psi_{\mathbf{G}_2} \rangle$ shows vanishingly small values, in agreement with our earlier conclusion. The fluctuations of the order parameter give a more quantitative estimate. A plot $\langle \Delta\psi^2_{\mathbf{G}_2} \rangle$ as a function of density in Fig. 3.3 (b) shows that the fluctuations are maximum around the density $\rho\sigma^2 = 0.918$. Since the peak of the fluctuation is indicative of the transition point, irrespective of the nature of the transition, the melting of the solid happens at a density $\rho\sigma^2 = 0.918$. It is worth noting that the solid order parameter and its fluctuations are quantities that are averaged over the system. Even though we get a fairly good estimate of the transition point, neither the average solid order parameter nor the fluctuations can spatially resolve the translational order in the system.

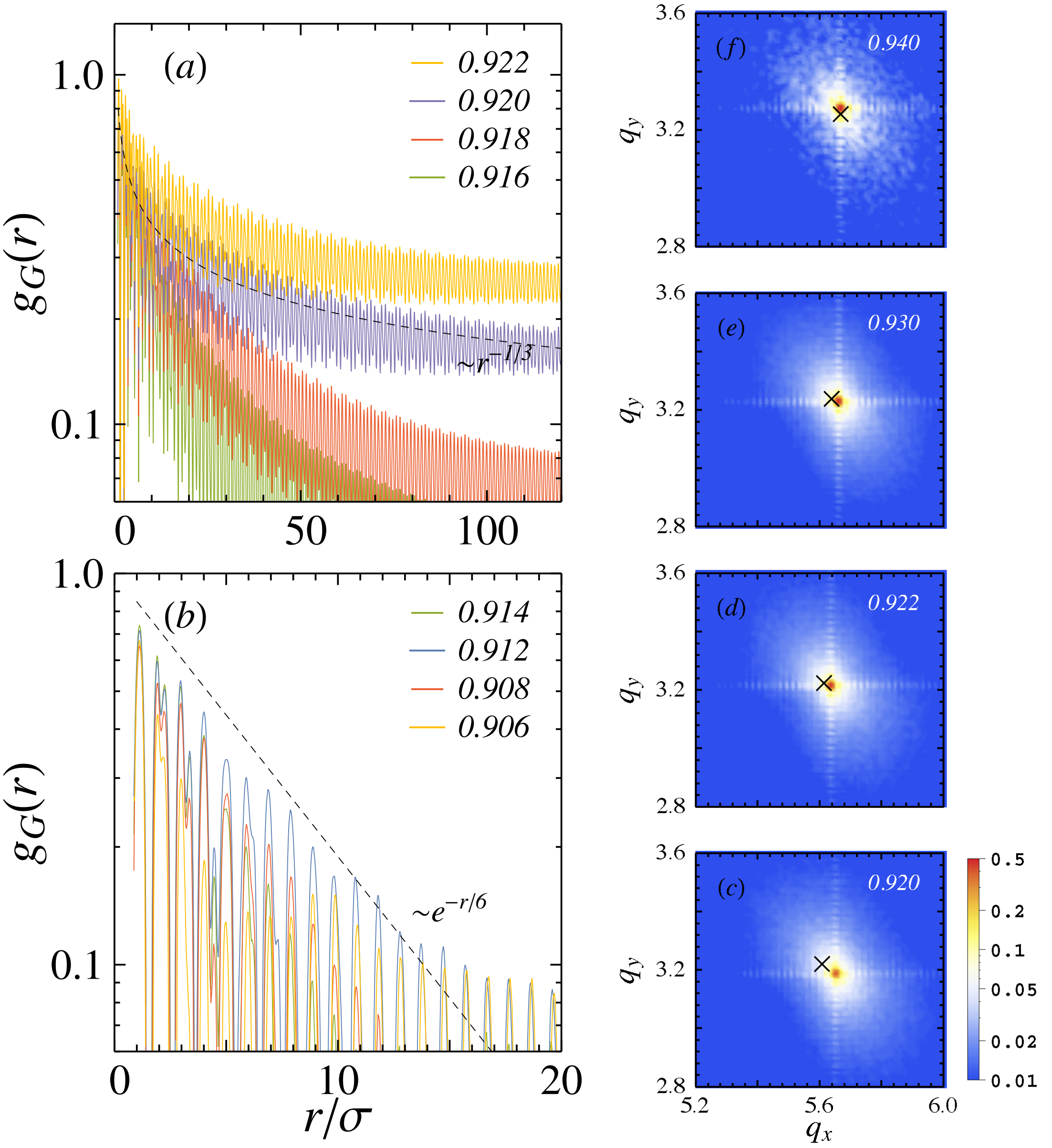

Figure 3.6 (a)–(b):The spatial correlation of solid order parameter $g_{\mathbf{G}}(r)$ is shown in the double logarithmic scale for the densities indicated in the legend. Here $\mathbf{G} = 2\pi/a$ is one of the reciprocal lattice vector out of six vectors, at which Bragg peaks are obtained in the static structure factor plane for the stable solid phase. The black dashed line shows the plot of $r^{-1/3}$ to clearly identify the solid-hexatic melting point. At densities below $\rho\sigma^2 = 0.920$, the decay of the correlation is short-ranged. **(c)–(f)**: Sequence of plots that depicts the shift in $\mathbf{G}_2$ for different densities.

3.3.3 Melting of the solid:Correlation function

A further qualitative confirmation of the solid melting is obtained from the pair correlation function $g(x,y)$ and its cut along the x direction. The two dimensional pair correlation function, defined as $g(x,y) = \langle\rho(x,y)\rho(0,0)\rangle/\langle\rho\rangle^2$, is shown over a length scale of $\pm 10\sigma$ in Fig. 3.4 for a sequence of densities that capture the solid-hexatic and the hexatic-liquid melting.In determining the correlation function, the system was divided in a grid of 4096×4096. The subsequent histogram was averaged over 200 independent configurations. Care was taken to orient the independent configurations such that the x corresponded to the sample orientation.

At densities above the $\rho\sigma^2 \geq = 0.92$, the pair correlation function shows the characteristic triangular lattice structure. With the melting of the solid, the correlation changes to local diffused triangular symmetry that is characteristic of the hexatic phase. This is evident in the plot of $g(x,y)$ for the density $\rho\sigma^2 = 0.918$ (figure (d)). Upon decreasing the density further, as the transition to the liquid phase approaches, the triangular symmetry in the pair correlation is completely lost and the diffused structures are replaced by concentric hexagonal rings (see Fig. 3.4 (c)). In the liquid phase, the correlation reflects the isotropy of the system and we observe concentric circular rings as depicted in Fig. 3.4 (a)–(b).

The melting point of the solid is identified from the cut of the pair correlation function $g(x,0)-1$. The KTHNY theory predicts a quasi-long range translational order in the solid phase. Accordingly, the pair correlation exhibits an algebraic decay with an exponent $\eta(\rho) \leq 1/3$. In the KTHNY theory, $\eta^* = 1/3$ marks the boundary of the stable solid phase. In contrast, in the hexatic phase, the correlation is short ranged and decays exponentially. The measured data for $g(x,0)-1$ is shown in Fig. 3.5 for different densities as indicated in the legend. At high densities, the correlation indeed decays with a power law crossing over to an exponential decay, in conformation with the predictions from KTHNY-theory. The solid-hexatic melting transition point is identified using the criteria $\eta(\rho_m) = 1/3$. The lowest density at which the the correlation shows a power law decay with exponent η^* is identified as the solid-hexatic melting point. This happens at the density $\rho\sigma^2 = 0.920$ as shown in Fig. 3.5 (a). Below this density, the correlation shows an exponential decay (see figure Fig. 3.5 (b)).

We get an identical result on the solid-hexatic melting point from the correlation of the solid order parameter. The solid order parameter correlation function is defined as $g_{\mathbf{G}}(r) = \langle \psi_{\mathbf{G}_2}(\mathbf{r}+\mathbf{r}')\psi_{\mathbf{G}_2}(\mathbf{r}')\rangle$. We show this correlation in Fig. 3.6 (a) and (b). We note that the correlation $g_G(r)$ was evaluated at the reciprocal lattice vector which showed the maximum intensity peak in the $q_x - q_y$ plane (see Fig. 3.6 (c) – (f)). The KTHNY theory of melting predicts a quasi long-ranged positional order at densities above the melting point that transforms into a short ranged order below the melting. Accordingly, $g_{\mathbf{G}}(r)$ is quasi-long ranged with a power law decay and as the solid melts the correlation becomes short ranged. In Fig. 3.6 (a), we observe an asymptotic power law decay with an exponent η^* at a density $\rho\sigma^2 = 0.920$. Above this density, the correlation always decays as a power law with an exponent $\eta < \eta^*$, indicating a stable solid phase. On the other hand, Fig. 3.6 (b) shows that for densities below $\rho\sigma^2 = 0.920$, the decay of the correlation is short ranged.

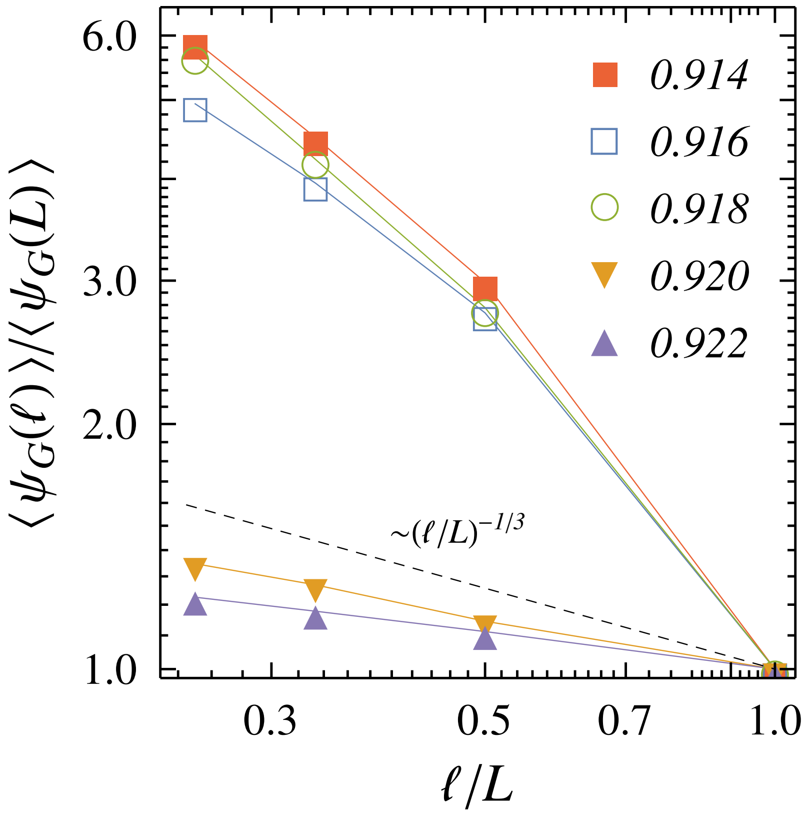

Figure 3.7 Finite size scaling of solid order parameter ψ_G in double logarithmic scale. The dashed black line is the plot of $(\ell/L)^{-1/3}$ slope that indicates the boundary of the stable solid phase. For densities $\rho\sigma^2 \geq 0.920$ the system goes into a stable solid phase and $\rho\sigma^2 = 0.920$ is the solid-hexatic melting point.

3.3.4 Melting of solid:Finite size scaling

The final corroboration for the melting transition comes from the finite size scaling analysis of the solid order parameter. To evaluate the finite scaling, we divided the system into sub-blocks of sizes $\ell_x \times \ell_y = \ell^2$ and determined the solid order parameter in these sub-boxes. As defined for the global system, the same definition of the solid order parameter was used for the particles contained in the sub-boxes. KTHNY theory predicts that the ratio $\langle\psi_{\mathbf{G}_2}(\ell)\rangle/\langle\psi_{\mathbf{G}_2}(L)\rangle \sim (\ell/L)^{-\nu}$ with $\nu \leq 1/3$ in a stable solid phase. In Fig. 3.7 we present the results of our finite size scaling analysis. We observe that for densities $\rho\sigma^2 \geq 0.920$, the ratio $\langle\psi_{\mathbf{G}_2}(\ell)\rangle/\langle\psi_{\mathbf{G}_2}(L)\rangle$ decays as $(\ell/L)^{-\nu}$ with the exponent $\nu < 1/3$, indicating a stable solid phase. As the density becomes lower than $\rho\sigma^2 = 0.920$, the finite size scaling shows that the solid becomes unstable, and consequently the density $\rho\sigma^2 = 0.920$ marks the melting transition of the solid. The absence of power law scaling in $\langle \psi_{\mathbf{G}_2}(\ell) \rangle / \langle \psi_{\mathbf{G}_2}(L) \rangle$ for densities below the melting point is reflective of the fact that the solid order parameter correlation decays exponentially in the hexatic as well as in the liquid phase.

Since the pair-correlation function, the solid order parameter correlation and the finite size scaling of $\psi_{\mathbf{G}_2}$ resolves the positional order even at the largest length scale of the system, we conclude that the melting of the solid to a hexatic phase happens at $\rho_m\sigma^2 = 0.920$.

3.3.5 Hexatic melting: Order parameter

Once the triangular solid melts, it does not go into an isotropic liquid phase but rather retains some orientational order. The phase is characterized by a quasi long range orientational order and a short-ranged positional order. This is the hexatic phase. With the melting of the solid at a density of $\rho\sigma^2 = 0.92$, the system goes into a hexatic phase. Following the pair-correlation function shown in Fig. 3.4, we observe that at a density of $\rho\sigma^2 = 0.902$, the correlation shows a diffused hexagonal concentric rings that is characteristic of the hexatic phase. It is worth noting that at the lower density of $\rho\sigma^2 = 0.900$, even though concentric circular rings are clearly visible in the correlation $g(x,y)$, the innermost ring is non-uniform and has the signature of a hexatic phase. In contrast, the pair correlation function at a density $\rho\sigma^2 = 0.890$ shows rings of uniform intensity underlying the isotropy of the system. This qualitative comparison gives us the first estimate of the hexatic melting point as $\rho\sigma^2 \approx 0.902$. We proceed to have a more quantitative estimate. To this end we first look at the orientational order parameter ψ_6.

In defining the hexatic bond orientational order parameter, we utilize a measure for the local hexatic order, that is,

$$\langle \psi_6 \rangle = \left\langle \left| \frac{1}{N} \sum_{i=1}^{N} \psi_6^i \right|^2 \right\rangle \tag{3.2}$$

where ψ_6^i is the local hexatic order defined for a particle as $\psi_6^i = \sum_{j=1}^{n} (\ell_i/\ell) e^{\mathrm{i}6\theta_{ij}}$ with n being the number of Voronoi neighbors.The angle θ_{ij} is defined as the angle made by the separation vector $\mathbf{r}_{ij}$ with the x axis. The definition of the local hexatic order utilizes a weighted average of the exponentials with the weight factor ℓ_i/ℓ such that $\sum_{i=1}^{n} \ell_i = \ell$ with ℓ_i denoting the length of the Voronoi edge corresponding to the j-th neighbor.[11] The average $\langle \psi_6 \rangle$ serves as the orientational order parameter for the hexatic-liquid transition. The measured values of $\langle \psi_6 \rangle$ as a function of density are shown in Fig. 3.8. In the solid phase, the orientational order parameter has a value $\langle \psi_6 \rangle > 0.5$ and decreases monotonically as the system density is decreased. The average ψ_6 becomes vanishingly small at densities below $\rho\sigma^2 = 0.902$.

In order to fix the melting point of the hexatic, we also look at the fluctuations of the orientational order parameter $\langle \Delta\psi_6^2 \rangle$ as a function of density. Irrespective of the nature of the transition, the fluctuations of the order parameter peak at the transition point. This is illustrated in Fig. 3.8 (b) which depicts the measured values of $\langle \Delta\psi_6^2 \rangle$ from the simulations as the density of the system is varied. The maximum of the order parameter fluctuations is observed at a density $\rho\sigma^2 \approx 0.906$, giving us the first estimate of the melting point. To confirm the transition point, we focus our attention on the correlation of the ψ_6.

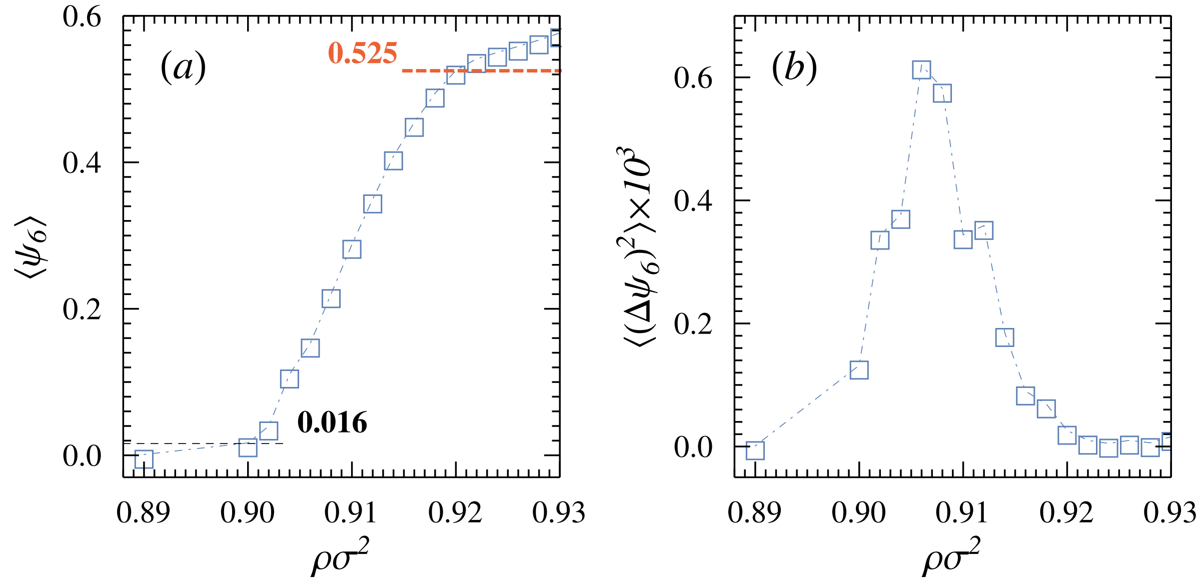

Figure 3.8 Plot of the bond orientational order parameter (a) and its fluctuation (b) as a function density. The peak of the order parameter fluctuation occurs at a density $\rho\sigma^2 = 0.906$.

3.3.6 Hexatic melting: Order parameter correlation

The orientational order parameter correlation $g_6(r)$ is defined as

$$g_6(r) = \langle \psi_6^{i*} \psi_6^{j} \delta(r - r_{ij}) \rangle \tag{3.3}$$

where ψ_6^{i*} denote the complex conjugate of ψ_6^{i}, the local bond orientational order and r_{ij} is the separation between a pair. The identification of the hexatic melting is done from the nature of the decay of $g_6(r)$. In the solid phase the orientational order parameter is long-ranged that transforms to a quasi-long ranged behavior in the hexatic phase, decays algebraically with an density dependent exponent $\eta_6(\rho)$. The upper bound of this exponent is predicted by the KTHNY theory. A stable hexatic phase is identified with the value of the exponent $\eta_6 \leq 1/4$ with the equality happening at the melting point of the hexatic. Once the hexatic melts to an isotropic liquid, the correlation becomes short ranged, decaying exponentially. Accordingly, in the solid phase we observe no decay in $g_6(r)$ as depicted in Fig. 3.9 for the density $\rho\sigma^2 = 0.920$, the melting point of the triangular solid. In contrast, once the solid melts, the correlation exhibits a power law decay with an exponent $\eta_6 \leq \eta_6^*$. Looking at the decay of $g_6(r)$, we observe that the hexatic becomes unstable for densities $\rho\sigma^2 < 0.906$. At the density $\rho\ s^2 = 0.906$ the exponent is exactly $1/4$. Even though this estimate is slightly higher than the qualitative prediction from the pair correlation function $g(x,y)$, it is in excellent agreement with the value obtained from the quantitative estimate using the fluctuations of the order parameter. Additionally, we also observe that for densities close to $\rho\sigma^2 = 0.906$, but below it, the correlation does not exhibit an exponential decay throughout. Rather, the asymptotic decay appears to be a power law with an exponent greater than η_6^*.

3.3.7 Hexatic melting: Finite size scaling

The final piece in this puzzle is the finite size scaling of the hexatic order parameter. In order to study the finite size scaling of ψ_6, we divided the system into sub-boxes of size $\ell_x \times \ell_y = \ell^2$.The particle based definition of the local hexatic order ρ_6^i was used in determining the orientational order parameter $\psi_6(\ell)$ for a specific box and $\langle\psi_6(\ell)\rangle$ was obtained by averaging over the boxes of same size ℓ. The ratio $\langle\psi_6(\ell)\rangle/\langle\psi_6(L)\rangle$, where $L_x \times L_y = L^2$, as a function of ℓ/L is shown in Fig. 3.10. The KTHNY theory predicts that $\langle\psi_6(\ell)\rangle \sim \ell^{-\eta_6}$ with $\eta_6 \leq \eta_6^* = 1/4$. The boundary of a stable hexatic phase is marked by $\langle\psi_6(\ell)\rangle/\langle\psi_6(L)\rangle \sim (\ell/L)^{-1/4}$. From the measured data on finite size scaling, we see that for densities $\rho\sigma^2 \leq 0.902$, the decay of the ratio is faster than $(\ell/L)^{-1/4}$ and therefore do not form a stable hexatic phase. In contrast for densities $\rho\sigma^2 \geq 0.906$, the ratio decays with an exponent less than η_6^*. We conclude that the hexatic – liquid melting transition happens at the density $\rho_l\sigma^2 = 0.906$.

3.4 Defect formation in the system

In this section, we discuss the defect formations in the system, as the system melts from solid to a hexatic and then to an isotropic liquid. The KTHNY theory predicts that this two-step melting is a defect mediated transition. A topological defect is identified by

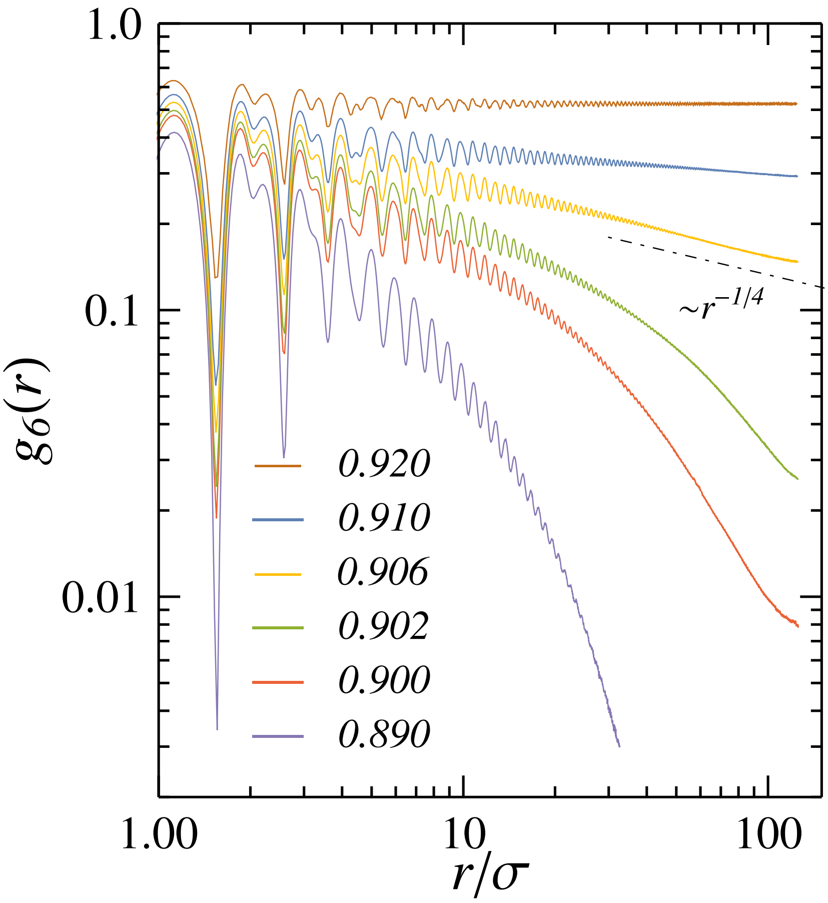

Figure 3.9 Spatial correlation of the orientational order parameter $g_6(r)$ is shown for different densities. At the density $\rho\sigma^2 = 0.920$, the orientational order is long ranged and does not exhibit a decay. As the solid melts to a hexatic, the long ranged order transforms into a quasi-long ranged order and the correlation decays as a power law with an exponent $\eta \leq 1/4$. In the liquid phase the correlation becomes short-ranged, decaying exponentially.

the coordination number of a particle. In a perfect triangular lattice that is defect free, the coordination number of each particle is $n_v = 6$. The coordination number itself is a dynamically varying quantity and changes with time as the particles rearrange. A n_v-fold defect is identified with a particle whose coordination number is n_v, with $n_v \neq 6$. Of interest are three types: quartets which are $5-7-5-7$ defects, dislocation which are $5-7$ defect pairs and disclinations which are isolated 5 and 7 fold defects.

At densities above the solid melting point, the formation of the defects is suppressed. Quartets form the majority of the defects in the solid phase and the melting of the solid is mediated by the dissociation of these quartets into dislocations. The presence of these dislocations marks the hexatic phase of the system. A further dissociation of the dislocations into free disclinations takes the hexatic phase into an isotropic liquid.

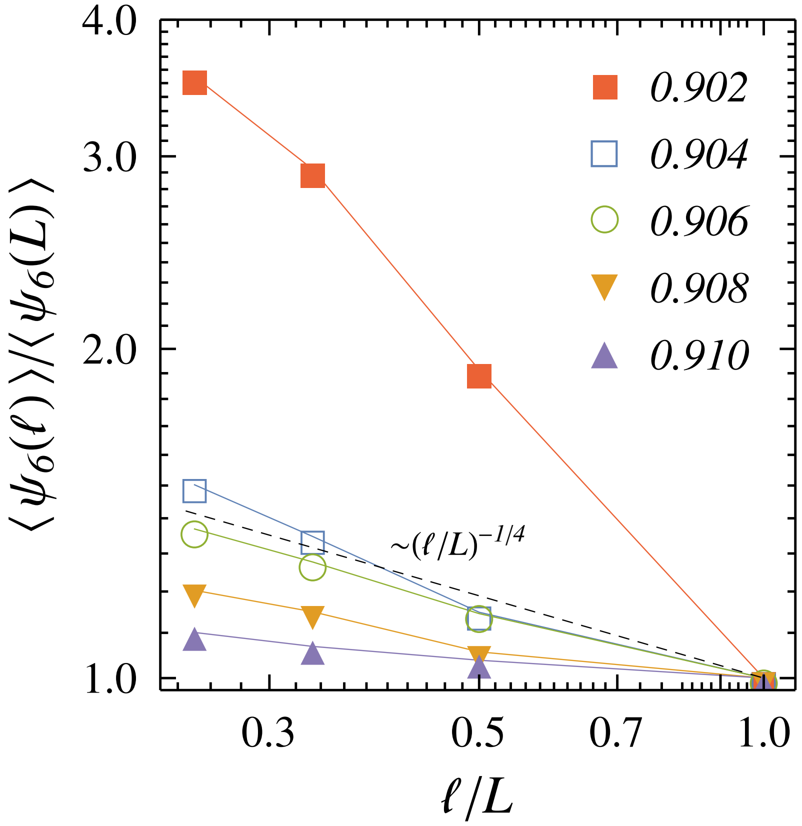

Figure 3.10 System size scaling of orientational order parameter ψ_6 for the densities indicated in the legend. The dashed line indicates the $-1/4$ slope and is the boundary of a stable hexatic. The data shows that for densities $\rho\sigma^2 > 0.906$ the system is in a stable hexatic phase.

To validate this picture, we followed the different types of defects in the system. We used Voronoi tessellations to identify the nearest topological neighbors of a given particle. The number of topological neighbor of a given particle was denoted as the coordination number n_v of the particle. Accordingly, we estimated the number of different types of defects by keeping track of particles with $\eta_v \neq 6$. In Fig. 4.17 (a) we show the percentage fraction of defects $d_f = N_d/N \times 100$ as a function of density. N_d is the total number of particles with $n_v \neq 6$, that is $N_d = (N - n_6)$, where N is the total particle number. We clearly observe that above the melting of the solid, the percentage fraction of defects are negligibly small and in a liquid phase, d_f increases by almost an order of magnitude. In addition to this, we also show the percentage fraction of rest of the defects that are not quartets, dislocations or disclinations in the same figure. Fig. 4.17 (b) explicitly shows the percentage fraction of quartets, dislocations and disclinations in the system as the density is varied. In the solid phase, the dominant defect types are that of quartets. As the density is decreased the percentage fraction of dislocations starts to increase. For a closer look at these defect formations at a given density, we ask a different question. Given N_d at a fixed density, what fraction of these defects form quartets, dislocations or disclinations? We estimate this using the quantity $d_c = n_d/N_d \times 100$, where

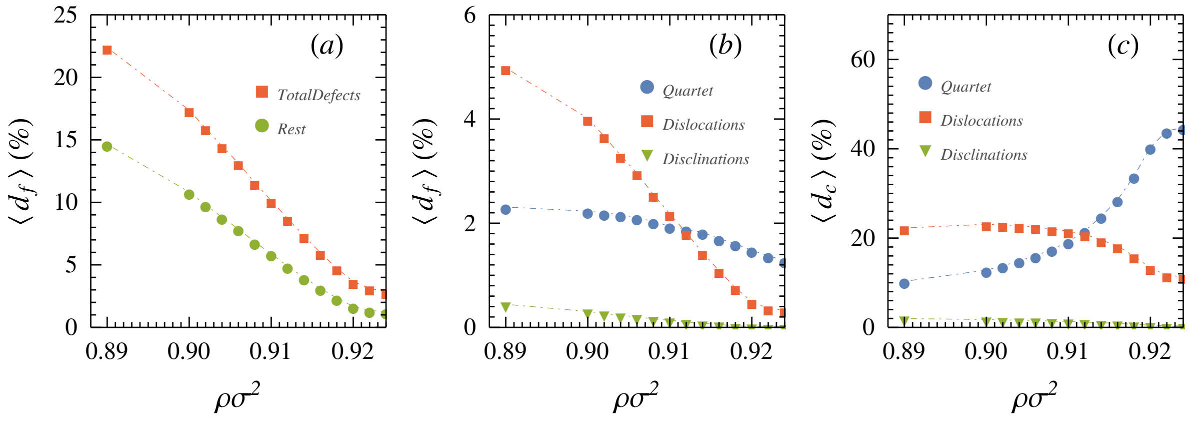

Figure 3.11 **(a)**: Variation of percentage defect-fraction d_f with system density $\rho\sigma^2$. **(b)**: The percentage fraction of quartets, dislocations and disclinations are shown as a function of the system density. **(c)**: Plot of the quantity d_c, the percentage fraction of 5 fold and 7 fold defects that contribute to form either a quartet, dislocation or disclination, as a function of density.

---

n_d is the total number of defects that contribute to form either a quartet, a dislocation or a disclination. In Fig. 4.17 (c) we show the variation of d_c as a function of density. At high densities, when the system is in a triangular solid, almost half of the defects in the system are bound as quartets. As the density of the system is decreased, the fraction of quartets also decreases and the number of defects contributing to dislocations increases. This dissociation of quartets into dislocations mediates the melting of the solid is consistent with the KTHNY theory. We note that the quartets do not altogether vanish as the system melts to an isotropic liquid, but rather the percentage fraction of quartets becomes a constant.

The melting of the hexatic into an isotropic liquid does not follow the KTHNY scenario – there is no significant increase in the percentage fraction of free disclinations as the density is varied. Instead, as the hexatic melts to a liquid, we observe connected $5-7$ defects that forms strings and compact clusters appear in the system (see Fig. 3.12).

To have a clear picture, we looked at the Voronoi tessellations of a configuration of size $20\sigma \times 20\sigma$ and color coded the particles according to their coordination number n_v : 4 (violet), 5 (green), 6 (sky blue) 7 (red) and 8 (yellow). In the solid phase (Fig. 3.12 (a)) defects are bound in the form of quartets. As the density is decreased, the dislocations increase in the system Fig. 3.12 (b). But along with this, we also observe the appearance of clusters of connected defects which dominate in the liquid phase (see Fig. 3.12 (c)–(d)). The percentage fraction of disclinations in the system remains significantly low. To correlate the defects with the local orientational order, we have also shown the corresponding Voronoi tessellations colored according to the local hexatic order in Fig. 3.12 (e)–(h).

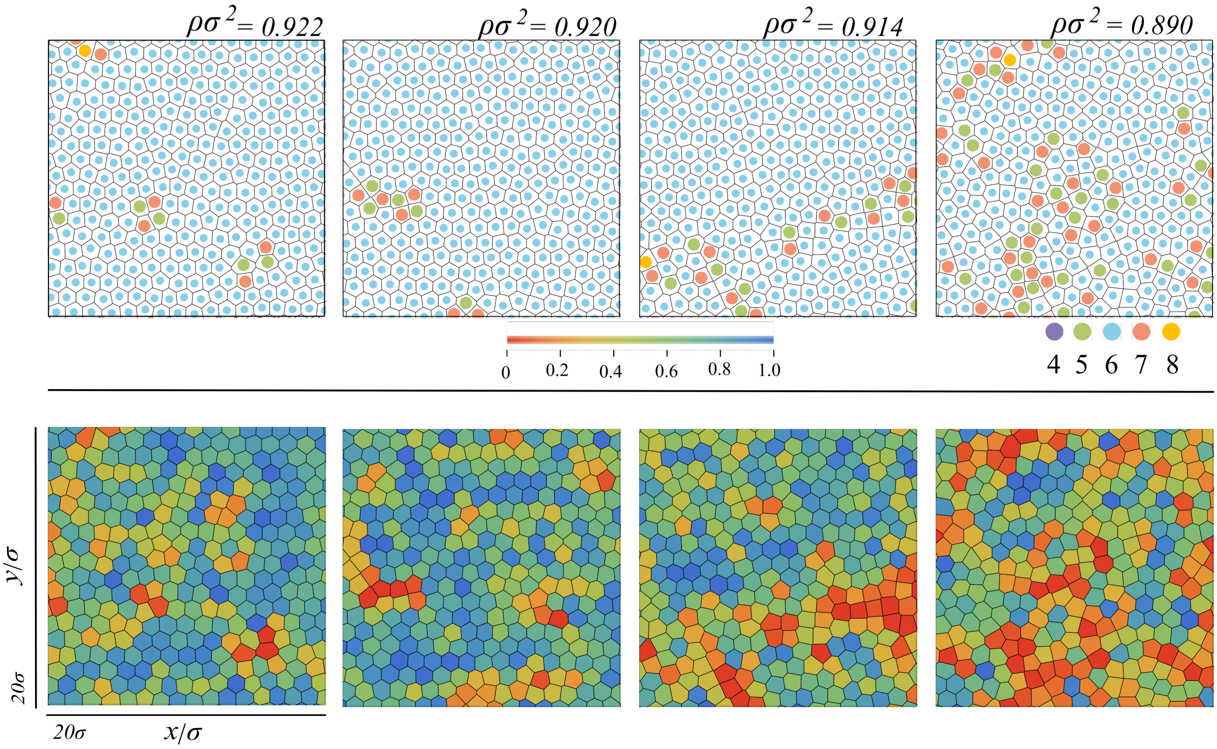

Figure 3.12 Defects formation and its effect on local orientation order is shown for different phases of the system. In the top panel, particles with different number of neighbors are shown inside their respective voronoi cells. They can be distinguished by different colors given to them. The legend at the bottom of the extreme right plot represents this color code. In the solid phase $\rho\sigma^2 = 0.922$ (a) and 0.920 (b), defects mostly appear in the form of dislocation-pairs. Figure (c) shows that the number of defects is increased at the density $\rho\sigma^2 = 0.914$ and the major contribution is coming from free dislocations. In the liquid $\rho\sigma^2 = 0.890$ (d) the defect-density becomes very high. The bottom panel replicates the same system area as above. The corresponding voronoi cells are color-coded with the local orientational order values. These figures clearly indicate that the deformation caused by defects formation lowers the orientational order in the system. The results shown here are obtained from a single snap shot.

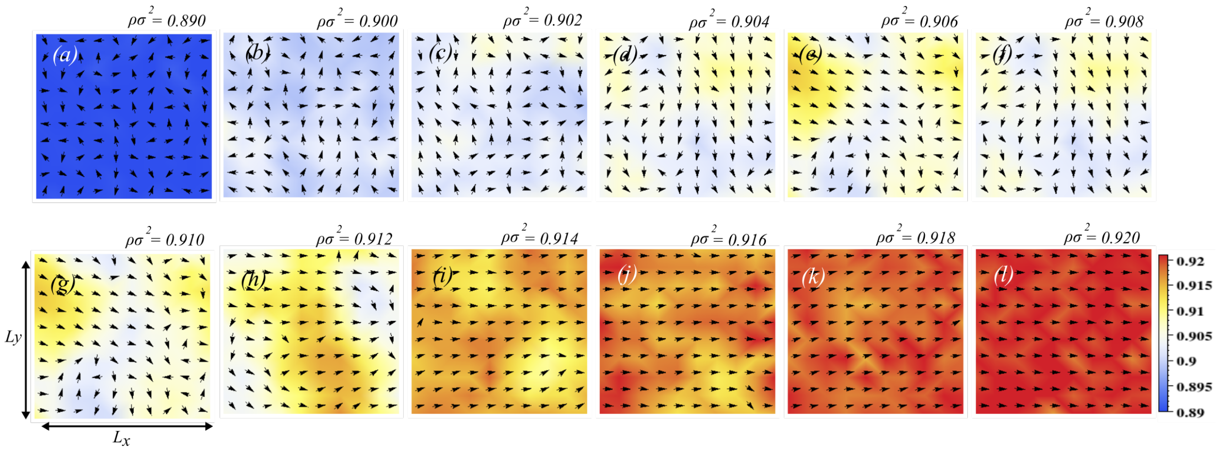

Figure 3.13 Sequence of plots that shows the spatially resolved and time-average density profiles for the whole system. The system was divided in a grid of 10×10 with each sub-box dimension $L_x/10 \times L_y/10$. The average system densities are indicated on the top of the figures. Overlapped on this are plots of the average local orientational order in the sub-box (for a single configuration) as indicated by the arrows. In the solid phase, the density is uniform and there is a long range orientational order. As the solid melts ($\rho\sigma^2 < 0.920$) to a hexatic phase, coexistence of phases with different densities is observed in the system. The high and the low density phases are associated with long and short ranged orientational order, respectively.

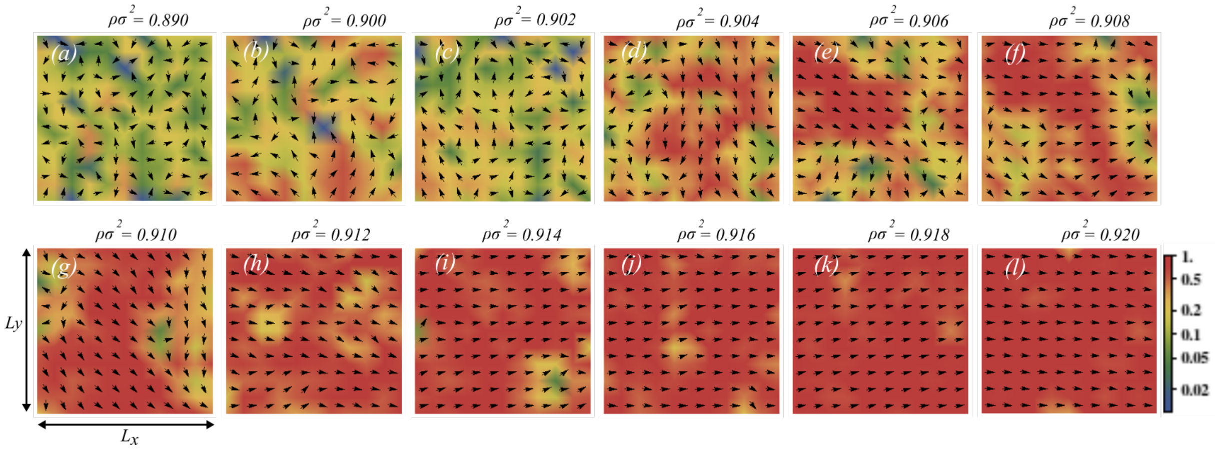

Figure 3.14 Sequence of plots that shows the spatially resolved orientational order for the whole system for a single configuration. The system was divided in a grid of 10×10 with each sub-box dimension $L_x/10 \times L_y/10$. The different densities are indicated on the top of the figures. Overlapped on this and indicated by the arrows, are plots of the local orientational order averaged in the sub-box. In the solid phase, there is a long range orientational order. As the solid melts to a hexatic phase, in the density range of $0.910 < \rho\sigma^2 \leq 0.920$, there isolated regions of low orientational order in the system. In contrast, in the density regime $0.900 \geq \rho\sigma^2 \leq 0.910$, coexisting phases with high and low orientational order is observed in the system.

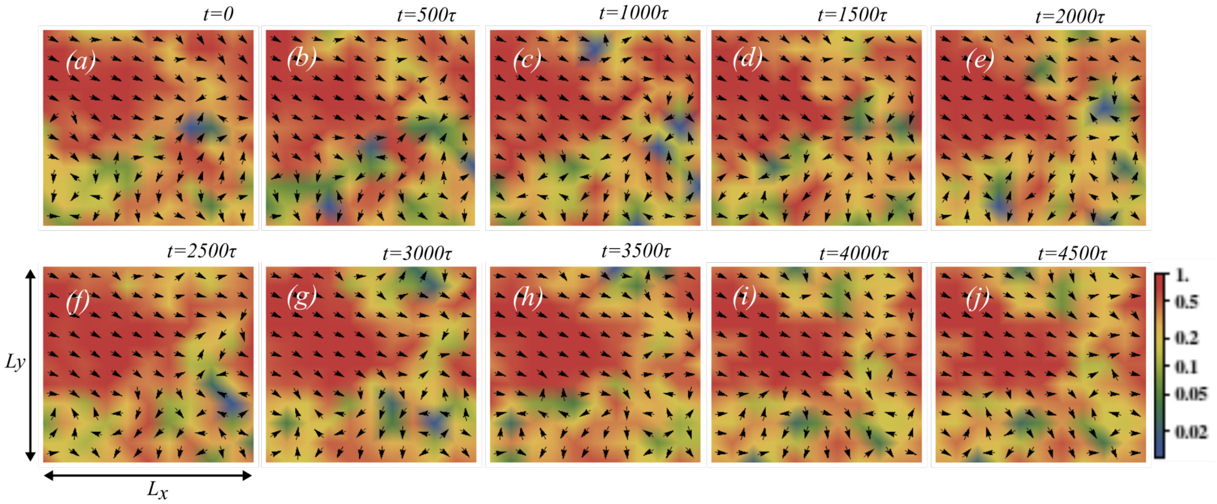

Figure 3.15 Time evolution of coarse-gained orientational order at the density $\rho\sigma^2 = 0.906$. The heatmap at each time snapshot was obtained by dividing the whole system into 10×10 blocks.The local orientational order $\psi_6(\mathbf{r})$ is calculated inside each block using the particle based definition ψ_6^i and restricting the sum in Eq. (3.2) over the sub-boxes. Overlapped on the heatmap are the local orientation vectors $(\mathrm{Re}\ \psi_6(\mathbf{r}), \mathrm{Im}\ \psi_6(\mathbf{r}))$ indicated by the arrows. The time evolutions indicate a stable macrophase separation of high and low hexatic order.

3.5 Order of the transitions

The final piece in this melting scenario comes from the study of the order of the transition. Our earlier discussions have given us a clue to the nature of the transitions in the system. All of these – thermodynamic pressure, pair-correlation, solid order parameter correlation, finite size scaling and defect formations in the system hint towards a continuous melting of the solid to a hexatic phase. In contrast, the hexatic-liquid melting exhibits signatures of the KTHNY theory in the correlation function of the orientational order parameter and its finite size scaling, but the thermodynamic pressure and the defect formation indicate otherwise.

To ascertain whether the solid hexatic melting is continuous, we measured the solid order parameter in a sub-box of size $L_x/10 \times L_y/10$ and looked at the distribution of these order parameters as depicted in Fig. 3.16. At the solid-hexatic melting point of $\rho_m\sigma^2 = 0.920$, the distribution is uni-modal with a peak at $\psi_G^\ell \approx 0.6$. As the density is decreased, the peak shifts to lower values indicating the melting of the solid. The uni-modal nature of the distribution, as the peak shifts to lower values, indicates the absence of any metastable states, a feature of a continuous phase transition.

The first attempt to study the melting of the hexatic is to look at the transition qualitatively. For this, we divide the whole system in a grid of 10×10 and measure the

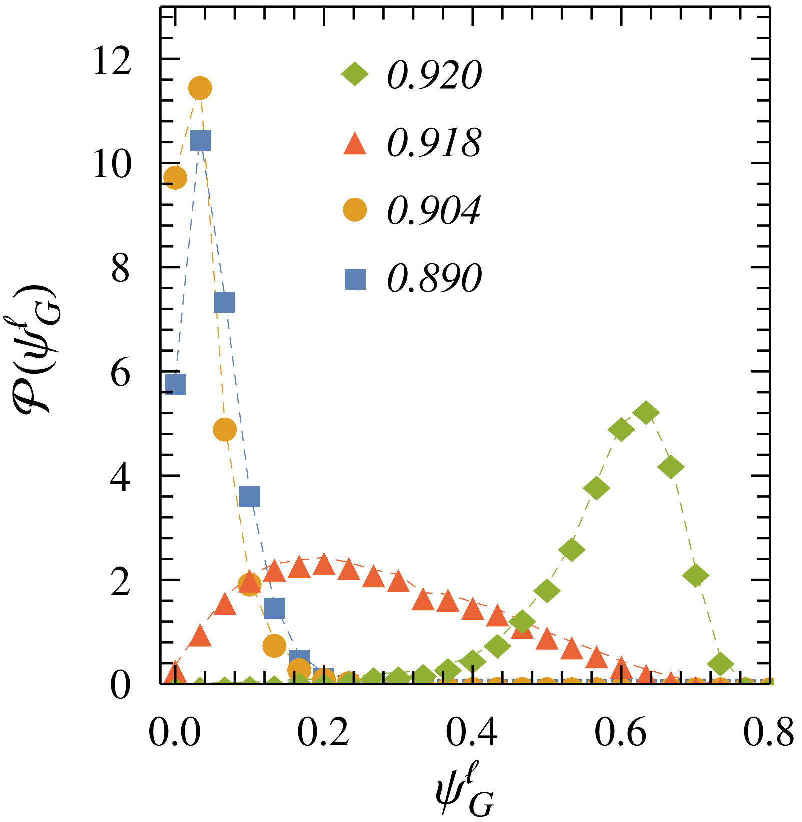

Figure 3.16 Distribution of the solid order parameter ψ_G^ℓ in a sub-system of size $L_x/50 \times L_y/50$ for different densities as indicated in the legend. At the solid-hexatic melting point of $\rho_m\sigma^2 = 0.920$, the distribution is uni-modal and peak at $\psi_G^\ell \approx 0.6$. With the melting of the solid, the peak shifts to lower values but the uni-modal nature of the distribution does not change. This indicates that the transition is continuous.

time averaged density profiles in these blocks. Simultaneously, we overlapped the block-averaged local orientational order vector $(\mathrm{Re}(\psi_6^\ell), \mathrm{Im}(\psi_6^\ell))$ for a single configuration, on the spatially resolved density profile. A sequence of these plots is shown in Fig. 3.13. In the solid phase, the density is uniform throughout the system. The local orientational order vectors are perfectly aligned with each other, indicating a long-range orientational order. As the solids melts to a hexatic, we observe coexisting regions of high and low density along with high and low orientational bond order, respectively. Finally, once the hexatic melts to a liquid, the density is uniform throughout and the bond orientational order vectors are randomly oriented.

In addition to this, we also carried out the same procedure for the orientational order for a single configuration. The whole system was divided into a grid of size 10×10, with each sub-box dimension $L_x/10 \times L_y/10$. The local orientational order ψ_6^ℓ was computed from the local bond order ρ_6^i restricting the average over these sub-boxes. A heat-map of the spatially resolved orientational order was overlapped with its vector. A sequence of such plots are shown in Fig. 3.14. Once the solid melts, in the density range $0.910 < \rho\sigma^2 \leq 0.920$, there are isolated regions of low orientational order in the system. In contrast, between $0.904 \leq \rho\sigma^2 \leq 0.910$, we see coexisting regions with high and low values of hexatic order. These plots also gave us the typical size of these coexisting regions. Additionally, to ascertain a macrophase separation over time, we followed similar configurations over time, as shown in Fig. 3.15 for the density $\rho\sigma^2 = 0.998$. The plots clearly reveal that a macrophase separation indeed exists over time.

To get a more quantitative picture, we looked at the distribution of the block-averaged orientational order parameter, with block sizes smaller than the size of the coexisting phases. In the solid (liquid), we observe uni-modal distribution peaked at high (low) values of densities and orientational order, signifying that the system remains in a single phase. In contrast, in the hexatic phase, away from the solid-hexatic melting point, we see evidence of coexisting phases high and low orientational order, respectively. The probability distribution $\mathscr{P}(\psi_6^\ell)$ is shown in Fig. 3.17, along with the free-energy $\Delta F = -\ln \mathscr{P}(\psi_6^\ell)$. We observe a weak double minima in the free-energy and corresponding peaks in the distribution function. This coexistence is a characteristic of a first-order transition.

After a careful look at the orientational order parameter correlation and the spatially resolved density and orientational order, we come to the following conclusion. Once the solid melts to a hexatic phase at the density $\rho_m\sigma^2 = 0.920$, a significant amount of orientational order exists in the system up to a density of $\rho\sigma^2 \approx 0.906$. As the density is decreased further, the system does not immediately go to a liquid phase. Rather, some amount of orientational order is retained in the system. Only for densities $\rho\sigma^2 \leq 0.900$, the system goes into an isotropic liquid phase. Hence, although we identify $\rho\sigma^2 = 0.906$ as the melting of hexatic phase, in reality, this is merely the density up to which the hexatic phase is stable.

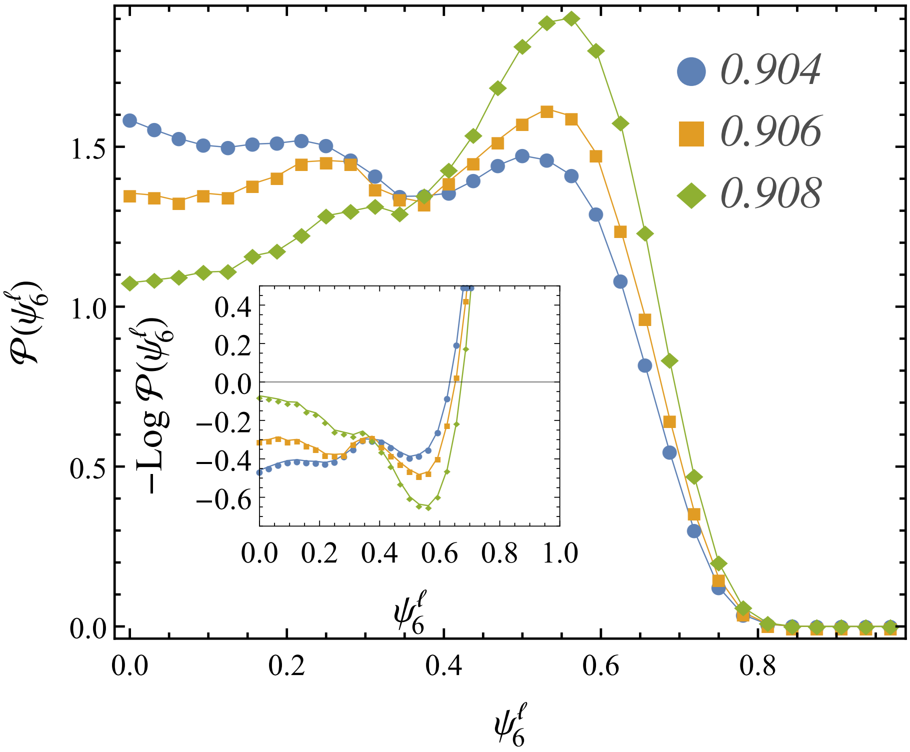

Figure 3.17 Distribution of the orientational order parameter ψ_6^ℓ in a sub-system of size $L_x/10 \times L_y/10$ for the system densities as indicated in the legend. The distribution shows weak double maxima at the boundary of the stable hexatic point $\rho\sigma^2 = 0.906$. The corresponding free-energy, defined as the negative logarithm of the probability distribution, is shown in the inset for the same three densities as in the main plot. A clear double minima, albeit very weak, appears in the free-energy.

3.6 Conclusion

In conclusion, we have presented a detailed analysis of the melting transition in a two dimensional colloidal suspension interacting via Weeks-Chandler-Anderson potential. We find that the melting is a two step process. At high densities, the system is in a triangular solid phase characterized by quasi-long ranged positional order and long ranged orientational order. As the density is decreased, the solid melts to a hexatic phase with a short ranged positional order and a quasi-long ranged orientational order. Upon further decreasing the density the hexatic melts to an isotropic liquid phase. The

Transition Densities	Kapfer *et. al.*[12]	Current Work
ρ_{hs}	$\rho\sigma^2 = 1.015$	$\rho\sigma^2 \approx 0.920$
ρ_{hex}	$\rho\sigma^2 = 1.005$	$\rho\sigma^2 \approx 0.906$
ρ_{liq}	$\rho\sigma^2 = 0.998$	$\rho\sigma^2 \approx 0.900$
Nature of Solid-Hexatic Transition	Continuous	Continuous
Nature of Hexatic-Liquid Transition	First-Order	First-Order

Table 3.1 Table comparing the solid-hexatic and the hexatic-liquid melting points and the nature of transition with the earlier works of Kapfer *et. al.*.[12]

two melting points are identified using the solid and orientational order parameter, their fluctuations and their correlations. The analysis of defect formation in the system shows that the solid-hexatic melting is a continuous transition that is mediated by the dissociation of quartets into dislocations, in agreement with KTHNY theory. Further, we also find that there is strong evidence of the hexatic-liquid transition being a first order transition. We summarise the melting points and compare it with the earlier work of Kapfer *et. al.* in the table below. The noticable difference in the transition points are due to the nature of the pair interaction potential, the WCA potential being much softer compared to the repulsive r^{-12} pair interaction.

Bibliography

[1] J. D. Weeks, D. Chandler and H. C. Andersen, *The Journal of Chemical Physics*, 1971, **54**, 5237–5247.

[2] R. Sadus, *Molecular Simulation of Fluids*, Elsevier Science, 2002.

[3] D. Frenkel and B. Smit, *Understanding molecular simulation: from algorithms to applications*, Academic press, NY, 2002.

[4] M. KrÃűger, *Physics Reports*, 2004, **390**, 453 – 551.

[5] J.-P. Hansen and L. Verlet, *Phys. Rev.*, 1969, **184**, 151–161.

[6] J.-P. Hansen, *Phys. Rev. A*, 1970, **2**, 221–230.

[7] D. M. Heyes and H. Okumura, *Molecular Simulation*, 2006, **32**, 45–50.

[8] A. Ahmed and R. J. Sadus, *Phys. Rev. E*, 2009, **80**, 061101.

[9] S. Toxværd, *Physical Review E*, 1993, **47**, 343.

[10] G. S. Grest and K. Kremer, *Phys. Rev. A*, 1986, **33**, 3628–3631.

[11] W. Mickel, S. C. Kapfer, G. E. Schröder-Turk and K. Mecke, *J. Chem. Phys.*, 2013, **138**, 044501.

[12] S. C. Kapfer and W. Krauth, *Physical Review Letters*, 2015, **114**, 035702–5.

4

Phase transition in a driven system

We consider a two dimensional colloidal dispersion of soft-core particles driven by a one dimensional stochastic flashing ratchet that induces a time averaged directed particle current through the system. It undergoes a non-equilibrium melting transition as the directed current approaches a maximum associated with a resonance of the ratcheting frequency with the relaxation frequency of the system. We use extensive molecular dynamics simulations to present a detailed phase diagram in the ratcheting rate- mean density plane. With the help of numerically calculated structure factor, solid and hexatic order parameters, and pair correlation functions, we show that the non-equilibrium melting is a continuous transition from a quasi-long ranged ordered solid to a hexatic phase. The transition is mediated by the unbinding of dislocations, and formation of compact and string-like defect clusters.

4.1 Introduction

A class of non-equilibrium driven systems called pump models are particularly intriguing due to their following property. They involve periodic forces, in time and space, that vanish under spatio-temporal averaging but still drives an overall directed current[1–10]. This is achieved via the breaking of time-reversal symmetry through, e.g., a phase lag between spatially non-local drives[5,7,8], or breaking of space inversion symmetry of the external potential profile[1–4]. Most of the biological processes generating directed motion involve reaction cycles and utilize some variant of this principle. Natural examples involve ion-pumps, e.g., the Na^+, K^+-ATPase pumps, and molecular motors[11], e.g., Kinesin or myosin moving on polymeric tracks of microtubules or F-actins, respectively[4]. The flashing ratchet model has been used to describe molecular motor locomotion[1]. In experiments on colloids, ratcheting could be generated using optical[12,13], magnetic[14,15] or electrical fields[16–18]. Most of the studies on pump models focused on systems of non-interacting particles, restricted to one dimension, with a few exceptions that analyzed the impact of interaction on molecular motors[19,20], collective properties of particle pumps[7–10,21], and in ratchet models[3,22–24].

In a recent study, we used an asymmetric periodic potential that switches between an *on* and *off* state in a stochastic manner to drive a directed current of particles in a two dimensional (2d) dispersion of sterically stabilized colloids[25], focusing on the frequency and density dependence of the ratcheted current. With the change in the rate of ratcheting, the time- averaged directed current carried by the colloids show a resonance with the system's relaxation frequency. The current shows a non-monotonic dependence on density as well. This change in the dynamical properties, as we show in this chapter, is closely related to the associated structural changes, e.g., the solid melts near the resonance frequency.

In the limit of extremely high switching frequency, higher than the inherent relaxation time of the colloids, the system can only respond to essentially a time- averaged potential profile. In addition, if one considers the limit of vanishing asymmetry in the potential profile, the scenario becomes equivalent to that of the re-entrant laser induced melting transition (RLIM)[26–29], in which a high- density colloidal liquid undergoes solidification followed by melting, as the strength of a commensurate external periodic potential is increased. This is an equilibrium phase transition of the Kosterlitz-Thouless type[28,29], and is described in terms of unbinding of a specific type of dislocations, allowed by the potential profile.

In this chapter, we consider an asymmetric ratcheting of soft-core particles, and investigate structural transitions associated with the change in dynamical behavior of the system, observed in terms of its current carrying capacity. Using a large scale molecular dynamics simulation, we obtain the phase diagram in the density- ratcheting rate plane, showing melting from a solid to hexatic phase. We find a re-entrant solid- hexatic- solid transition with changing ratcheting frequency. The transitions are associated with a non-monotonic variation of the mean directed current. The increase in current is related to solid melting. We discuss a connection between this melting and a plastic depinning phenomenon[30]. As we demonstrate in detail, the non-equilibrium melting is a continuous transition from a quasi- long ranged ordered (QLRO) solid to a hexatic phase, and is mediated by the formation of topological defects. The dominant defect types generated at the solid melting are dislocations, and compact or string-like defect clusters.

The rest of the chapter is organized in the following way. In Section 4.2 we present the model and details of the numerical simulations. The main results of the study describing the particle current, the different phases of the system, the nature of the transition between these phases, and associated defect formation are presented in Section 4.3. We finally conclude presenting a discussion and outlook in Section 4.4.

4.2 Model and Simulation Details

We consider a two dimensional system of a repulsively interacting colloidal suspension of N particles in a volume $A = L_x L_y$. The mean inter-particle separation in this system $a^2 = \sqrt{3}\rho/2$ is set by the particle density $\rho = N/A$. We assume that the colloids repel each other via a shifted soft-core potential $U(r) = \varepsilon\,[(\sigma/r)^{12} - 2^{-12}]$ when the inter-particle separation $r < r_c$ with $r_c = 2\sigma$, and $U(r) = 0$ otherwise. The units of energy and length scales are set by ε, σ respectively. The system evolves under an asymmetric ratchet potential $U_{\rm ext}(x,y,t) = V(t)\,[\sin(2\pi y/\lambda) + \alpha \sin(4\pi y/\lambda)]$, where the time-dependent strength $V(t)$ switches between ε and 0 stochastically with a rate f. The two sinusoidal terms in the above expression of $U_{\rm ext}$ with $\alpha = 0.2$ maintains the asymmetric shape of the potential profile. When it assumes a triangular lattice structure, the separation between consecutive lattice planes in the system is $a_y = \sqrt{3}a/2$. We have chosen the periodicity of the external potential $\lambda = a_y$, commensurate with the mean lattice spacing. In the absence of the external potential, the soft core solid is expected to undergo a two stage solid- hexatic- liquid transition[31–34], with the solid melting point at $\rho\sigma^2 \approx 1.01$. In the presence of a time- independent potential profile with $V(t) = U_0$ and $\alpha = 0$, the system undergoes RLIM with increase in U_0[27–29]. At

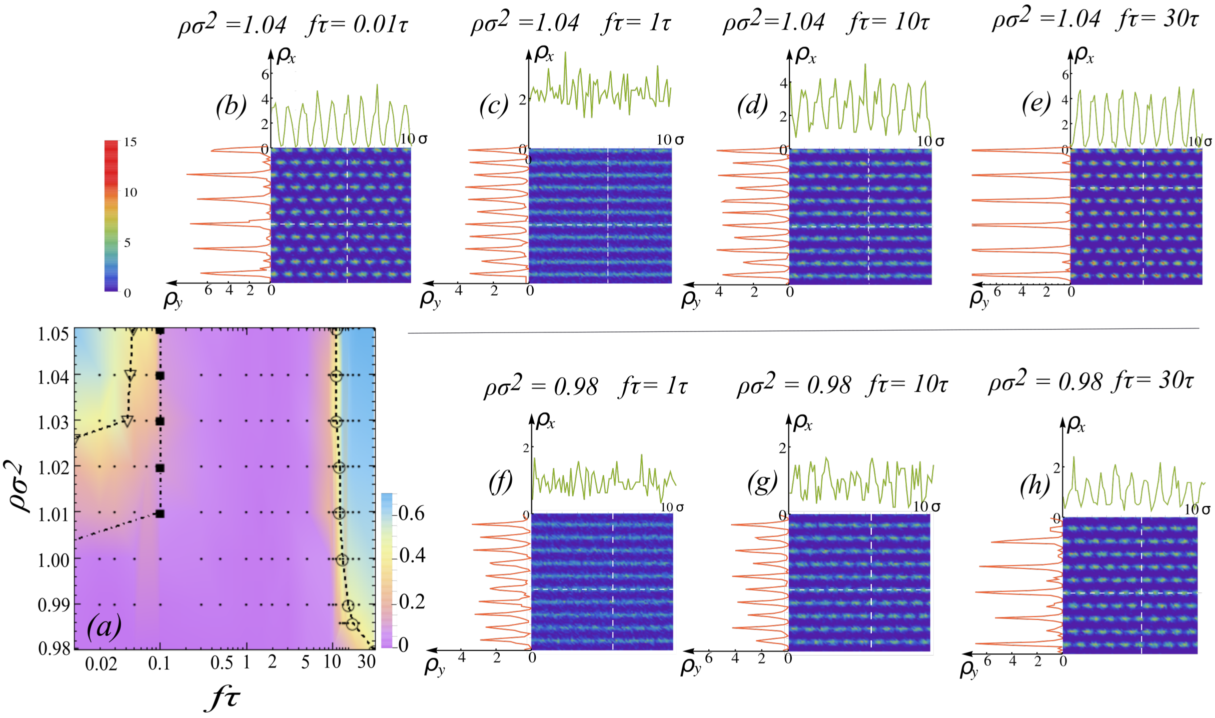

Figure 4.1 (a) Phase diagram in the density- frequency plane. The color code indicates the values of the solid order parameter $\langle \psi_{\mathbf{G}_2} \rangle$ of the stochastically ratcheted 2d colloidal suspension at different density and ratcheting frequency. Sky-blue denotes high solid order. The dashed lines through open symbols ($\triangledown$, $\circ$) show the boundaries of instability of the solid phase. The dash-dotted line through ■ indicates the low driving frequency f_s below which the system can relax to instantaneous external potential profile. In the opposite limit of high frequencies, the system feels a time- integrated constant confinement analogous to a laser induced freezing and consequently exhibits a high value of the order parameter. In the regime of intermediate frequencies, the long range order is broken due to the particle current. (b)-(h) Plots of time-averaged local density profiles $\rho(x,y)$ over a section of $10\sigma \times 10\sigma$ area, at different densities and frequencies as indicated in the figures. Their cuts ρ_y measured along the vertical white dashed lines, and ρ_x measured along the horizontal dashed lines are shown in the out-ward projected ordinate and abscissa, respectively.

$U_0 = \varepsilon$, the laser induced melting point of the soft-core solid is $\rho\sigma^2 = 0.95$[29].

We perform molecular dynamics simulations of the system, with periodic boundary conditions, in the presence of an external ratcheting potential using the standard leap-frog algorithm[35] with a time-step $\delta t = 0.001\,\tau$ where $\tau = \sigma\sqrt{m/\varepsilon}$ is the characteristic time scale. We use $m = 1$. The temperature of the system is kept constant at $T = 1.0\varepsilon/k_\mathrm{B}$ using a Langevin thermostat characterized by an isotropic friction $\gamma = 1/\tau$. At each step a trial move is performed to switch $V(t)$ between 0 and ε, and accepted with a probability $f\,\delta t$. In this current work, we present the results for a large system of $N = 262144$ particles. We discard simulations over initial 10^7 steps to ensure achievement of steady state, and the analyses are performed collecting data over further 10^7 steps.

4.3 Results and Discussion

In this section we present the main results of our study. We begin our discussion with a presentation of the non-equilibrium phase diagram in the ratcheting frequency- system density plane, along with a description of the local structures at various phases (Section 4.3.1). We find a re-entrant melting as a function of the ratcheting frequency. The structural transition is concomitant of enhancement of the driven particle flux. We show in Section 4.3.2, the re-entrant melting is associated with a non-monotonic variation of the ratcheting current with respect to the driving frequency. More detailed characterization of the melting transition is outlined in the rest of the section. In Section 4.3.3 we demonstrate the melting transition showing the variation of the solid and hexatic order parameters. Using their distribution functions in Section 4.3.4 we establish the continuous nature of the melting. In Section 4.3.5 we show that the pair correlation function changes from a power-law nature characterising the quasi- long range ordered solid phase to exponential decay at melting. Finally, the formation of different types of topological defects in the system are analyzed in Section 4.3.6.

4.3.1 Phase diagram

In Fig. 4.1 we present the detailed phase diagram along with local density profiles of the 2D system of mono-dispersed ratcheted colloids. The system displays a solid and a density modulated hexatic phase, controlled by the dimensionless density $\rho\sigma^2$ and ratcheting rate $f\tau$. The color codes in Fig. 4.1(a) denote the values of mean solid order parameter $\langle \psi_{\mathbf{G}_2} \rangle = (1/N) \langle \sum_{i=1}^{N} \sum_{j=1}^{N} e^{-\mathrm{i}\mathbf{G}_2 \cdot (\mathbf{r_i} - \mathbf{r_j})} \rangle$ where $\mathbf{G}_2 = (\pm 2\pi/a, \pm\pi/a_y)$ that captures the translational order in the system. The two dashed lines with open symbols signify the two solid melting boundaries at small and high frequencies. The dash-dotted line with filled squares denotes the inverse of relaxation time-scales f_s of the system at a given density. For ratcheting rates slower than this time-scale, the solid and hexatic order can *equilibrate* to the instantaneous external potential and follow its change. The details of the calculation of such relaxation times are discussed later.

As is shown in Fig. 4.1(a), the system remains in a QLRO triangular lattice solid phase at the highest frequencies, if the ambient density permits. As the frequency decreases, the solid melts into a hexatic phase, below the dashed line through open circles (Fig. 4.1). As the frequency of the drive is decreased further, below the equilibrium relaxation time, the system starts to follow the time variation of the external potential. As a result, the time-averaged properties turn out to be approximately a superposition of

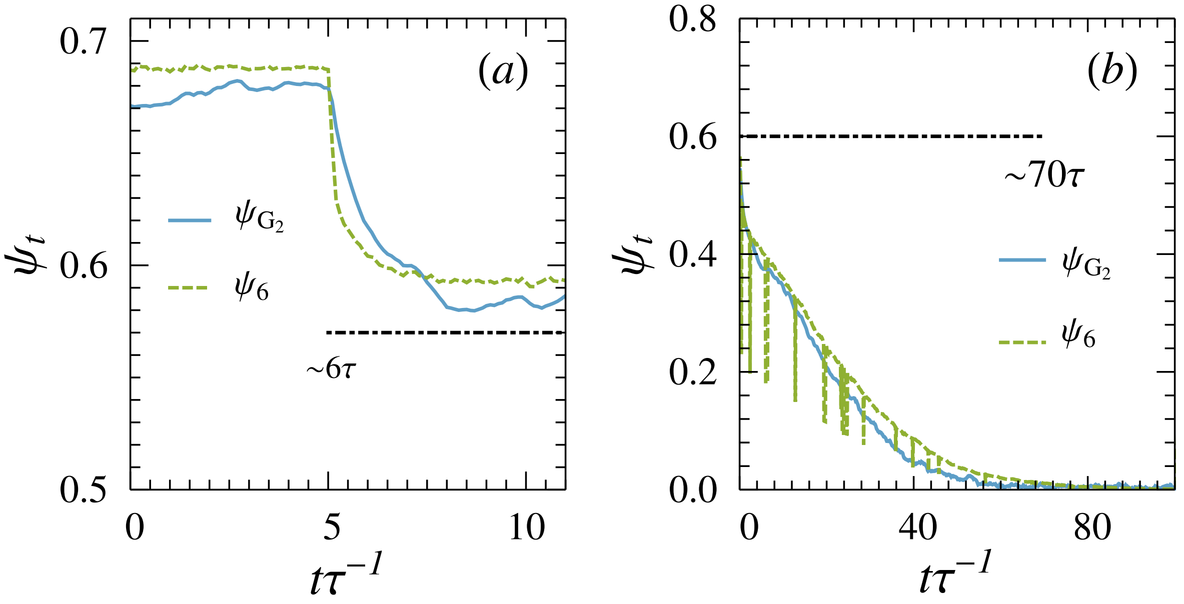

Figure 4.2 Relaxation dynamics of the solid and hexatic order parameters at $\rho\sigma^2 = 1.04\,(a)$ and $\rho\sigma^2 = 0.98\,(b)$, respectively. The time scales for relaxation are $f_s^{-1} \approx 6\,\tau\,(a)$ and $f_s^{-1} \approx 70\,\tau\,(b)$.

the properties of the equilibrium states in the presence ($V(t) = \varepsilon$) and absence ($V(t) = 0$) of external potential profile. At high densities ($\rho\sigma^2 \gtrsim 1.026$) the solid phase is stabilized even at low ratcheting frequencies like $f\tau = 0.01$.

Here we momentarily digress to provide the details of the equilibrium relaxation times of the order parameters. This time-scale at different densities are determined from separate simulations. The initial equilibration is performed under a time-independent external potential of the form given in Section 4.2 with $V(t) = \varepsilon$ over 10^7 simulation steps. Thereafter, the external potential is removed and the evolution of the solid and the hexatic order parameters are measured over time. In Fig. 4.2 we show the results for the relaxation time-scales of the solid and the hexatic order parameters at densities $\rho\sigma^2 = 1.04$ (figure a) and 0.98 (figure b), after withdrawing an external potential commensurate with the system density under which the system is initially equilibrated At densities higher than the equilibrium melting point $\rho_m\sigma^2 \approx 1.01$, the solid and the hexatic order parameters, ψ_{G_2} and ψ_6, decay to finite values, indicating order even in the absence of external potential (Fig. 4.2(a)). In contrast, at densities $\rho < \rho_m$, the solid and the hexatic order parameters vanish with time (Fig. 4.2(b)). The time-scale of such decay, indicated in Fig. 4.2, gives the estimate of the relevant relaxation time. If a time-independent external potential switches with a rate slower than this time-scale, the system will have enough time to *equilibrate* to instantaneous potential profiles. The relaxation frequency f_s is inverse of this time-scale, and has been indicated by the dash-dotted line through ■ symbols in the phase diagram Fig. 4.1.

In Fig. 4.1(b)-(h) we present the time-averaged local density profiles $\rho(x,y)$, at two mean densities $\rho\sigma^2 = 1.04, 0.98$. We show the results over local cross- sections of area $10\sigma \times 10\sigma$, for better visibility. Corresponding to $\rho\sigma^2 = 1.04$, the density profile shows triangular lattice structure at $f\tau = 0.01$ (Fig. 4.1(b)). At $f\tau = 1$ the solid melts into a phase with density modulation along y-axis, the direction of ratcheting drive (Fig. 4.1(c)). As the frequency is further increased to $f\tau = 10$, a local triangular lattice- like pattern starts to reappear (Fig. 4.1(d)), and the system shows a more compact triangular lattice structure at $f\tau = 30$ (Fig. 4.1(e)). Thus with increasing $f\tau$ the system shows a re-entrant transition from solid to density modulated to solid phase.

Similar characterization at a lower density $\rho\sigma^2 = 0.98$ is presented in Fig. 4.1(f)-(h). In this case, a triangular lattice order is only observed at the highest ratcheting frequency $f\tau = 30$ (Fig. 4.1(h)). At lower frequencies, this pattern gets smeared (Fig. 4.1(g) and (f)). Note that the densities considered here are relatively large with respect to the equilibrium laser induced melting point $\rho\sigma^2 \approx 0.95$, for a constant $V(t) = \varepsilon$.

The local structure is further quantified in terms of the cuts of density profile $\rho_x(x) \equiv \rho(x,y_0)$ and $\rho_y(y) \equiv \rho(x_0,y)$, at fixed $y_0 = 5a_y$ and $x_0 = 6a$ as indicated by the two perpendicular white dashed lines in each $\rho(x,y)$ plot in Fig. 4.1(b)-(h). These profiles $\rho_x(x)$ and $\rho_y(y)$ are shown along the top and left axes around the $\rho(x,y)$ plots. The clean density modulations in $\rho_x(x)$ along the $y_0 = 5a_y$ line captures the spontaneous solid- like order in that direction. Note that the position of the peaks would shift by $a/2$ keeping the periodicity same, if one considers $\rho_x(x)$ along a neighboring lattice plane at $y_0 \pm a_y$ instead. Due to the shape of the triangular lattice solid, the density cut $\rho_y(y)$ along the vertical line at $x_0 = 6a$ shows density modulations with larger peaks appearing at every alternate lattice lines with a periodicity $2a_y$ (see Fig. 4.1(b) and (e)). After the solid melts, the system gets into a density modulated phase characterized by equal heights of $\rho_y(y)$ peaks with a reduced periodicity a_y (e.g., see Fig. 4.1(c) and (f)).

4.3.2 Directed particle current and order

The inherent asymmetry of the ratchet potential, added with the stochastic switching drives a time- and space- averaged directed particle current in the system,

$$\langle j_y \rangle = \frac{1}{\tau_m}\frac{1}{A}\int^{\tau_m} dt \int^{L_x} dx \int^{L_y} dy \; j_y(x,y,t), \tag{4.1}$$

where, τ_m is an integral multiple of $1/f$, the mean switching time of the flashing ratchet potential. The flashing ratchet leads to an effective potential which is periodic and spa-

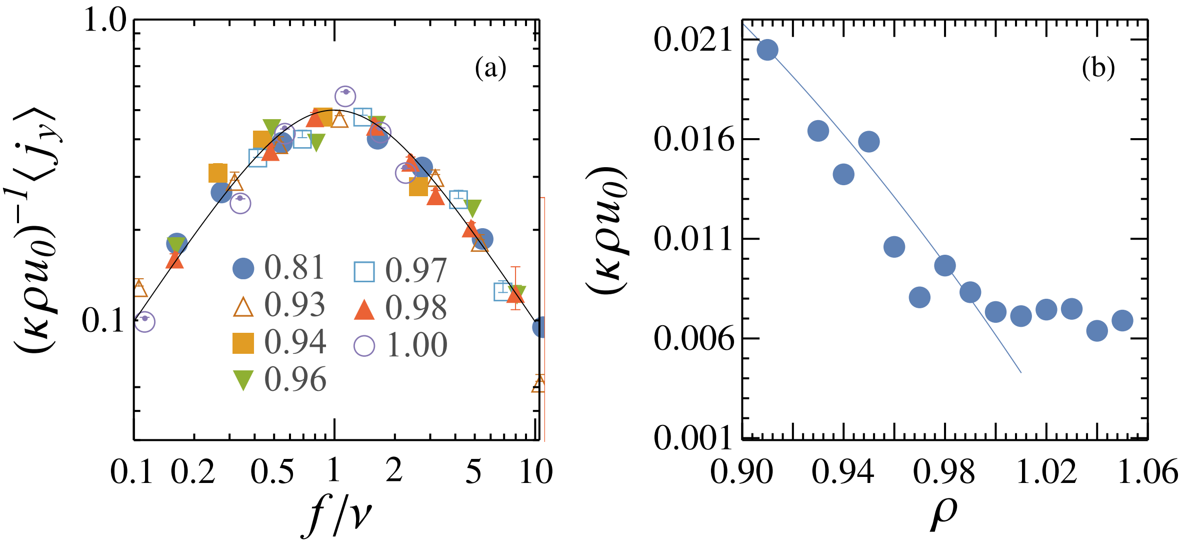

Figure 4.3 (color online) (a) Variation of the scaled particle current $(\kappa\rho u_0)^{-1}\langle j_y\rangle$ along the direction of the drive as a function f/ν for different densities as indicated in the legend. The solid line is plot of the function $(f/\nu)/\left(1+(f/\nu)^2\right)$ as given by Eq. (4.2). (b) Plot of the current amplitude $\rho\kappa u_0$ as a function of density. The solid line is a fit to the data using the functional form $\kappa D_0\rho^{3/2}(1-\rho/\rho_c)$ with κD_0 and ρ_c as fitting parameters with values $\kappa D_0 \approx 0.22$ and $\rho_c\sigma^2 \approx 1.004$.

tially tilted, with the tilt changing with the ratcheting frequency non-monotonically[36].

At low frequencies the particle current increases linearly with the driving frequency f, achieves a maximum around $f = \nu$ with ν being the intrinsic relaxation frequency, and beyond this decays as f^{-1}. The behaviour of the current in the whole frequency range can be captured by the simple ansatz[25]

$$\langle j_y\rangle = \kappa \frac{\nu f}{\nu^2 + f^2}\rho u_0, \tag{4.2}$$

where, $u_0 = \nu\lambda$ intrinsic velocity, and κ is a proportionality constant.

In the high density regime, where, the mean-free path of the particles is small, the diffusive time scale τ_D to travel the length scale of the potential periodicity λ is set by $\tau_D = \lambda^2/D(\rho)$. Here $D(\rho)$ denotes the density- dependent tagged particle diffusivity, which decreases linearly with density, $D(\rho) = D_0(1-\rho/\rho_c)$[25], with $D_0 = k_B T/\gamma$ is the bare diffusivity. The commensurate external potential ensures that $\lambda^2 \sim 1/\rho$, and consequently the intrinsic relaxation frequency takes the form $\nu = \rho D(\rho)$. The maximum of the current appears when ratcheting frequency f becomes equal to ν. The intrinsic velocity scale is set by $u_0 = \lambda/\tau_D = \rho^{1/2}D(\rho)$. Substituting for u_0 and ν in Eq. (4.2), the

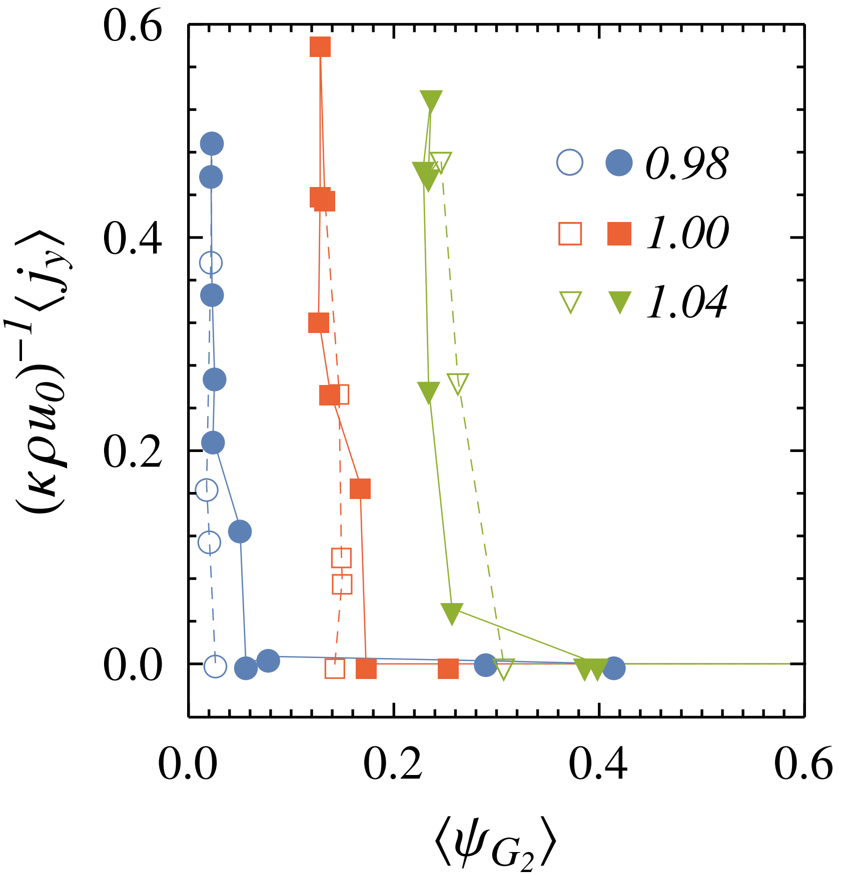

Figure 4.4 Parametric plot of the scaled particle current $(\kappa\rho u_0)^{-1}\langle j_y\rangle$ and the solid order parameter $\langle\psi_{G_2}$ with changing frequency $f\tau$ is shown for three densities as indicated in the legend. The open (filled) symbols represent the increase (decrease) of current with frequency. For better visibility, plots at $\rho\sigma^2 = 1.00$ and 1.04 are shifted along the $\langle\psi_{G_2}\rangle$ axis by 0.1 and 0.2, respectively.

density and frequency dependent current takes the form

$$\langle j_y\rangle = \frac{fD_0^2}{D_0^2\rho^2(1-\rho/\rho_c)^2+f^2}\rho^{5/2}(1-\rho/\rho_c)^2. \tag{4.3}$$

The resonance in the particle current appears at the ratcheting rate $f = \nu = D_0\rho(1-\rho/\rho_c)$ and the density dependent amplitude take the form $\kappa\rho u_0 = \kappa D_0\rho^{3/2}(1-\rho/\rho_c)$.

Fig. 4.3(a) shows data collapse of particle currents when plotted as $(\kappa\rho u_0)^{-1}\langle j_y\rangle$ against the dimensionless variable f/ν. The current maximizes at the resonance frequency of $f = \nu$. Fig. 4.3(b) shows the limit of validity of the approximate form $u_0 = D_0\rho^{1/2}(1-\rho/\rho_c)$. A comparison of Fig. 4.1 and Fig. 4.3a shows the relationship between the structure and dynamics. For example, at the resonance frequency, the system melts in order to carry the largest directed current.

Clearly the amount of translational order of the system is directly related to the amount of driven current. Fig. 4.4 shows explicitly the variation of the solid order $\langle \psi_{\mathbf{G}_2} \rangle$ with the driven current $\langle j_y \rangle$, at three system densities $\rho\sigma^2 = 0.98, 1.00, 1.04$. In each case, the translational order drops with the increase in driven current. The reentrance as a function of frequency, shows a monotonic behavior when the transition is viewed with respect to the driven current. The low current supports a translationally ordered state (at both low and high frequencies), whereas a high drift current produces a disordering transition (intermediate frequencies).

In this context, let us reconsider the picture of effective tilted potential generated due to the flashing ratchet[36]. While the spatial periodicity of the effective potential, depending on the potential- depth with respect to the thermal noise, may produce particle pinning, the tilt in this potential tries to drive a directed particle current. The onset of this current with increasing tilt can then be viewed as a depinning phenomenon (e.g., see Ref. [30] and citations therein). The depinning current and associated structural transitions of a pinned solid under directed external force have been studied in various contexts[30,37–39].

In Fig. 4.5 we follow the trajectories of neighboring particles in the initial configurations. As can be clearly seen from Fig. 4.5(a) and (c), the trajectories of nearest neighbors remain localized at both high and low ratcheting frequencies, corresponding to small current. These trajectories in Fig. 4.5(a) and (c) correspond to the solid phase, and can be interpreted as a pinned state. On the other hand, in the current carrying state at the intermediate frequency $f\tau = 1.0$, the neighbouring trajectories get extended, mostly along the y- direction, the direction of driven current $\langle j_y \rangle$. These extended trajectories correspond to a depinning phenomenon. A question remains whether after depinning the trajectories move together as in an elastic depinning, or separate out as in a plastic depinning. To demonstrate that, in Fig. 4.5(d) we show the mean squared fluctuations of the relative displacements $\langle (\mathbf{u}_i - \mathbf{u}_j)^2 \rangle$ of nearest neighbor pairs i, j corresponding to the initial configuration. In the low and high frequency limits of small $\langle j_y \rangle$, the relative displacement stays unchanged over appreciable intervals before jumping in steps, suggesting particle hopping between neighboring lattice sites, maintaining the solid order. On the other hand, in the current carrying phase at $f\tau = 1.0$, the relative displacement fluctuations grow diffusively with time, suggesting a plastic depinning that eventually melts the solid. At low densities, e.g., $\rho\sigma^2 = 0.98$, the trajectories get localized (pinned) only at the highest ratcheting frequencies (see Fig. 4.6).

In Fig. 4.7, we further analyze the local dynamics in terms of the mean squared displacements observed for individual particles. Let us consider the system at $\rho\sigma^2 =$

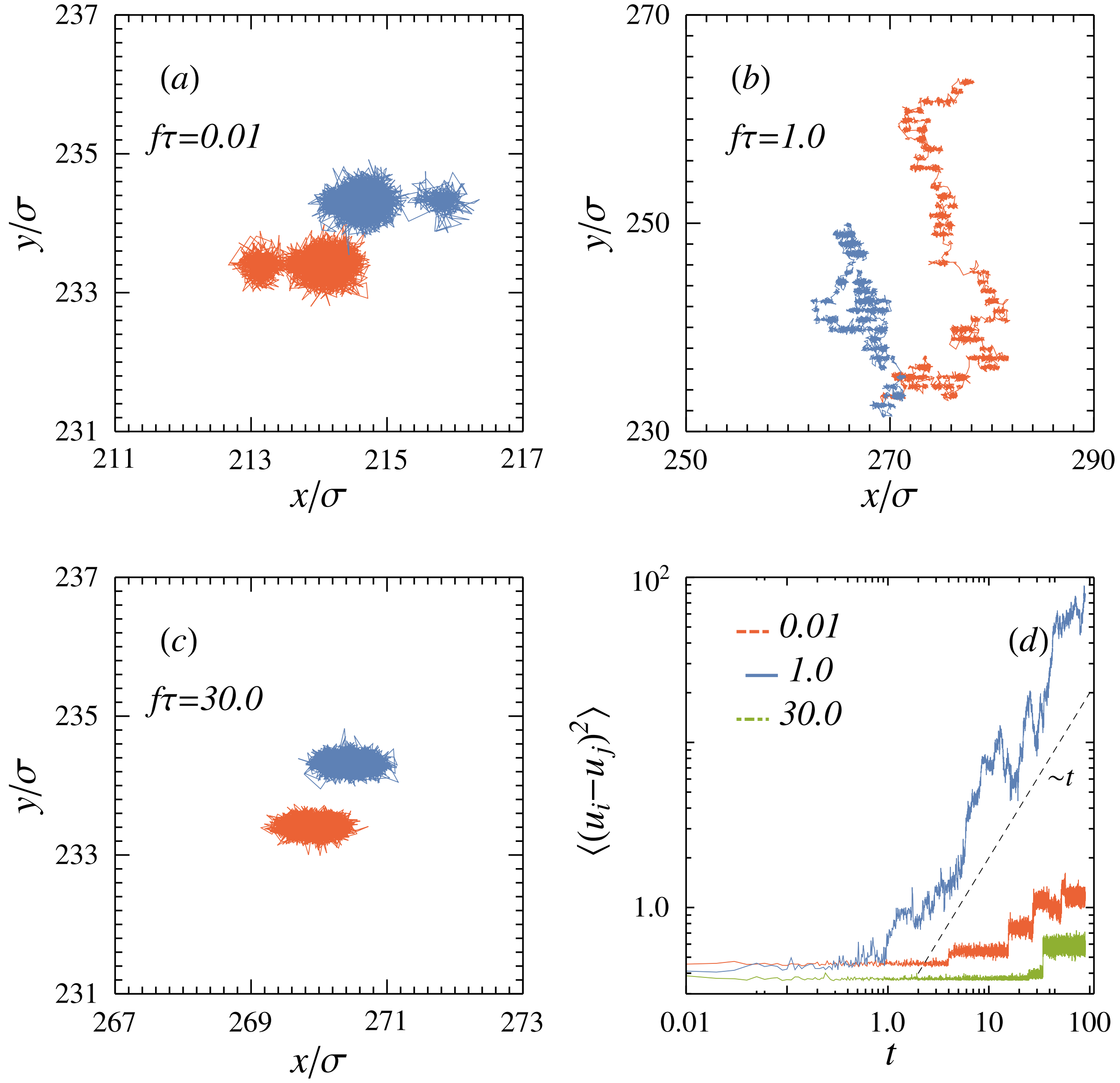

Figure 4.5 (color online) Typical trajectories of neighboring particles are shown for three frequencies $f\tau = 0.01$ (a), 1.0 (b) and 30.0 (c) for a system at a density of $\rho\sigma^2 = 1.04$. At low driving frequencies, even though the trajectories are localized, we observe hopping between neighboring lattice points along the x-direction (a). In contrast, at high driving frequencies the trajectories are more strongly localized (c). At intermediate frequencies that drives higher directed current through the system, the trajectories are extended along the direction of the drive (b). In (d) we plot the relative mean-square displacement $\langle(\mathbf{u}_i - \mathbf{u}_j)^2\rangle$ of nearest- neighbour pairs corresponding to initial configuration. We plot the results for the three ratcheting frequencies. The results are averaged over 10 pairs of trajectories. We observe that in the current carrying regime, $f\tau = 1.0$, the relative displacement fluctuations diverge in a diffusive manner.

1.04. Both the components of the displacement fluctuations in Fig. 4.7 show an initial ballistic part $\sim t^2$ due to the inertial nature of the dynamics. In the low $\langle j_y \rangle$ limits of low and high frequencies, this crosses over to a sub-diffusive behavior ($\sim t^{\nu}$ with $\nu < 1$). The test particles show localized motion within cages formed by neighbours

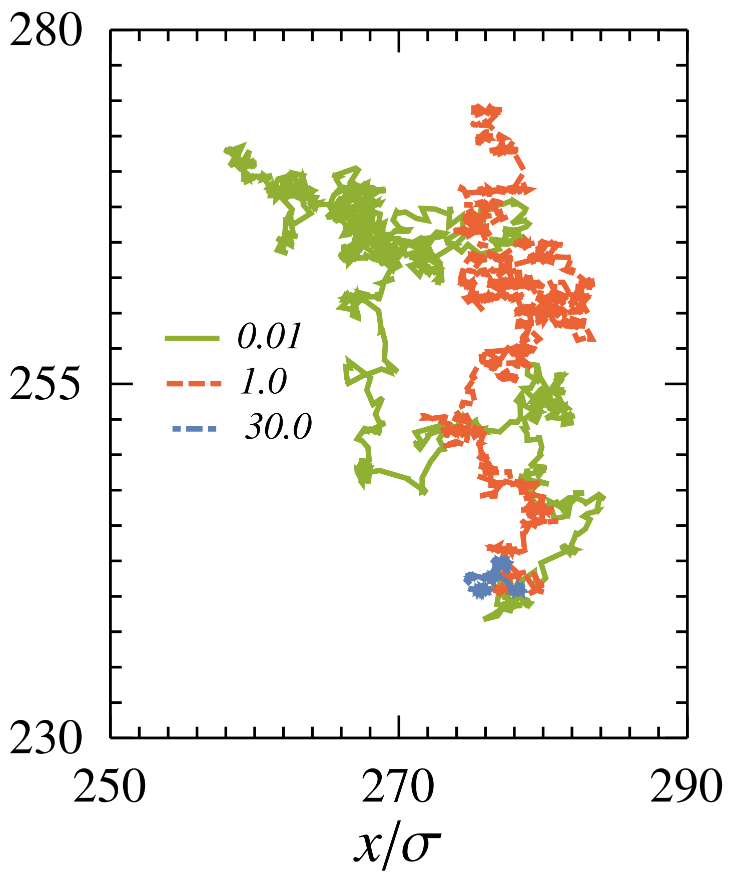

Figure 4.6 (color online) Typical trajectories of particles at densities $\rho\sigma^2 = 0.98$ are shown for three different frequencies $f\tau = 0.01$, 1 and 30. At high frequencies the particles get localized, whereas at very low frequencies localization happens only at densities above ρ_c. In the intermediate frequencies, at both densities the trajectories span a length scale of $\approx 20\,\sigma - 30\,\sigma$.

(see Fig. 4.5(a) and (c)). At $f\tau = 1$ corresponding to high $\langle j_y \rangle$, we find a long time diffusive behavior in x- direction, $\langle \Delta x^2 \rangle \sim t$, and almost ballistic motion in y, $\langle \Delta y^2 \rangle \sim t^{\nu}$ with $1 < \nu \lesssim 2$ (Fig. 4.7). The corresponding particle trajectories display long excursions in the y-direction, as is shown in Fig. 4.5(b).

4.3.3 Non-equilibrium melting

For a more quantitative analysis, we turn our attention to the phase diagram Fig. 4.1(a) and consider the phase behavior along constant frequency, and constant density lines. The structure factor, $\langle \psi_{\mathbf{q}} \rangle = (1/N)\,\langle \rho_{\mathbf{q}}\,\rho_{-\mathbf{q}} \rangle$ (see Fig. 4.8) with $\rho_{\mathbf{q}} = \sum_{j=1}^{N} e^{-\mathrm{i}\mathbf{q}\cdot\mathbf{r_j}}$ and $\rho^*_{\mathbf{q}} = \rho_{-\mathbf{q}}$, can clearly distinguish between a solid, hexatic, liquid and a modulated liquid phase[40]. In the solid phase $\langle \psi_{\mathbf{q}} \rangle$ shows a characteristic six fold symmetry with peaks at $\mathbf{G}_1 = (0, \pm 2\pi/a_y)$ and $\mathbf{G}_2 = (\pm 2\pi/a, \pm\pi/a_y)$ reflecting the underlying triangular lattice structure (see Fig. 4.8(a),(c),(f)). The six intensity maxima broaden along the constant

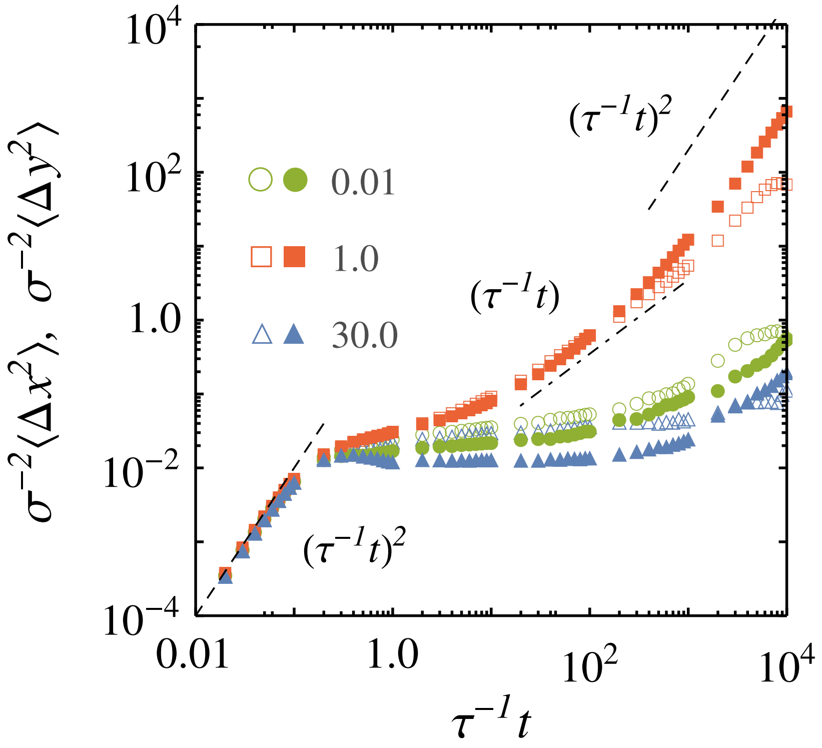

Figure 4.7 (color online) Plot of the mean-square displacement at density $\rho\sigma^2 = 1.04$ for frequencies $f\tau = 0.01$ (green), 1.0 (red) and 30.0 (blue). The displacements in $\langle\Delta x^2\rangle$ are shown with open symbols and that in $\langle\Delta y^2\rangle$ are represented with filled symbols.

---

radius $q = 2\pi/a$ circle in a hexatic (Fig. 4.8(b),(e)). In a simple liquid with spherical symmetry, the broadening extends to overlap forming a characteristic ring structure. On the other hand, in a modulated liquid phase, $\langle\psi_{\mathbf{q}}\rangle$ is expected to show two bright spots at $\mathbf{G}_1$, in addition to the ring structure characterizing a simple liquid (see Fig. 4.8(b),(e)). Note that the presence of the external periodic potential in the present context induces an explicit symmetry breaking by imposing density modulations in y-direction, ensuring $\langle\psi_{\mathbf{G}_1}\rangle > \langle\psi_{\mathbf{G}_2}\rangle$. The other four quasi Bragg peaks at $\mathbf{G}_2$, e.g., at the highest ratcheting frequencies, identify the appearance of the quasi long ranged positional order (QLRO). We used their arithmetic mean as the measure of solid order parameter $\langle\psi_{\mathbf{G}_2}\rangle$.

The QLRO in the solid phase is explicitly demonstrated using the system size dependence of $\langle\psi_{\mathbf{G}_2}\rangle$ shown in Fig. 4.9. The calculations are performed over sub-blocks of sizes $\ell_x \times \ell_y = \ell^2$. Within both the high and low frequency solid regions, $\langle\psi_{\mathbf{G}_2}(\ell)\rangle \sim \ell^{-\nu}$ where $\nu < 1/3$, the value of the exponent expected at the equilibrium KTHNY (Kosterlitz- Thouless- Halperin- Nelson- Young) melting[31–33]. In this case, the value of the exponent ν depends on the mean density and ratcheting frequency.

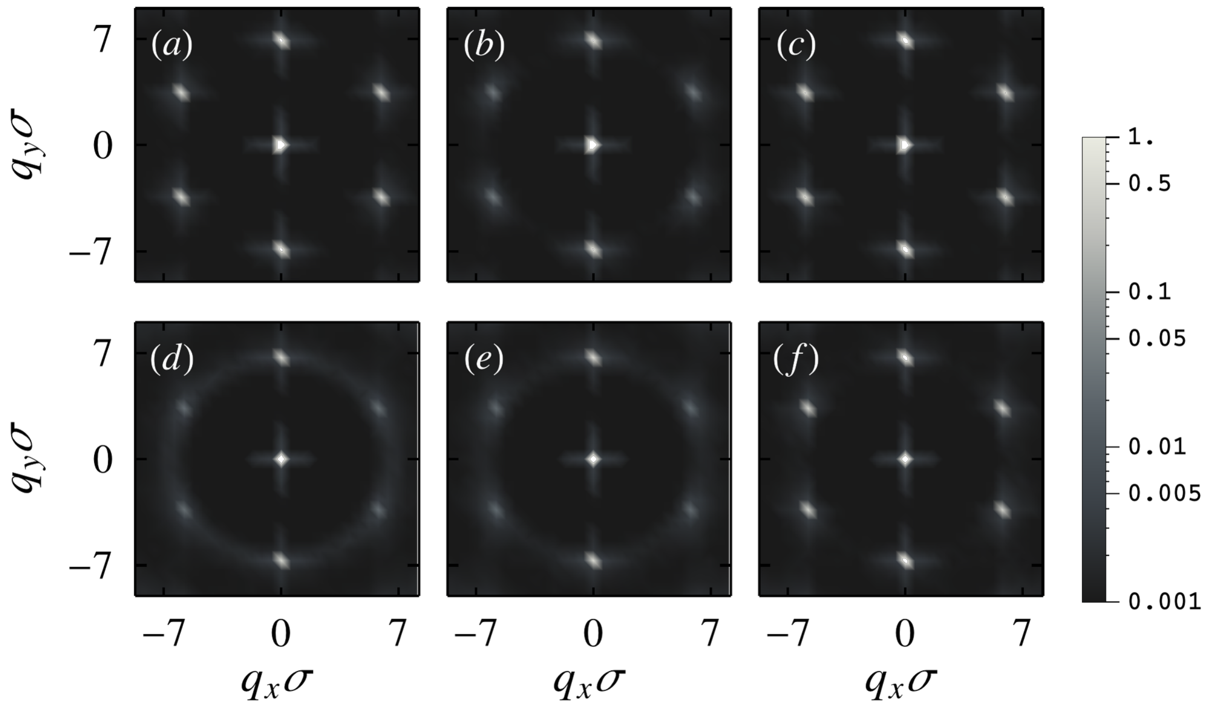

Figure 4.8 Plots of the static structure factor $\langle\psi_{\mathbf{q}}\rangle$ for the densities $\rho\sigma^2 = 1.04$ (a-c) and 0.98 (figures d-f). The three columns correspond to three different frequencies $f\tau = 0.01$ (a and d), 1.00 (b and e) and 30 (c and f).

The phase behaviors can be further characterized by following the change in the hexatic bond orientational order $\langle\psi_6\rangle = (1/N)\langle|\sum_{i=1}^{N} \psi_6^i|^2\rangle$, where we define the local hexatic order $\psi_6^i = \sum_{k=1}^{n_v}(\ell_k/\ell)\exp(\mathrm{i}6\phi_{ik})$ utilizing the n_v Voronoi neighbors of the i-th test particle. Here ϕ_{ik} is the angle subtended by the bond between the i-th particle and its k-th Voronoi neighbor. In this definition we used the weighted average over the weight factor ℓ_k/ℓ such that $\ell = \sum_{k=1}^{n_v}\ell_k$ and ℓ_k denotes the length of the Voronoi edge corresponding to the k-th topological neighbor[41].

In Fig. 4.10(a) and (b) we show the variations of the solid and hexatic orders, $\langle\psi_{\mathbf{G}_2}\rangle$ and $\langle\psi_6\rangle$, as a function of the ratcheting frequency keeping the density of the system fixed. Both the order parameters show non-monotonic variation with frequency. The large variation of the solid order parameter $\langle\psi_{\mathbf{G}_2}\rangle$ with $f\tau$ signifies melting, followed by a *re-entrant solidification*. Here we use the value of the solid order parameter at the equilibrium melting point, $\langle\psi_{\mathbf{G}_2}^m\rangle \approx 0.376$ (Fig. 4.11), to identify the boundary of solid phase, $\langle\psi_{\mathbf{G}_2}\rangle \geq \langle\psi_{\mathbf{G}_2}^m\rangle$. The small variation of $\langle\psi_6\rangle$ in Fig. 4.10(b) demonstrate maintenance of the hexatic order at different frequencies.

Fig. 4.10(c) and (d) show variation of the two order parameters as a function of the density, keeping the driving frequency fixed. Fig. 4.10(c) shows that the solid order parameter $\langle\psi_{\mathbf{G}_2}\rangle$ does not depend appreciably on the mean density $\rho\sigma^2$, unless at the

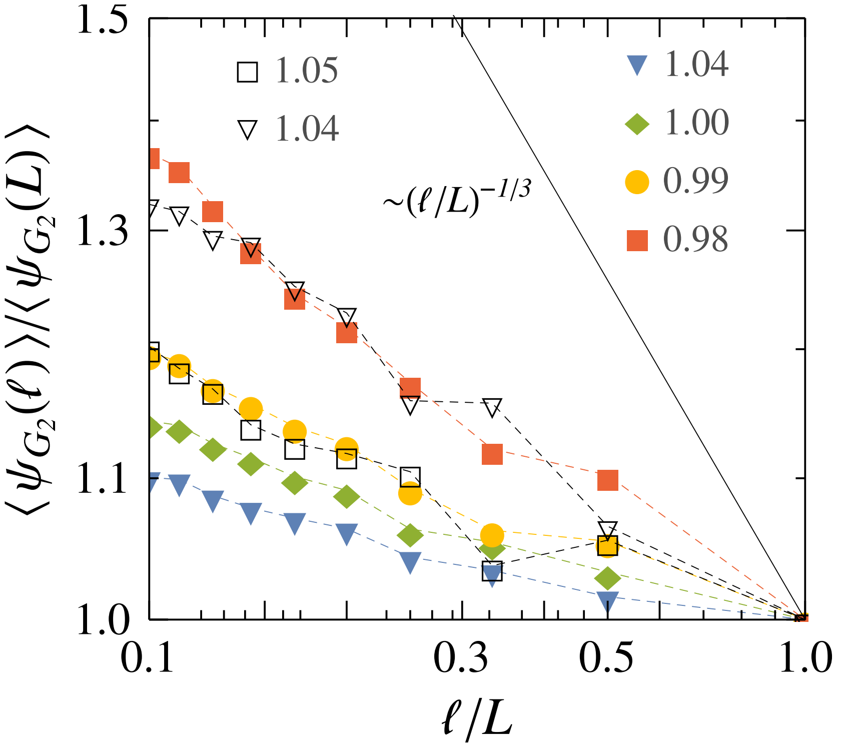

Figure 4.9 System size dependence of the solid order parameter. The ratio of mean order parameter measured over blocks of size $\ell = (\ell_x \times \ell_y)^{1/2}$ with respect to that measured over the whole system, $\langle \psi_{\mathbf{G}_2}(\ell) \rangle / \langle \psi_{\mathbf{G}_2}(L) \rangle$ decays with ℓ/L with power law $(\ell/L)^{-\nu}$. The data is shown for different densities as indicated in the legend. The solid and open symbols denote results at frequency $f\tau = 30$ and $f\tau = 0.01$, respectively. The solid black line is a plot of the power-law $(\ell/L)^{-1/3}$ expected at the equilibrium KTHNY melting point.

smallest driving frequencies. At such low frequencies, the system has enough time to equilibrate to the instantaneous potential profile, and the solid order shows appreciable increase with density as in equilibrium. Similar non-linear variations are observed for $\langle \psi_6 \rangle$, although, with smaller amplitude (Fig. 4.10(d)). At driving frequencies much larger than the inverse relaxation times, the system responds to only a time-averaged potential profile. The corresponding behavior as a function of density is similar to that in the presence of a time-independent commensurate potential (see Fig. 4.11).

Within a QLRO solid, the hexatic order is expected to remain long ranged. As the solid melts to a hexatic phase one expects a QLRO in the hexatic order parameter. In Fig. 4.12 we show the system- size dependence of $\langle \psi_6(\ell) \rangle$ at $\rho\sigma^2 = 1.04$. In the solid phase, corresponding to both the small and high frequencies, the hexatic order remains relatively high (see the inset in Fig. 4.12) and shows extremely weak decay over a length scale of $0.2L$, followed by saturation. The value of $\langle \psi_6(\ell) \rangle$ is appreciably smaller (< 0.4) at the intermediate frequency $f\tau = 1.0$, but shows a weak power-law like decay $\langle \psi_6(\ell) \rangle \sim \ell^{-\mu}$, with an extremely small value of the exponent μ. This hexatic order is

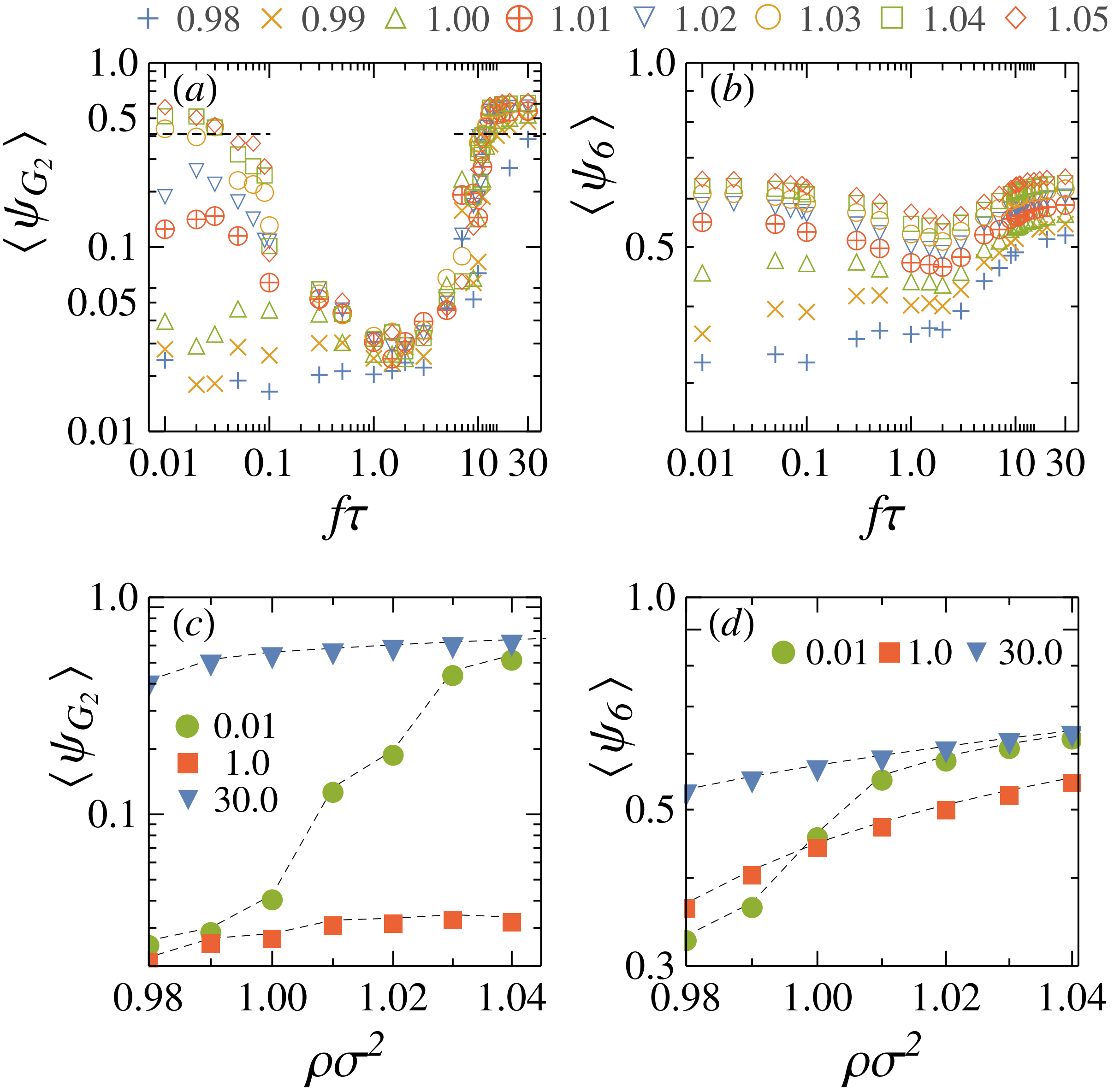

Figure 4.10 Dependence of the (a) solid order parameter $\langle \psi_{G_2} \rangle$ and (b) hexatic order parameter $\langle \psi_6 \rangle$ as a function of frequency is plotted for different densities as indicated in the legend on the top. The equilibrium melting point $\langle \psi^m_{G_2} \rangle = 0.376$ is denoted by the dashed lines in (a). The variations of (c) $\langle \psi_{G_2} \rangle$ and (d) $\langle \psi_6 \rangle$ are shown as a function of the mean density for three driving frequencies $f\tau = 0.01$, 1 and 30 as indicated in the legends.

---

maintained, even after the melting of the solid at intermediate frequencies. This is due to the external periodic potential.

4.3.4 Continuous transition: Distribution of order parameters

We probe the order of the phase transitions using the distribution of the local solid and hexatic order parameters. In determining the local solid order, we divided the simula-

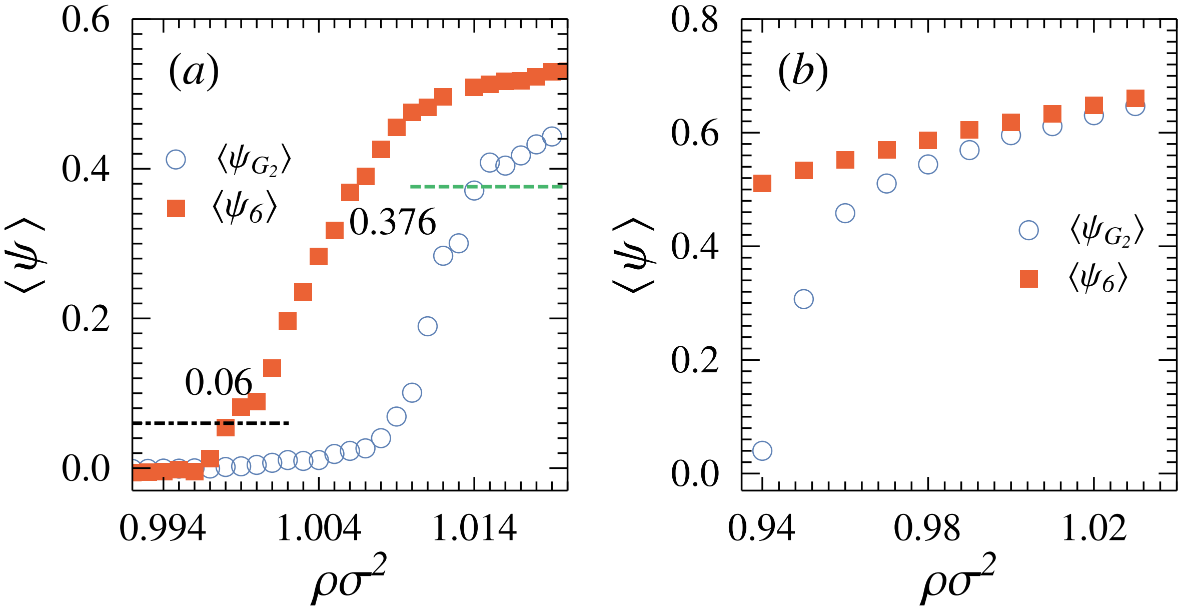

Figure 4.11 Plot of the solid order parameter $\langle\psi_{\mathbf{G}_2}\rangle$ and the hexatic order parameter $\langle\psi_6\rangle$ for the equilibrium phase transition (for more details see Chapter 2). The green dashed line denotes solid melting point $\langle\psi^m_{\mathbf{G}_2}\rangle = 0.376$, and the black dash-dotted line denotes the hexatic melting point $\langle\psi_6\rangle = 0.06$. In figure (b) we show a similar plot for the two order parameters but in the presence of a time- independent potential of the form $U_{ext}(x,y)$ given in Section 4.2 with $V(t) = \varepsilon$. In the presence of this potential, the hexatic does not melt in the regime of $\rho\sigma^2 \geq 0.94$. The external potential maintains a significant hexatic order, with a value greater than $\langle\psi_6\rangle = 0.51$, although the solid order does drop below 0.376 at $\rho\sigma^2 \approx 0.96$.

tion box into sub-boxes of size $\ell = (\ell_x \times \ell_y)^{1/2}$ with $\ell_x/L_x = \ell_y/L_y = 1/14$. The local solid order $\psi^l_{\mathbf{G}_2} \equiv \psi_{\mathbf{G}_2}(\ell)$ is then calculated using the definition of $\psi_{\mathbf{q}}$ restricted within these sub-boxes. For the local hexatic order parameter, we calculate $|\psi^i_6|^2$ for all the particles. The distribution functions of these quantities, $\mathscr{P}(\psi^l_{\mathbf{G}_2})$ and $\mathscr{P}(|\psi^i_6|^2)$ are plotted in Fig. 4.13. They remain unimodal at all points of the phase diagram. At low densities, $\rho\sigma^2 = 0.98$ in Fig. 4.13(a), the maximum of $\mathscr{P}(\psi^l_{\mathbf{G}_2})$ appears at an order parameter corresponding to the solid phase only at the highest frequencies. With decreasing frequency the peak shifts towards lower values, signifying melting below $f\tau = 10$ and remain low at the lowest frequencies. The unimodal nature of the distribution function, as the peak shifts to lower values, signifies the absence of any metastable state across the transition, a characteristic of continuous transitions. At high densities, e.g., $\rho\sigma^2 = 1.04$ in Fig. 4.13(b), corresponding to the re-entrant transition, the peak of the distribution $\mathscr{P}(\psi^l_{\mathbf{G}_2})$ shifts from a high to low and back to high values as the ratcheting rate decreases from the highest frequencies. As before, the unimodal nature of the distribution corresponds to a continuous melting transition.

The solid melts to a hexatic phase, characterized by the finite hexatic order. How-

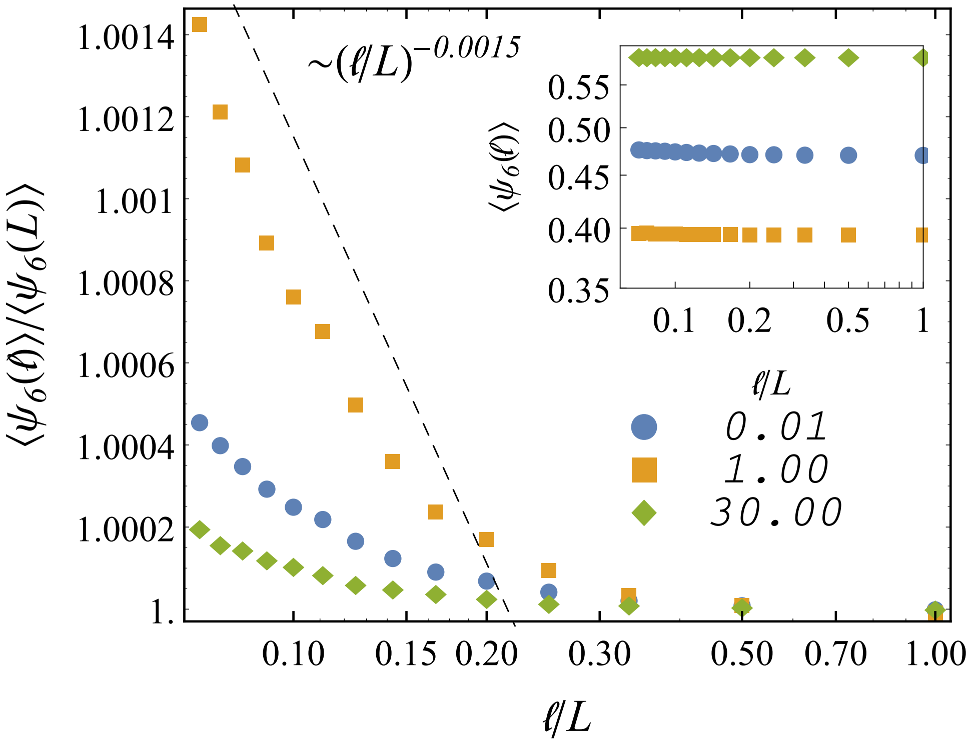

Figure 4.12 (color online) Plot of the finite size scaling ratio $\langle\psi_6(\ell)\rangle/\langle\psi_6(L)\rangle$ for three different frequencies as indicated in the legend at a density of $\rho\sigma^2 = 1.04$. The inset depicts the values of $\langle\psi_6(\ell)\rangle$ as a function of ℓ/L for the three driving frequencies corresponding to main plot.

ever, a further melting of the hexatic is not observed as the frequency is varied. In the density-frequency range bounded between the two dashed lines with open inverted triangles and open circles denoted in Fig. 4.1 (a), the system remains in a hexatic phase. This is corroborated by the distribution of the local hexatic order $\mathscr{P}(|\psi_6^i|^2)$ shown in Fig. 4.13(c) and (d) corresponding to densities $\rho\sigma^2 = 0.98$ and 1.04, respectively. The uni-modal nature of the distribution with a roughly unchanged peak position and a fat tail persists throughout the frequency range. The peak of the distribution does not shift. However, it is important to note that deep inside the hexatic phase, near $f\tau = 1$, a significant fraction of the system displays vanishing hexatic order. This is more prominent at lower densities (see Fig. 4.13(c)).

4.3.5 Pair correlation: quasi- long ranged order to disorder

The pair correlation functions $g(x,y) = \langle\rho(x,y)\rho(0,0)\rangle/\langle\rho\rangle^2$ capture the solid melting. In Fig. 4.15 we show the two dimensional pair correlation functions at $\rho\sigma^2 = 0.98$ and $\rho\sigma^2 = 1.04$ for three representative frequencies: low $(f\tau = 0.01)$, intermediate $(f\tau = 1)$ and high frequency $(f\tau = 30)$. The figures show the correlations over a length scale of

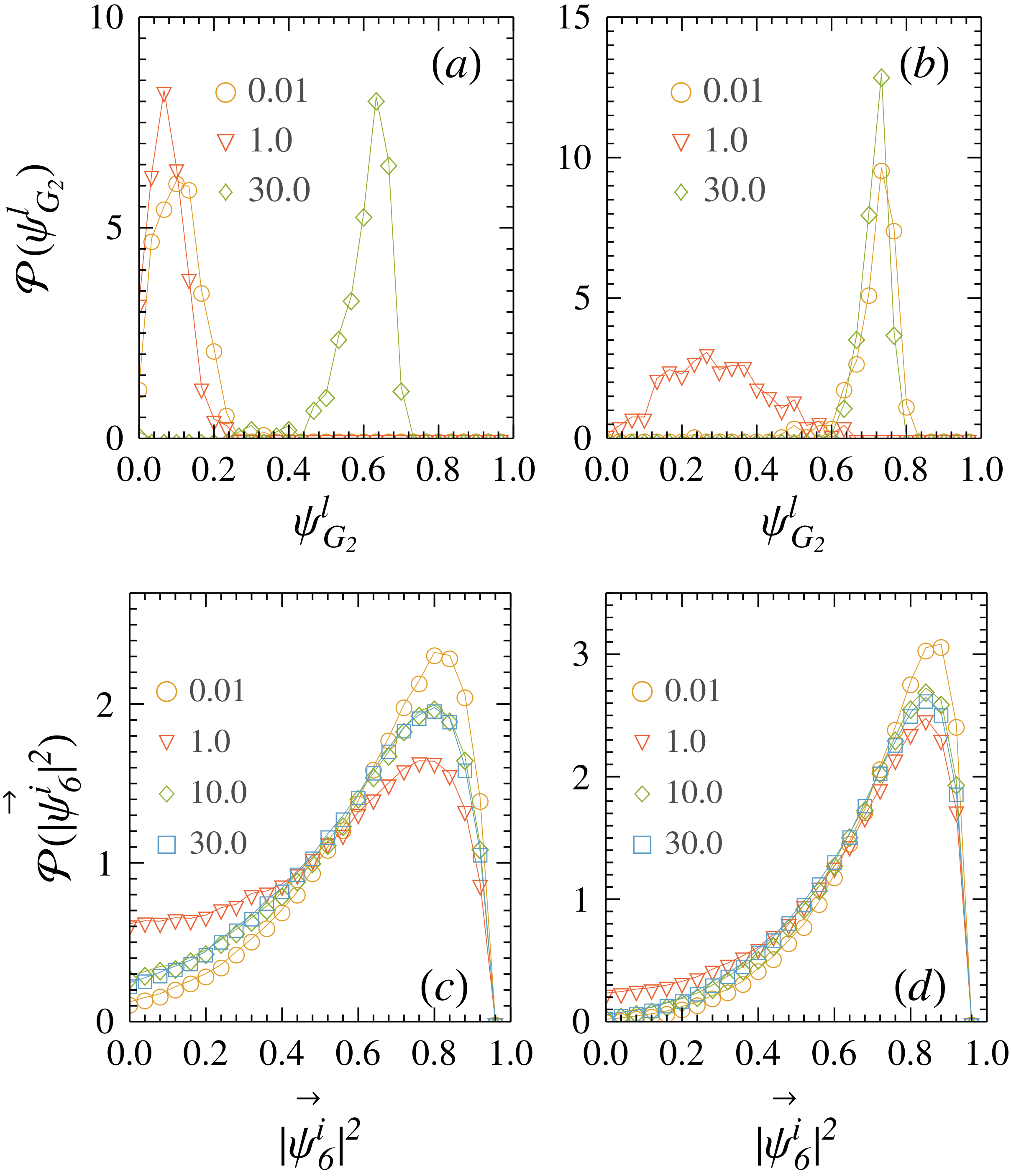

Figure 4.13 Probability distributions of the local solid and hexatic order parameters $\psi^l_{\mathbf{G}_2}$ and $|\psi^i_6|^2$. The distribution functions $\mathscr{P}(\psi^l_{\mathbf{G}_2})$ at densities $\rho\sigma^2 = 0.98\,(a)$ and $\rho\sigma^2 = 1.04\,(b)$. The local solid order parameter is determined over subsystems of length $\ell = (\ell_x \times \ell_y)^{1/2}$, where $\ell_x/L_x = \ell_y/L_y = 1/14$. The distribution functions of local hexatic order $\mathscr{P}(|\psi^i_6|^2)$ at $\rho\sigma^2 = 0.98\,(c)$ and $1.04\,(d)$, corresponding to four representative ratcheting frequencies as indicated in the legends.

$\pm 9\sigma$. While the clear contrast in Fig. 4.15(a), (c) and (f) demonstrate the triangular lattice symmetry, the local diffused approximately triangular structures in the other

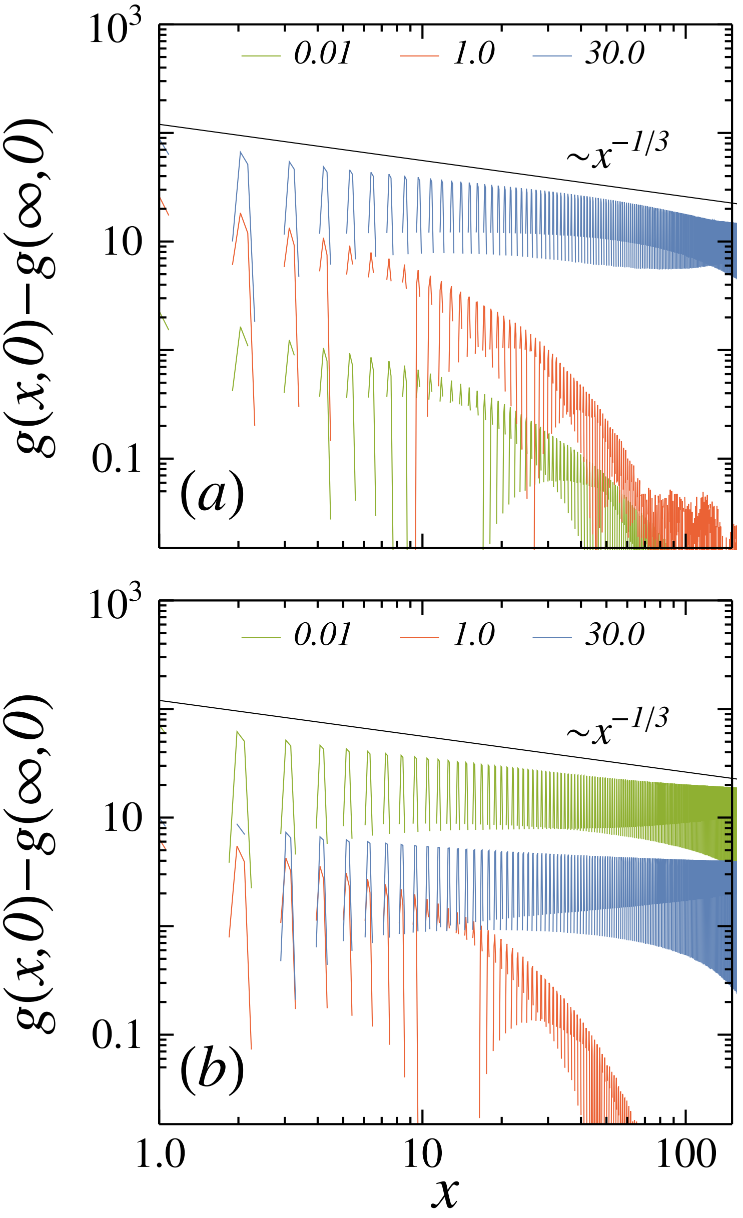

Figure 4.14 (Color Online) The pair correlation functions $g(x,0)-g(\infty,0)$ calculated at the mean densities $\rho\sigma^2 = 0.98$ (*a*) and 1.04 (*b*) for the frequencies indicated in the legends.

$g(x,y)$ figures are characteristic of the hexatic phase.

A density modulation is externally induced in the system along the y-direction by the ratcheting potential, breaking the translational symmetry in that direction, explicitly. To study the spontaneous symmetry breaking, here we focus on the x-component of the two point correlation functions $g(x,y)$. The component of the correlation $g(x,0)-g(\infty,0)$ along the axis perpendicular to the direction of the ratcheting drive are shown in Fig. 4.14. This provides a more conclusive evidence to the nature of the phases in different density and frequency regimes. At low densities, as we have shown before,

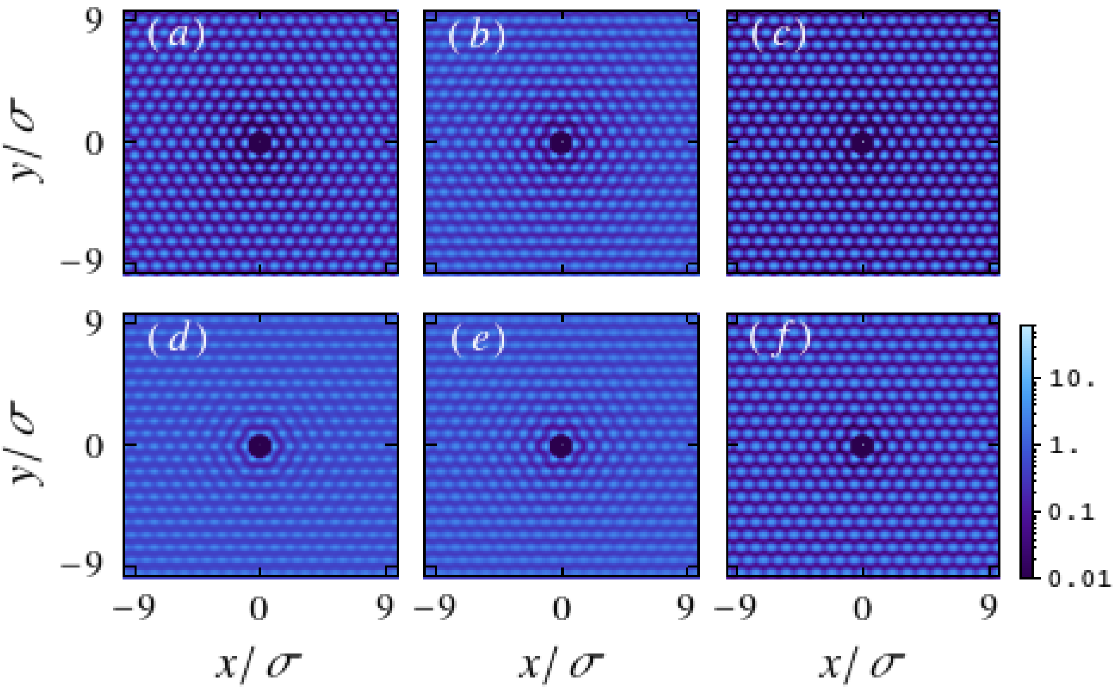

Figure 4.15 Pair correlation functions in the driven 2D colloidal suspension at densities $\rho\sigma^2 = 1.04$ in the top panels (a-c) and $\rho\sigma^2$=0.98 in the bottom panels (d-f) corresponding to three different frequencies $f\tau = 0.01$ (left column), $f\tau = 1$ (middle column) and $f\tau = 30$ (right column).

---

the solid order exists only at the highest frequencies. At such frequencies we find an algebraic decay of the correlation along the x direction, signifying the QLRO (see Fig. 4.14(a)). At intermediate and low frequencies the system melts. This is captured by the exponential decay of the correlation with a correlation length $\sim 10\sigma$ (see Fig. 4.14(a)). The scenario changes at higher densities. At high frequency, as before, we again find a solid phase, with the correlation exhibiting an algebraic decay corresponding to the QLRO (Fig. 4.14(b)). At high densities, one obtains another solid phase at the low ratcheting frequencies. This also shows algebraic decay of correlations signifying QLRO (see $f\tau = 0.01$ graph in Fig. 4.14(b)). The power law $x^{-1/3}$ shown by the black solid lines in the figures denote the expected correlation at the onset of the equilibrium KTHNY melting. At the intermediate driving frequencies, $f\tau = 1$ in $\rho\sigma^2 = 1.04$ system, the correlation shows exponential decay with a correlation length $\sim 10\,\sigma$, similar to the behavior observed in the low density regime (Fig. 4.14(b)). The change from algebraic to exponential decay identifies the solid melting points (open $\triangledown$ and $\circ$) in the phase diagram.

A complete scan of $g(x,0) - g(\infty,0)$ near the phase boundary is depicted in Fig. 4.16. Figures (a)–(h) show the high-frequency melting, while (i)–(p) show possible melting at low frequencies. At $\rho\sigma^2 \lesssim 1.03$ and low frequencies, the decay of the pair correlation

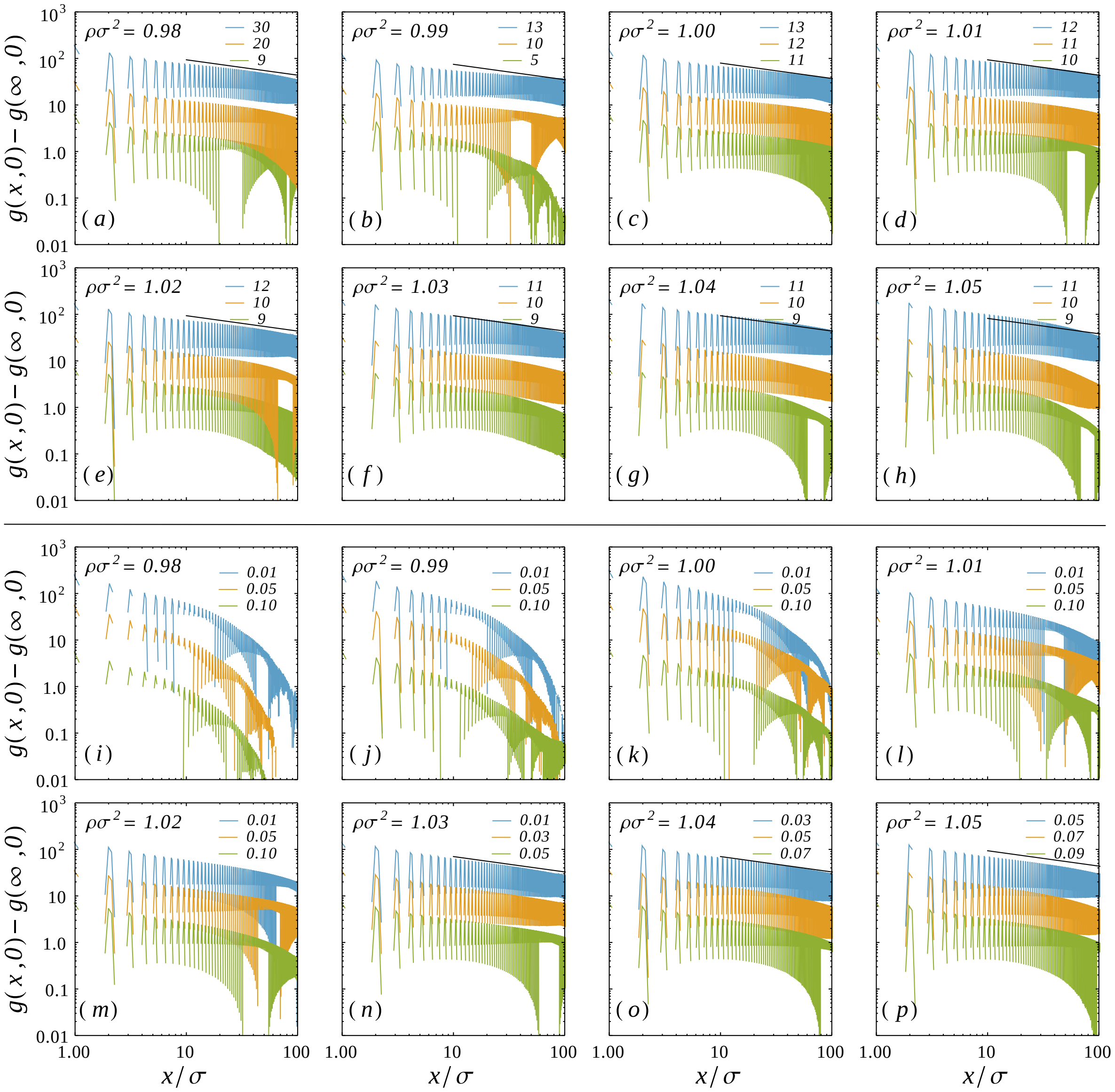

Figure 4.16 Plots of $g(x,0) - g(\infty,0)$ at different densities $\rho\sigma^2$ of the system for frequencies $f\tau$ indicated in the legends. In (a)–(h) we show the data near the high-frequency phase boundary, and in (i)–(p) near the low-frequency phase boundary. The solid black lines denote the power law $x^{-1/3}$ that indicates the expected correlation at the solid melting point within KTHNY thoery[31–33].

function remains always exponential, identifying an absence of transition. A crossover to an algebraic decay in $g(x,0) - g(x,\infty)$ appears at $\rho\sigma^2 \gtrsim 1.03$, resulting in solid- hexatic transition points. The phase boundaries displayed in Fig. 4.1 (a) are consistent with the transition points obtained from this analysis.

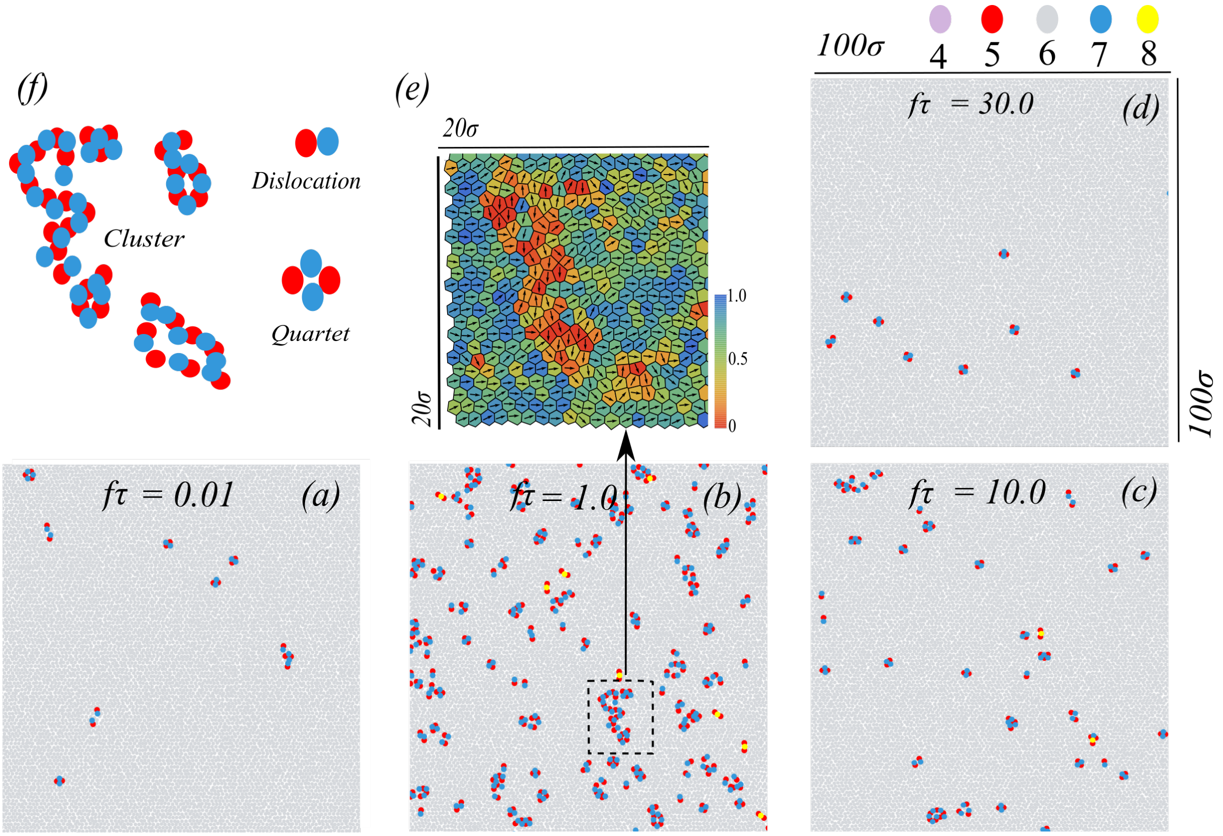

Figure 4.17 (a)-(d): Configurations of the system in $100\sigma \times 100\sigma$ sub-volumes at a density of $\rho\sigma^2 = 1.04$ for frequencies $f\tau = 0.01$ (a), 1 (b), 10 (c) and 30 (d). The particles are color coded according to the number of their topological neighbors n_v, with gray $(n_v = 6)$, blue $(n_v = 7)$, red $(n_v = 5)$, purple $(n_v = 4)$, and yellow $(n_v = 8)$, as shown in the legend on top of (d). (e) The figure highlights the hexatic order in a region containing a connected string of defects marked by a dashed-box of size $20\sigma \times 20\sigma$ in (b). The Voronoi tesselations are shown for each particle within the box and are color coded according to the local value of the hexatic order. The arrows denote the orientation of the local hexatic order ψ_6^i. (f) Indicate typical examples of defect quartets, dislocations and defect clusters that appear in the system.

4.3.6 Defect formation

The equilibrium KTHNY melting of the two- dimensional solid is known to proceed by the unbinding of dislocation pairs into free dislocations. To identify such topological defects, we first obtain the coordination number n_v of each particle in the system counting the number of its Voronoi neighbours. In a perfect triangular lattice $n_v = 6$ for all particles. We follow $n_v \neq 6$ particles to identify the n_v-fold defects. Even within the solid phase, fluctuations of bound quartets of $5-7-5-7$ defects (bound dislocation pairs) keep appearing. They form dislocations by dissociating into separate $5-7$ and $7-5$ non-neighboring pairs. Presence of a finite fraction of particles associated with dislocations characterize the hexatic phase. The system shows dislocation formation as the solid melts. Moreover, we find defect clusters larger than quartets that are

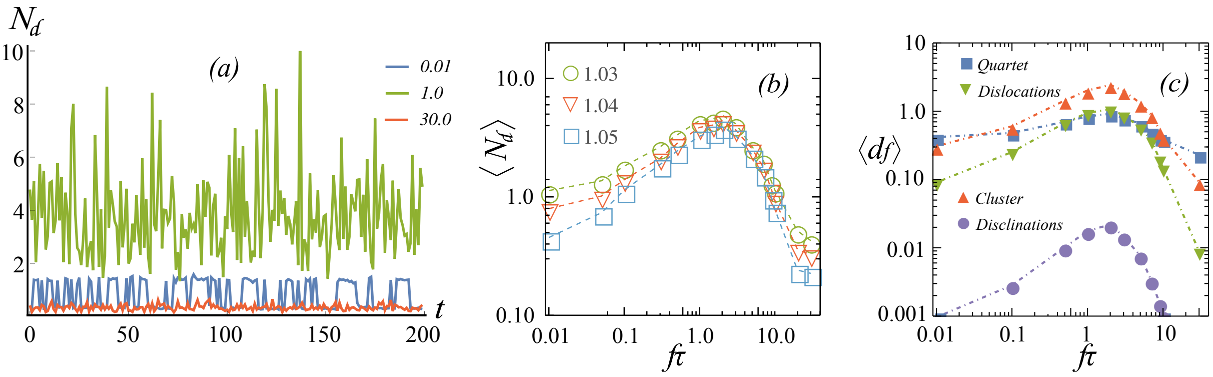

Figure 4.18 (a) Plot of the total defect percentage N_d as a function of time for three different driving frequencies as indicated in the legend. The density of the system is $\rho\sigma^2 = 1.04$. At high frequency the system remains in a solid phase, and the defect formation is significantly low ($N_d < 1\%$). On the other hand, in the opposite limit of low frequency, $f\tau = 0.01$, the defect formation follows the swicthing of the driving potential, N_d switches between two values. In the intermediate current carrying regime, the formation of the defects is maximized. The defects are further classified by types, e.g., quartets, dislocations, clusters, and disclinations. (b) The average defect percentage $\langle N_d \rangle$ shows a non-monotonic variation with the ratcheting frequency. We show results at three densities denoted in the legend. (c) Variation of the time averaged percentage fraction of the individual defect types, the quartets, dislocations, defect clusters, and disclinations with ratcheting frequency.

either compact or string-like (grain boundary).[42,43] All the dominant defect types observed in our simulations are indicated in Fig. 4.17(f). Their typical configurations in a sub-volume of size $100\sigma \times 100\sigma$ at $\rho\sigma^2 = 1.04$ and different ratcheting frequencies are shown in Fig. 4.17(a)-(d). In these figures, the colors associated to particles indicate the number of topological neighbors they have, $n_v = 4$ (purple), 5 (red), 6 (green), 7 (blue), 8 (yellow). Clearly, defect formation is suppressed at both the extremities of the ratcheting frequency. It increases significantly in the intermediate frequency regime associated with solid melting (Fig. 4.17 (b)). The relative fraction of different defect types also vary with the driving frequency. In the highest frequency solids, only bound quartets (bound dislocation pairs) are observed in Fig. 4.17 (d). As the solid melts with decreasing frequency, dislocations and defect clusters start to appear and eventually dominate over the quartets in the system (Fig. 4.17 (b) and (c)). The string-like defects remain extended along the y-direction, the direction of particle current under ratcheting. Such a connected string of defects is shown in Fig. 4.17 (b) and has been highlighted in Fig. 4.17 (e), which shows Voronoi diagram of a region containing the connected string of defects. The color code in each Voronoi cell denotes the amount of hexatic order, and the arrows denote the corresponding hexatic orientations. At the location of the connected clusters of defects, the local hexatic order is low, and shows a hexatic orientation approximately orthogonal to the neighboring defect-free regions. With further lowering of the ratcheting frequency below f_s, the defect fraction decreases strongly.

This description is quantified by focusing on the time evolution of defect fractions. We first consider the evolution of the total fraction of all the topological defects, the percentage of particles having non-six Voronoi neighbors $N_d = (1 - n_6/N) \times 100$, where n_6 denotes the total number of particles with $n_v = 6$ (Fig. 4.18 (a)). Clearly, the largest value of N_d with the strongest fluctuations appear at the intermediate frequencies. The defect formation gets dramatically suppressed in the solid phase corresponding to the high ratcheting frequencies. At the lowest frequencies ($f\tau = 0.01$ in Fig. 4.18 (a)), N_d remains relatively low and follows the switching of external potential.

The mean value of $\langle N_d \rangle$ remanis less than 4% and varies non-monotonically with $f\tau$ (Fig. 4.18 (b)). It shows a maximum at the resonance frequency corresponding to the largest directed current, relating formation of topological defects with carrying capacity of particle current in the system.

Further insight into the structure- dynamics relations can be obtained by following the behavior of different defect fractions separately. For this purpose, the percentage fraction d_f of a defect type is defined as $d_f = (n_d/N) \times 100$, where n_d is the total number of $n_v \neq 6$ particles that may contribute to either a quartet, a dislocation, a cluster, or a disclination as described above. The time averaged percentage fractions of these topological defects as a function of the driving frequency is shown in Fig. 4.18 (c). They exhibit a similar non-monotonic behavior as N_d and the mean particle current. In the high frequency solid, the dominant defects are the quartets. As the frequency is decreased, the melting of the solid is mediated by the unbinding of these quartets into dislocations. The dislocation fraction becomes larger than that of quartets. More importantly, at the resonance melting, the formation of defect clusters dominate (Fig. 4.18(c)). The fraction of disclinations remain relatively insignificant (less than 0.03%), about two orders of magnitude smaller than that of the defect clusters. This is consistent with the fact that the hexatic does not melt within these parameter regimes.

4.4 Discussion

In conclusion, using a large scale simulation involving 262144 particles, we have presented a detailed study of a ratcheted two-dimensional colloidal suspension, focusing on the structure- dynamics relationship. The mean directed particle current driven by the ratchet exhibits a resonance behavior. Associated with this, the solid melts to hexatic providing a mechanism allowing directed transport. The system exhibits a rich non-equilibrium phase diagram as a function of the driving frequency and mean density. At high densities, we found a re-entrant melting transition as a function of ratcheting frequency. The system melts as it starts to carry more and more directed particle current. This can be viewed as a depinning with increasing tilt of the effective tilted periodic potential due to flashing ratchet. The relative displacements of neighboring particles are shown to stretch out in a diffusive manner after solid melting. The different phases are characterized by the spatially resolved density profile, the pair correlation function, the structure factor, the solid and hexatic order parameters, and their distribution functions. The role of the defects in the phase transition has been investigated in detail. The solid- melting is associated with formation of dislocations, but unlike the equilibrium two- dimensional melting, this non-equilibrium melting is dominated by the formation of defect clusters, connected strings of defects that remain oriented largely along the direction of the ratcheting drive. Remarkably, the driven hexatic does not melt to a fluid within the studied range of density and ratcheting drive. Our detailed predictions regarding the variation of particle current and associated phase transitions can be verified using colloidal particles and optical[12] or magnetic ratcheting[15] in a suitable laser trapping setup[27]. The impact of changing degree of potential asymmetry on the dynamics and phase behavior remains an interesting future direction of study.

Bibliography

[1] F. Julicher, A. Ajdari and J. Prost, *Reviews of Modern Physics*, 1997, **69**, 1269–1282.

[2] R. D. Astumian and P. Hänggi, *Physics Today*, 2002, **55**, 33.

[3] P. Hänggi, *Reviews of Modern Physics*, 2009, **81**, 387–442.

[4] P. Reimann, *Physics Reports*, 2002, **361**, 57–265.

[5] P. Brouwer, *Phys. Rev. B*, 1998, **58**, R10135–R10138.

[6] R. Citro, N. Andrei and Q. Niu, *Phys. Rev. B*, 2003, **68**, 165312.

[7] K. Jain, R. Marathe, A. Chaudhuri and A. Dhar, *Phys. Rev. Lett.*, 2007, **99**, 190601.

[8] D. Chaudhuri and A. Dhar, *EPL (Europhysics Letters)*, 2011, **94**, 30006.

[9] D. Chaudhuri, A. Raju and A. Dhar, *Phys. Rev. E*, 2015, **91**, 050103.

[10] D. Chaudhuri, *J. Phys. Conf. Ser.*, 2015, **638**, 012011.

[11] D. C. Gadsby, A. Takeuchi, P. Artigas and N. Reyes, *Philos. Trans. R. Soc. B Biol. Sci.*, 2009, **364**, 229–238.

[12] L. Faucheux, L. Bourdieu, P. Kaplan and A. Libchaber, *Physical Review Letters*, 1995, **74**, 1504–1507.

[13] B. Lopez, N. Kuwada, E. Craig, B. Long and H. Linke, *Physical Review Letters*, 2008, **101**, 220601.

[14] P. Tierno, P. Reimann, T. H. Johansen and F. Sagués, *Physical Review Letters*, 2010, **105**, 230602.

[15] P. Tierno, *Physical Review Letters*, 2012, **109**, 198304.

[16] J. Rousselet, L. Salome, A. Ajdari and J. Prost, *Nature*, 1994, **370**, 446.

[17] S. Leibler, *Nature*, 1994, **370**, 412.

[18] C. Marquet, A. Buguin, L. Talini and P. Silberzan, *Physical Review Letters*, 2002, **88**, 168301.

[19] I. Derényi and T. Vicsek, *Physical review letters*, 1995, **75**, 374.

[20] I. Derényi and A. Ajdari, *Physical Review E*, 1996, **54**, R5–R8.

[21] R. Marathe, K. Jain and A. Dhar, *J. Stat. Mech. Theory Exp.*, 2008, **2008**, P11014.

[22] S. Savel'ev, F. Marchesoni and F. Nori, *Phys. Rev. E*, 2004, **70**, 061107.

[23] A. Pototsky, A. J. Archer, M. Bestehorn, D. Merkt, S. Savel'ev and F. Marchesoni, *Phys. Rev. E*, 2010, **82**, 030401.

[24] S. Savel'ev, F. Marchesoni and F. Nori, *Phys. Rev. Lett.*, 2003, **91**, 010601.

[25] D. Chakraborty and D. Chaudhuri, *Physical Review E - Statistical, Nonlinear, and Soft Matter Physics*, 2015, **91**, 050301(R).

[26] A. Chowdhury, B. J. Ackerson and N. A. Clark, *Phys. Rev. Lett.*, 1985, **55**, 833.

[27] Q.-H. Wei, C. Bechinger, D. Rudhardt and P. Leiderer, *Physical Review Letters*, 1998, **81**, 2606–2609.

[28] E. Frey, D. R. Nelson and L. Radzihovsky, *Phys. Rev. Lett.*, 1999, **83**, 2977.

[29] D. Chaudhuri and S. Sengupta, *Physical Review E*, 2006, **73**, 11507.

[30] C. Reichhardt and C. J. Olson Reichhardt, *Reports Prog. Phys.*, 2017, **80**, 26501.

[31] J. M. Kosterlitz and D. J. Thouless, *J. Phys. C*, 1973, **6**, 1181.

[32] B. I. Halperin and D. R. Nelson, *Phys. Rev. Lett.*, 1978, **41**, 121–124.

[33] A. P. Young, *Phys. Rev. B*, 1979, **19**, 1855.

[34] S. C. Kapfer and W. Krauth, *Physical Review Letters*, 2015, **114**, 035702–5.

[35] D. Frenkel and B. Smit, *Understanding molecular simulation: from algorithms to applications*, Academic press, NY, 2002.

[36] F. Jülicher and J. Prost, *Physical Review Letters*, 1997, **78**, 4510–4513.

[37] W. Li, K. Wang, C. Reichhardt, C. J. O. Reichhardt, M. S. Murillo and Y. Feng, *Phys. Rev. E*, 2019, **100**, 033207.

[38] Q. Le Thien, D. McDermott, C. J. Olson Reichhardt and C. Reichhardt, *Phys. Rev. B*, 2016, **93**, 014504.

[39] Q. Lu, C. J. O. Reichhardt and C. Reichhardt, *Phys. Rev. B*, 2007, **75**, 054502.

[40] P. M. Chaikin and T. C. Lubensky, *Principles of Condensed Matter Physics*, Cambridge University Press, Cambridge, 2012.

[41] W. Mickel, S. C. Kapfer, G. E. Schröder-Turk and K. Mecke, *J. Chem. Phys.*, 2013, **138**, 044501.

[42] W. Qi, A. P. Gantapara and M. Dijkstra, *Soft Matter*, 2014, **10**, 5449–5457.

[43] C. Reichhardt and C. J. Olson Reichhardt, *Phys. Rev. E*, 2006, **73**, 046122.

5

Summary and Outlook

In this thesis, the melting of a two dimensional colloidal suspension is studied for a free and a driven system. We used large scale molecular dynamics simulations, implemented on Graphics Processing Units, to investigate the corresponding melting scenarios. Despite the fact that the melting of a two-dimensional solid is almost a 40 years old problem, and a significant amount of effort dedicated to the problem,[1–20] there seems to be little consensus on the melting scenarios of system. The celebrated KTHNY theory[21–24]is not universally applicable to all systems, but rather the melting scenarios are sensitive to atomistic parameters such as shape, interaction and pinning.[6,7,14,16,18,20] Even for the simplest system of hard-disks, a conclusive evidence was obtained only a decade ago. In contrast, for a repulsively interacting colloidal suspension with $U(r) \sim r^{-12}$, the melting scenarios were debated as recently as 2019.[17,20]

The first part of the thesis concentrates on the equilibrium phase transition in two-dimensional colloidal systems. Our study on equilibrium phase transition was motivated from this fact, with a view to settle this issue. Additionally, we also observed that there is dearth of results on the melting scenarios of two-dimensional colloidal suspension with Weeks-Chandler-Anderson (WCA) interaction. The results of our studies on the melting scenarios of a two-dimensional colloidal suspension with a repulsive pair-interaction is presented in Chapter 2, and with a WCA interaction is presented in Chapter 3. The different phases in the system are identified by the pair-correlation function, the solid and the orientational order parameter correlation functions and their finite size scaling. In both the cases, we find that the melting proceeds via a two-step process. The solid phase melts to a hexatic phase via a continuous transition, in conformation with the KTHNY theory. The nature of the transition is identified from the behavior of the distribution of the local solid-order parameter. For a repulsively interacting colloidal suspension, the melting of the solid happens at the density $\rho\sigma^2 = 1.014$, whereas the WCA solid melts at the density $\rho\sigma^2 \approx 0.920$.

In contrast, the hexatic-liquid transition proceeds via a weak first order transition. A stable hexatic phase is found up to the density $\rho\sigma^2 = 1.006$ for a repulsively interacting colloidal dispersion, and $\rho\sigma^2 = 0.906$ for a colloidal system interacting with WCA system. The isotropic liquid is found at the densities $\rho\sigma^2 = 0.996$ and $\rho\sigma^2 = 0.898$ for the repulsive and WCA interaction, respectively.

The melting of a repulsively interacting colloidal suspension driven by a one dimensional stochastic flashing ratchet is the focus of the second part of the thesis. Such an out-of equilibrium condition was specifically chosen since the drive is known to generate a time-averaged particle current through the system. A non-equilibrium melting was associated with the particle current. The system exhibits a rich phase diagram as a function of the driving frequency and the density. We observed a re-entrant melting transition as a function of the driving frequency. The role of defect formations in the non-equilibrium melting has also been studied in detail. The melting of the solid proceeds via the unbinding of the quartets into dislocations. Remarkably, the hexatic phase of the driven system does not melt further into a liquid. The role of potential asymmetry on particle current and thermodynamic phases remains an open question and definite future direction of study.

Bibliography

[1] J. Broughton, G. Gilmer and J. Weeks, *Physical Review B*, 1982, **25**, 4651.

[2] S. Toxværd, *Phys. Rev. Lett.*, 1983, **51**, 1971–1974.

[3] K. J. Strandburg, *Phys. Rev. B*, 1986, **34**, 3536.

[4] J. A. Zollweg and G. V. Chester, *Phys. Rev. B*, 1992, **46**, 11186–11189.

[5] H. Aranda-Espinoza, M. Carbajal-Tinoco, E. Urrutia-Bañuelos, J. L. Arauz-Lara, M. Medina-Noyola and J. Alejandre, *The Journal of Chemical Physics*, 1994, **101**, 10925.

[6] J. F. Fernández, J. J. Alonso and J. Stankiewicz, *Phys. Rev. Lett.*, 1995, **75**, 3477–3480.

[7] P. Bladon and D. Frenkel, *Phys. Rev. Lett.*, 1995, **74**, 2519–2522.

[8] Q.-H. Wei, C. Bechinger, D. Rudhardt and P. Leiderer, *Physical Review Letters*, 1998, **81**, 2606–2609.

[9] J.-d. Bao and Y.-z. Zhuo, *Physics Letters A*, 1998, **239**, 228.

[10] A. Jaster, *Phys. Rev. E*, 1999, **59**, 2594–2602.

[11] C. F. Chou, O. Bakajin, S. W. Turner, T. a. Duke, S. S. Chan, E. C. Cox, H. G. Craighead and R. H. Austin, *Proceedings of the National Academy of Sciences of the United States of America*, 1999, **96**, 13762–5.

[12] M. A. Bates and D. Frenkel, *Phys. Rev. E*, 2000, **61**, 5223–5227.

[13] K. Mangold, P. Leiderer and C. Bechinger, *Physical Review Letters*, 2003, **90**, 158302.

[14] E. P. Bernard and W. Krauth, *Phys. Rev. Lett.*, 2011, **107**, 155704.

[15] S. Deutschländer, T. Horn, H. Löwen, G. Maret and P. Keim, *Phys. Rev. Lett.*, 2013, **111**, 098301.

[16] W. Qi, A. P. Gantapara and M. Dijkstra, *Soft Matter*, 2014, **10**, 5449–5457.

[17] S. C. Kapfer and W. Krauth, *Physical Review Letters*, 2015, **114**, 035702–5.

[18] J. A. Anderson, J. Antonaglia, J. A. Millan, M. Engel and S. C. Glotzer, *Phys. Rev. X*, 2017, **7**, 021001.

[19] A. L. Thorneywork, J. L. Abbott, D. G. A. L. Aarts and R. P. A. Dullens, *Physical Review Letters*, 2017, **118**, 158001–5.

[20] A. Hajibabaei and K. S. Kim, *Phys. Rev. E*, 2019, **99**, 022145.

[21] J. M. Kosterlitz and D. J. Thouless, *J. Phys. C*, 1973, **6**, 1181.

[22] B. I. Halperin and D. R. Nelson, *Phys. Rev. Lett.*, 1978, **41**, 121–124.

[23] D. R. Nelson and B. I. Halperin, *Phys. Rev. B*, 1979, **19**, 2457.

[24] A. P. Young, *Phys. Rev. B*, 1979, **19**, 1855.

List of Figures

Figure 1.1 Pressure-temperature plane in three dimensional space 7

Figure 1.2 Sketch representing the longest wavelength of spins fluctuation in the system of size L in one dimensional space. 10

Figure 1.3 Schematic representation of XY Model. In (a) spins residing on the sites of a square lattice and (b) representing the allowed values that each spin can take. 11

Figure 1.4 Figure (a) represents a perfect triangular lattice, in which each site is surrounded by six neighbors. Figure (b) shows generation of a dislocation in an otherwise perfect triangular lattice as a result of inserting two half planes (highlighted with yellow color) inside it. At the point where these planes terminate, a five-fold defect together with a seven-fold defect is generated. The closed Burger circuit around the dislocation is shown in blue color. The black dashed line represents the Volterra-cut. If the crystal is cut along this line up to its tip and both sides of it get shifted relative to each other by a lattice spacing a , the structure of the perfect triangular crystal gets recovered. . . 16

Figure 1.5 Figure (a) presents dislocation-pair inside a solid. Because of thermal fluctuations, particles are displaced from their equilibrium positions. In the process two particles loose one of their neighbor in each and as a result the other two particles accompanied with an additional neighbor. This distortion generates local stress in the system and is represented by blue vectors. At sufficient high temperature the thermal energy overcomes this stress and in order to increase local stress field, the dislocation-pair get dissociated into two free dislocations. Figure (b) represent the state of free dislocations. The alignment of green color vectors with the black head around the distorted area, shows orientation in the crystal remains unaffected in the presence of both paired and free dislocations. 17

Figure 1.6 Figure (a) and (b) represent generation of a free five-fold and seven-fold defect in an otherwise perfect triangular lattice respectively. These isolated defects can be generated by twisting the two sides of the Volterra-cut through angles $\pm\pi/3$ relative to each other. The five-fold defect known to be positive disclination, is produced as a result of rotation through $+\pi/3$ and the rotation through $-\pi/3$ creates seven-fold defect also known as negative disclination. Note that the presence of disclinations breaks the orientational order of the system as green vectors around these defects are not in the same direction. 18

Figure 1.7 Sketch representing the trapping of a suspended particle on the center axis of a focused light beam. k_1 and k_2 are the momenta that the particle experiences because of the outgoing refracted rays '1' and '2' respectively. K_t is their resultant momentum and is in upward (-y) direction. 22

Figure 1.8 Schematic representation of particles confined between the troughs of a periodic optical potential. 23

Figure 1.9 A schematic representation of Feynman Ratchet device. It consists of a rod with vanes attached to it at one end, and a ratchet wheel at the other end. The wheel is in contact with a pawl, which is held by a piece of spring. The presence of pawl makes the ratchet wheel to move only in one direction. Both ends of the rod are placed inside the containers of gas. The temperatures of the two containers are T_1 and T_2. 25

Figure 1.10 Sketch representing the dynamics of a Brownian particle in the presence of one dimensional, time dependent ratchet potential. The potential has the periodicity 'L' and changes its state between $'On'$ and $'Off'$ phases with time. The parameter α controls the spatial asymmetry. For $\alpha < 1.0$ the distance between a minima and its consecutive maxima in the forward (+y) direction (αL) becomes smaller than the distance which it shares with the maxima in backward (-y) direction ($L - \alpha L$). 27

Figure 2.1 Time-averaged pressure as a function of system density is shown for the density range from $\rho\sigma^2 = 0.978$ to 1.03. There is almost a flat line of value ~14.70 from $\rho\sigma^2 = 0.998$ to 1.009. The zoomed picture of this region is highlighted in the inset plot. It shows that the pressure value actually has positive increment with density though the variation is very little ranging from the value of ~14.65 to ~14.73. 40

Figure 2.2 In Figure (a): schematic representation of two dimensional triangular lattice. The lattice spacing and corresponding reciprocal lattice vectors are indicated on top of it. Figure (b): **SSF plane**: six intensity peaks at corresponding reciprocal lattice vectors for triangular crystalline structure. Figure (c): The calculated time-averaged solid order parameter $\langle\psi_{G_2}\rangle$ as a function of system density $\rho\sigma^2$. The cut at 0.376 indicates the hexatic-solid transition point. Figure (d): Fluctuation of solid order parameter as a function of system density. . . . 42

Figure 2.3 The static structure factor for different densities of the system as indicated in the legend. $\psi_{\mathbf{q}}$ is calculated in the Fourier plane with resolution interval of $0.01\sigma^{-1}$.The sequence depicts the melting of the solid to a hexatic and the melting of the hexatic to an isotropic liquid phase.Plot of SSF 43

Figure 2.4 Time-averaged pair-correlation function g(x,y) is shown for the densities indicated on top of each plot. For clear visibility it is shown in the length scale of $20\sigma\times 20\sigma$. The calculations are done by aligning Δx in the direction of system orientation. Plot corresponding to the density $\rho\sigma^2$=1.014 belongs to the solid and for $\rho\sigma^2$=0.996 to the isotropic liquid phase. 44

Figure 2.5 Scan of pair-correlation g(x,y) along x-axis with the window of $40\sigma\times 40\sigma$ for densities $\rho\sigma^2 = 1.012$ (upper panel) and 1.014 (lower panel). At $\rho\sigma^2 = 1.014$ periodic arrangement can be seen throughout the range. whereas it disappears at large distances for $\rho\sigma^2 = 1.012$. . . . 45

Figure 2.6 A cut taken along $\mathbf{r} = (x,0)$ from the two dimensional pair-correlation function g(x,y) is shown for various densities. The densities belonging to the different colors are indicated inside the plot. At $\rho\sigma^2$ =1.014 the function g(x,0)-1 shows power law decay. The black dashed line with the decaying slope of 1/3 inside the plot is to compare the stability criteria for solids as predicted in KTHNY theory. For lower densities the decaying function shifts its behaviour from algebraic to the exponential form. 46

Figure 2.7 Plot of the spatial correlation of the solid order parameter for different densities as indicated in the legend. A stable solid is determined from the decay of the correlation function. KTHNY theory predicts an algebraic decay with an exponent $\eta \leq 1/3$, where the equality denotes the boundary of the stable solid phase and is indicated by the dashed line in the figure. The lowest density at which we observe a decay of the form $r^{-1/3}$ corresponds to the density $\rho\sigma^2 = 1.014$. Below this density, the decay transforms from an algebraic to an exponential form. 47

Figure 2.8 Finite size scaling of the solid order parameter for different densities as indicated in the legend. To study the finite size scaling, the system was divided in sub-boxes of size $\ell_x \times \ell_y = \ell^2$, and the solid order parameter was determined using the definition $\langle \psi_{\mathbf{G}_2} \rangle = \langle \rho_{\mathbf{q}} \rho_{-\mathbf{q}} \rangle$ but restricted to these sub-boxes. In the KTHNY theory, the ratio of the local to the global solid order parameter decays as a power law: $\langle \psi_{\mathbf{G}_2}(\ell) \rangle / \langle \psi_{\mathbf{G}_2}(L) \rangle \sim (\ell/L)^{-\nu}$, with $\nu \leq 1/3$. The equality marks the boundary of the stable solid phase, indicated by the dashed line in the figure. The solid melting occurs at the density of $\rho\sigma^2 = 1.014$. As the density is decreased beyond this value, the decay is no longer algebraic and bears the signature of short range positional order in the system. 48

Figure 2.9 A partcle having six topological neighbors is presented in figure (a). The neighbors are calculated by identifying Voronoi cell for each of the particles. First for a given particle 'j', we select candidates within a cut-off radius. Next we find the bond length r_{jk} between j^{th} particle and these candidates. Then perpendicular bisectors for each of the bond length is calculated. The points where these bisectors meet, form the vertices of the Voronoi cell for the j^{th} particle. Partcles which share at at least one of edges of Voronoi cell are considered as topological neighbors. 50

Figure 2.10 Plots of the time-averaged orientational order parameter $\langle \psi_6 \rangle$ (figure (a)) and its fluctuations $\langle \Delta\psi_6^2 \rangle$ (figure (b)) as a function of system density $\sigma^2\rho$. The cuts at the values 0.06 and 0.514 in figure (a) represent the liquid to hexatic and hexatic to solid transition points respectively. The maximum of the fluctuations occur at the density $\rho\sigma^2 \approx 0.998$, indicating the hexatic-liquid transition point. 50

Figure 2.11 Spatial correlation of bond angle orientations $g_6(r)$ is shown for the densities indicated in the legends. The black dot-dashed line is the plot of $r^{-1/4}$ that marks the upper bound for the stable hexatic according to the prediction of KTHNY theory. The lowest density at which a stable hexatic phase is obtained is that of $\rho\sigma^2 = 1.001$. A pure exponential decay of the correlation function throughout the system, characteristic of the isotropic liquid phase, is obtained at densities below $\rho\sigma^2 = 0.996$. In the intermediate density regime, the correlation shows an exponential decay up to 50σ and crosses over to an algebraic decay with an exponent greater than $1/4$. 51

Figure 2.12 Finite size scaling of the orientational order parameter for different densities as indicated in the legend. The system was divided into blocks of size $\ell_x \times \ell_y = \ell^2$ and the orientational order parameter was calculated using Eq. (2.7), restricting the sum in the block. KTHNY theory predicts the ratio $\psi_6(\ell)/\psi_6(L)$ to scale as $(\ell/L)^{-\eta_6(\rho)}$, with $\eta_6(\rho) \leq 1/4$. The equality marks the boundary of the stable hexatic phase and is indicated by the black dashed line. The dot-dashed lines passing through the symbols are guide to the eye. A stable hexatic phase is obtained up to the density $\rho\sigma^2 \approx 1.001$. Below this density, the finite size scaling shows the signature of short-range orientational order. 53

Figure 2.13 Distribution of local solid order parameter for the densities as indicated in the legend. The whole system was divided into 100×100 boxes and the local solid order parameter was calculated by computing the density mode $\rho_{\mathbf{G}_2}$, restricted to these sub-boxes. The distribution is uni-modal both in solid ($\rho\sigma^2 = 1.014$) and in liquid phase ($\rho\sigma^2 = 0.996$). With the melting of the solid to a hexatic phase, the distribution broadens, but there is clear absence of bi-modality in the distribution. This indicates that the transition is continuous. 54

Figure 2.14 Coarse-grained plots of the orientational order parameter in the system for different densities as indicated on the top. The heatmap was obtained by dividing the whole system into 16×16 blocks.The local orientational order $\psi_6(\mathbf{r})$ is calculated inside each block using the particle based definition ψ_6^i and restricting the sum in Eq. (2.7) over the sub-boxes. Overlapped on the heatmap are the local orientation vectors $(\mathrm{Re}\,\psi_6(\mathbf{r}), \mathrm{Im}\,\psi_6(\mathbf{r}))$ indicated by the arrows. Below the stable hexatic boundary ($\rho\sigma^2 < 1.001$), the system shows patches of coexisting regions of high and low hexatic order. 55

Figure 2.15 Time evolution of coarse-gained orientational order at the density $\rho\sigma^2 = 0.998$. The heatmap at each time snapshot was obtained by dividing the whole system into 16×16 blocks.The local orientational order $\psi_6(\mathbf{r})$ is calculated inside each block using the particle based definition ψ_6^i and restricting the sum in Eq. (2.7) over the sub-boxes. Overlapped on the heatmap are the local orientation vectors $(\mathrm{Re}\,\psi_6(\mathbf{r}), \mathrm{Im}\,\psi_6(\mathbf{r}))$ indicated by the arrows. The time evolutions indicate a stable macrophase separation of high and low hexatic order. 55

Figure 2.16 Distribution of local orientational order for the densities as indicated in the legend. The whole system was divided into 100×100 boxes and local order is calculated for a given configuration. A total of 200 independent configurations were used to construct the probability distribution $\mathscr{P}(\psi_6^\ell)$. As the solid melts to a hexatic, the distribution retains the uni-modal feature, but develops a fat tail with finite probabilities for lower values of hexatic order. At the boundary of the stable hexatic, we see the start of a weak bi-modality in the distribution with almost equal peaks at the density $\rho\sigma^2 = 1.000$. Very close to the liquid melting point ($\rho\sigma^2 = 0.997$), the signature of a intermediate metastable state is evident. 56

Figure 3.1 Variation of the thermodynamic pressure with density for two different system sizes as indicated inside the plot.The inset depicts a zoomed section of the main plot, for the comparatively larger system size 256^2, to highlight the Meyer-Wood loop within the density range $\rho\sigma^2 = 0.898$ to 0.922. 63

Figure 3.2 The static structure factor for different densities of the system as indicated in the legend. $\langle\psi_\mathbf{q}\rangle$ is calculated in the Fourier plane with resolution interval of $0.01\sigma^{-1}$.The sequence depicts the melting of the solid to a hexatic and the melting of the hexatic to an isotropic liquid phase. 65

Figure 3.3 Plot of the solid order parameter (a) and its fluctuation (b) as a function density. The peak of the order parameter fluctuation occurs at a density $\rho\sigma^2 = 0.918$. Irrespective of the nature of the transition, the peak of the solid order parameter fluctuation indicates the melting of the solid. 65

Figure 3.4 Pair correlation correlation $g(x,y)$ is shown for various densities as indicated inside each plot. In the solid phase, $g(x,y)$ shows the characteristic triangular lattice structure. As the solid melts, the triangular lattice structure overlaps with concentric hexagonal rings characteristic of the hexatic phase. In the liquid phase, these hexagonal rings transforms into completely symmetric circular rings that reflects the isotropy of the system. 66

Figure 3.5 The cut of the pair correlation $g(x,0)-1$ is shown in the double-logarithmic scale in (a) and in log scale in (b) for the densities indicated in the legend. The black dashed line shows the plot of $x^{-1/3}$ that identifies the stable solid phase. From the decay of the correlation, the hexatic-solid transition happens at the point $\rho\sigma^2 = 0.920$. For the densities below this point, there is an exponential decay observed in the pair correlation function. 67

Figure 3.6 **(a)–(b)**:The spatial correlation of solid order parameter $g_{\mathbf{G}}(r)$ is shown in the double logarithmic scale for the densities indicated in the legend. Here $\mathbf{G} = 2\pi/a$ is one of the reciprocal lattice vector out of six vectors, at which Bragg peaks are obtained in the static structure factor plane for the stable solid phase. The black dashed line shows the plot of $r^{-1/3}$ to clearly identify the solid-hexatic melting point. At densities below $\rho\sigma^2 = 0.920$, the decay of the correlation is short-ranged. **(c)–(f)**: Sequence of plots that depicts the shift in $\mathbf{G}_2$ for different densities. 68

Figure 3.7 Finite size scaling of solid order parameter ψ_G in double logarithmic scale. The dashed black line is the plot of $(\ell/L)^{-1/3}$ slope that indicates the boundary of the stable solid phase. For densities $\rho\sigma^2 \geq 0.920$ the system goes into a stable solid phase and $\rho\sigma^2 = 0.920$ is the solid-hexatic melting point. 70

Figure 3.8 Plot of the bond orientational order parameter (a) and its fluctuation (b) as a function density. The peak of the order parameter fluctuation occurs at a density $\rho\sigma^2 = 0.906$. 72

Figure 3.9 Spatial correlation of the orientational order parameter $g_6(r)$ is shown for different densities. At the density $\rho\sigma^2 = 0.920$, the orientational order is long ranged and does not exhibit a decay. As the solid melts to a hexatic, the long ranged order transforms into a quasi-long ranged order and the correlation decays as a power law with an exponent $\eta \leq 1/4$. In the liquid phase the correlation becomes short-ranged, decaying exponentially. 74

Figure 3.10 System size scaling of orientational order parameter ψ_6 for the densities indicated in the legend. The dashed line indicates the $-1/4$ slope and is the boundary of a stable hexatic. The data shows that for densities $\rho\sigma^2 > 0.906$ the system is in a stable hexatic phase. . . 75

Figure 3.11 **(a)**: Variation of percentage defect-fraction d_f with system density $\rho\sigma^2$. **(b)**: The percentage fraction of quartets, dislocations and disclinations are shown as a function of the system density. **(c)**: Plot of the quantity d_c, the percentage fraction of 5 fold and 7 fold defects that contribute to form either a quartet, dislocation or disclination, as a function of density. 76

Figure 3.12 Defects formation and its effect on local orientation order is shown for different phases of the system. In the top panel, particles with different number of neighbors are shown inside their respective voronoi cells. They can be distinguished by different colors given to them. The legend at the bottom of the extreme right plot represents this color code. In the solid phase $\rho\sigma^2 = 0.922$ (a) and 0.920 (b), defects mostly appear in the form of dislocation-pairs. Figure (c) shows that the number of defects is increased at the density $\rho\sigma^2 = 0.914$ and the major contribution is coming from free dislocations. In the liquid $\rho\sigma^2 = 0.890$ (d) the defect-density becomes very high. The bottom panel replicates the same system area as above. The corresponding voronoi cells are color-coded with the local orientational order values. These figures clearly indicate that the deformation caused by defects formation lowers the orientational order in the system. The results shown here are obtained from a single snap shot. 77

Figure 3.13 Sequence of plots that shows the spatially resolved and time-average density profiles for the whole system. The system was divided in a grid of 10×10 with each sub-box dimension $L_x/10 \times L_y/10$. The average system densities are indicated on the top of the figures. Overlapped on this are plots of the average local orientational order in the sub-box (for a single configuration) as indicated by the arrows. In the solid phase, the density is uniform and there is a long range orientational order. As the solid melts ($\rho\sigma^2 < 0.920$) to a hexatic phase, coexistence of phases with different densities is observed in the system. The high and the low density phases are associated with long and short ranged orientational order, respectively. 78

Figure 3.14 Sequence of plots that shows the spatially resolved orientational order for the whole system for a single configuration. The system was divided in a grid of 10×10 with each sub-box dimension $L_x/10 \times L_y/10$. The different densities are indicated on the top of the figures. Overlapped on this and indicated by the arrows, are plots of the local orientational order averaged in the sub-box. In the solid phase, there is a long range orientational order. As the solid melts to a hexatic phase, in the density range of $0.910 < \rho\sigma^2 \leq 0.920$, there isolated regions of low orientational order in the system. In contrast, in the density regime $0.900 \geq \rho\sigma^2 \leq 0.910$, coexisting phases with high and low orientational order is observed in the system. 78

Figure 3.15 Time evolution of coarse-gained orientational order at the density $\rho\sigma^2 = 0.906$. The heatmap at each time snapshot was obtained by dividing the whole system into 10×10 blocks.The local orientational order $\psi_6(\mathbf{r})$ is calculated inside each block using the particle based definition ψ_6^i and restricting the sum in Eq. (3.2) over the sub-boxes. Overlapped on the heatmap are the local orientation vectors $(\mathrm{Re}\,\psi_6(\mathbf{r}), \mathrm{Im}\,\psi_6(\mathbf{r}))$ indicated by the arrows. The time evolutions indicate a stable macrophase separation of high and low hexatic order. 79

Figure 3.16 Distribution of the solid order parameter ψ_G^ℓ in a sub-system of size $L_x/50 \times L_y/50$ for different densities as indicated in the legend. At the solid-hexatic melting point of $\rho_m\sigma^2 = 0.920$, the distribution is uni-modal and peak at $\psi_G^\ell \approx 0.6$. With the melting of the solid, the peak shifts to lower values but the uni-modal nature of the distribution does not change. This indicates that the transition is continuous. . . 80

Figure 3.17 Distribution of the orientational order parameter ψ_6^ℓ in a sub-system of size $L_x/10 \times L_y/10$ for the system densities as indicated in the legend. The distribution shows weak double maxima at the boundary of the stable hexatic point $\rho\sigma^2 = 0.906$. The corresponding free-energy, defined as the negative logarithm of the probability distribution, is shown in the inset for the same three densities as in the main plot. A clear double minima, albeit very weak, appears in the free-energy. . 82

Figure 4.1 (a) Phase diagram in the density- frequency plane. The color code indicates the values of the solid order parameter $\langle \psi_{\mathbf{G}_2} \rangle$ of the stochastically ratcheted 2d colloidal suspension at different density and ratcheting frequency. Sky-blue denotes high solid order. The dashed lines through open symbols ($\triangledown$, $\circ$) show the boundaries of instability of the solid phase. The dash-dotted line through ■ indicates the low driving frequency f_s below which the system can relax to instantaneous external potential profile. In the opposite limit of high frequencies, the system feels a time- integrated constant confinement analogous to a laser induced freezing and consequently exhibits a high value of the order parameter. In the regime of intermediate frequencies, the long range order is broken due to the particle current. (b)-(h) Plots of time-averaged local density profiles $\rho(x,y)$ over a section of $10\sigma \times 10\sigma$ area, at different densities and frequencies as indicated in the figures. Their cuts ρ_y measured along the vertical white dashed lines, and ρ_x measured along the horizontal dashed lines are shown in the out-ward projected ordinate and abscissa, respectively. 90

Figure 4.2 Relaxation dynamics of the solid and hexatic order parameters at $\rho\sigma^2 = 1.04\,(a)$ and $\rho\sigma^2 = 0.98\,(b)$, respectively. The time scales for relaxation are $f_s^{-1} \approx 6\,\tau\,(a)$ and $f_s^{-1} \approx 70\,\tau\,(b)$. 92

Figure 4.3 (color online) (a) Variation of the scaled particle current $(\kappa\rho u_0)^{-1}\langle j_y \rangle$ along the direction of the drive as a function f/ν for different densities as indicated in the legend. The solid line is plot of the function $(f/\nu)/\left(1+(f/\nu)^2\right)$ as given by Eq. (4.2). (b) Plot of the current amplitude $\rho\kappa u_0$ as a function of density. The solid line is a fit to the data using the functional form $\kappa D_0\rho^{3/2}(1-\rho/\rho_c)$ with κD_0 and ρ_c as fitting parameters with values $\kappa D_0 \approx 0.22$ and $\rho_c\sigma^2 \approx 1.004$. 94

Figure 4.4 Parametric plot of the scaled particle current $(\kappa\rho u_0)^{-1}\langle j_y \rangle$ and the solid order parameter $\langle \psi_{\mathbf{G}_2}$ with changing frequency $f\tau$ is shown for three densities as indicated in the legend. The open (filled) symbols represent the increase (decrease) of current with frequency. For better visibility, plots at $\rho\sigma^2 = 1.00$ and 1.04 are shifted along the $\langle \psi_{\mathbf{G}_2} \rangle$ axis by 0.1 and 0.2, respectively. 95

Figure 4.5 (color online) Typical trajectories of neighboring particles are shown for three frequencies $f\tau = 0.01$ (a), 1.0 (b) and 30.0 (c) for a system at a density of $\rho\sigma^2 = 1.04$. At low driving frequencies, even though the trajectories are localized, we observe hopping between neighboring lattice points along the x-direction (a). In contrast, at high driving frequencies the trajectories are more strongly localized (c). At intermediate frequencies that drives higher directed current through the system, the trajectories are extended along the direction of the drive (b). In (d) we plot the relative mean-square displacement $\langle(\mathbf{u}_i - \mathbf{u}_j)^2\rangle$ of nearest- neighbour pairs corresponding to initial configuration. We plot the results for the three ratcheting frequencies. The results are averaged over 10 pairs of trajectories. We observe that in the current carrying regime, $f\tau = 1.0$, the relative displacement fluctuations diverge in a diffusive manner. 97

Figure 4.6 (color online) Typical trajectories of particles at densities $\rho\sigma^2 = 0.98$ are shown for three different frequencies $f\tau = 0.01$, 1 and 30. At high frequencies the particles get localized, whereas at very low frequencies localization happens only at densities above ρ_c. In the intermediate frequencies, at both densities the trajectories span a length scale of $\approx 20\sigma - 30\sigma$. 98

Figure 4.7 (color online) Plot of the mean-square displacement at density $\rho\sigma^2 = 1.04$ for frequencies $f\tau = 0.01$ (green), 1.0 (red) and 30.0 (blue). The displacements in $\langle\Delta x^2\rangle$ are shown with open symbols and that in $\langle\Delta y^2\rangle$ are represented with filled symbols. 99

Figure 4.8 Plots of the static structure factor $\langle\psi_{\mathbf{q}}\rangle$ for the densities $\rho\sigma^2 = 1.04$ (a-c) and 0.98 (figures d-f). The three columns correspond to three different frequencies $f\tau = 0.01$ (a and d), 1.00 (b and e) and 30 (c and f). 100

Figure 4.9 System size dependence of the solid order parameter. The ratio of mean order parameter measured over blocks of size $\ell = (\ell_x \times \ell_y)^{1/2}$ with respect to that measured over the whole system, $\langle\psi_{\mathbf{G}_2}(\ell)\rangle/\langle\psi_{\mathbf{G}_2}(L)\rangle$ decays with ℓ/L with power law $(\ell/L)^{-\nu}$. The data is shown for different densities as indicated in the legend. The solid and open symbols denote results at frequency $f\tau = 30$ and $f\tau = 0.01$, respectively. The solid black line is a plot of the power-law $(\ell/L)^{-1/3}$ expected at the equilibrium KTHNY melting point. 101

Figure 4.10 Dependence of the (a) solid order parameter $\langle\psi_{\mathbf{G}_2}\rangle$ and (b) hexatic order parameter $\langle\psi_6\rangle$ as a function of frequency is plotted for different densities as indicated in the legend on the top. The equilibrium melting point $\langle\psi^m_{\mathbf{G}_2}\rangle = 0.376$ is denoted by the dashed lines in (a). The variations of (c) $\langle\psi_{\mathbf{G}_2}\rangle$ and (d) $\langle\psi_6\rangle$ are shown as a function of the mean density for three driving frequencies $f\tau = 0.01$, 1 and 30 as indicated in the legends. 102

Figure 4.11 Plot of the solid order parameter $\langle\psi_{\mathbf{G}_2}\rangle$ and the hexatic order parameter $\langle\psi_6\rangle$ for the equilibrium phase transition (for more details see Chapter 2). The green dashed line denotes solid melting point $\langle\psi^m_{\mathbf{G}_2}\rangle = 0.376$, and the black dash-dotted line denotes the hexatic melting point $\langle\psi_6\rangle = 0.06$. In figure ($b$) we show a similar plot for the two order parameters but in the presence of a time- independent potential of the form $U_{ext}(x,y)$ given in Section 4.2 with $V(t) = \varepsilon$. In the presence of this potential, the hexatic does not melt in the regime of $\rho\sigma^2 \geq 0.94$. The external potential maintains a significant hexatic order, with a value greater than $\langle\psi_6\rangle = 0.51$, although the solid order does drop below 0.376 at $\rho\sigma^2 \approx 0.96$. 103

Figure 4.12 (color online) Plot of the finite size scaling ratio $\langle\psi_6(\ell)\rangle/\langle\psi_6(L)\rangle$ for three different frequencies as indicated in the legend at a density of $\rho\sigma^2 = 1.04$. The inset depicts the values of $\langle\psi_6(\ell)\rangle$ as a function of ℓ/L for the three driving frequencies corresponding to main plot. . . 104

Figure 4.13 Probability distributions of the local solid and hexatic order parameters $\psi^l_{\mathbf{G}_2}$ and $|\psi^i_6|^2$. The distribution functions $\mathscr{P}(\psi^l_{\mathbf{G}_2})$ at densities $\rho\sigma^2 = 0.98$ (a) and $\rho\sigma^2 = 1.04$ (b). The local solid order parameter is determined over subsystems of length $\ell = (\ell_x \times \ell_y)^{1/2}$, where $\ell_x/L_x = \ell_y/L_y = 1/14$. The distribution functions of local hexatic order $\mathscr{P}(|\psi^i_6|^2)$ at $\rho\sigma^2 = 0.98$ (c) and 1.04 (d), corresponding to four representative ratcheting frequencies as indicated in the legends. . . 105

Figure 4.14 (Color Online) The pair correlation functions $g(x,0) - g(\infty,0)$ calculated at the mean densities $\rho\sigma^2 = 0.98$ (a) and 1.04 (b) for the frequencies indicated in the legends. 106

Figure 4.15 Pair correlation functions in the driven 2D colloidal suspension at densities $\rho\sigma^2 = 1.04$ in the top panels (a-c) and $\rho\sigma^2$=0.98 in the bottom panels (d-f) corresponding to three different frequencies $f\tau = 0.01$ (left column), $f\tau = 1$ (middle column) and $f\tau = 30$ (right column). 107

Figure 4.16 Plots of $g(x,0) - g(\infty,0)$ at different densities $\rho\sigma^2$ of the system for frequencies $f\tau$ indicated in the legends. In (a)–(h) we show the data near the high-frequency phase boundary, and in (i)–(p) near the low-frequency phase boundary. The solid black lines denote the power law $x^{-1/3}$ that indicates the expected correlation at the solid melting point within KTHNY thoery[31–33]. 108

Figure 4.17 (a)-(d): Configurations of the system in $100\sigma \times 100\sigma$ sub-volumes at a density of $\rho\sigma^2 = 1.04$ for frequencies $f\tau = 0.01$ (a), 1 (b), 10 (c) and 30 (d). The particles are color coded according to the number of their topological neighbors n_v, with gray $(n_v = 6)$, blue $(n_v = 7)$, red $(n_v = 5)$, purple $(n_v = 4)$, and yellow $(n_v = 8)$, as shown in the legend on top of (d). (e) The figure highlights the hexatic order in a region containing a connected string of defects marked by a dashed-box of size $20\sigma \times 20\sigma$ in (b). The Voronoi tesselations are shown for each particle within the box and are color coded according to the local value of the hexatic order. The arrows denote the orientation of the local hexatic order ψ_6^i. (f) Indicate typical examples of defect quartets, dislocations and defect clusters that appear in the system. . 109

Figure 4.18 (a) Plot of the total defect percentage N_d as a function of time for three different driving frequencies as indicated in the legend. The density of the system is $\rho\sigma^2 = 1.04$. At high frequency the system remains in a solid phase, and the defect formation is significantly low ($N_d < 1\%$). On the other hand, in the opposite limit of low frequency, $f\tau = 0.01$, the defect formation follows the swicthing of the driving potential, N_d switches between two values. In the intermediate current carrying regime, the formation of the defects is maximized. The defects are further classified by types, e.g., quartets, dislocations, clusters, and disclinations. (b) The average defect percentage $\langle N_d \rangle$ shows a non-monotonic variation with the ratcheting frequency. We show results at three densities denoted in the legend. (c) Variation of the time averaged percentage fraction of the individual defect types, the quartets, dislocations, defect clusters, and disclinations with ratcheting frequency. 110

List of Publications

The thesis is based on the following works:

1. Shubhendu Shekhar Khali, Dipanjan Chakraborty, and Debasish Chaudhuri. A structure–dynamics relationship in ratcheted colloids: resonance melting, dislocations, and defect clusters. *Soft Matter*, 16:2552–2564, 2020 (Chapter 4)
2. Shubhendu Shekhar Khali, Dipanjan Chakraborty, and Debasish Chaudhuri. Two step melting of the Weeks-Chandler-Anderson system in two dimensions. *arXiv e-prints*, page arXiv:2007.00297, July 2020 (Chapter 3)
3. Khali, S. S., Chakraborty, D.,Chaudhuri, D., "Phase transition in a system of two dimensional repulsively interacting colloids", (***Manuscript under preparation***) (Chapter-2).